Assessment and optimisation of a diamond master oscillator power amplifier

PhD Thesis

Pierre Julien

Institute of Photonics
Department of Physics
University of Strathclyde, Glasgow

March 27, 2026

This thesis is the result of the author's original research. It has been composed by the author and has not been previously submitted for examination which has led to the award of a degree.

Abstract

This thesis explores the theory and design of a diamond master oscillator power amplifier (D-MOPA) as a last stage amplifier for "eye safe" range (1.5-1.6 µm) laser sources with applications in outdoor Doppler LIDAR. The main characteristic assessed is the amplification factor defined as the ratio of output to input signal.

A numerical model of Raman amplification was developed to explore optimal parameters. It showed that top-hat seed pulses improve timing tolerance fourfold over Gaussian pulses, and that longer diamond samples enhance amplification (8 mm yields double the amplification of 4 mm). The model also highlighted parasitic 2^{nd}Stokes oscillation as a key constraint and informed the choice of AR coatings for the diamond.

The D-MOPA design was analysed and a proof-of-concept setup, first demonstrated by Lukasz Dsziechciarczyk, was re-characterised. Based on published results and new measurements three key limitations were identified: wavelength mismatch between the 2^{nd} Stokes wavelength and the EDFA seed optimal range, timing jitter between pump and seed lasers and parasitic 2^{nd} Stokes emission.

To remedy the wavelength mismatch a novel 1083 nm Q-switched Nd:YAP laser using a birefringent filter was developed. It produced 500 µJ pulses of 38 ns with $M^2 = 1.19$ and 0.9 nm linewidth. Integration of this pump source along with other optimisations such as a longer diamond sample and better synchronisation of the seed led to an improved amplification factor of $\times 1.15$ using half the pump pulse energy.

The results validate the potential of D-MOPA systems for efficient amplification in the eye-safe wavelength region. Remaining limitations were also identified such as the fragility of anti-reflection coatings on the diamond and the continued parasitic 2^{nd} Stokes emission which offer clear directions for further improvements.

Acknowledgements

I would especially like to thank Professor Alan Kemp, my thesis supervisor, for his supportive and caring demeanour throughout the incredibly challenging COVID period, both on a personal level and for the group as a whole. I am also grateful for his in-depth discussions on a wide range of questions and his inexhaustible knowledge of all things laser-related. Additionally, I want to thank the other members who joined the group later for their valuable help and expertise, particularly in the lab: Dr. Niall Simpson and Dr. Martin Lee. Although he has since left the group, I would also like to express my gratitude to Dr. Vasili Savitski for his continued support and enthusiasm for diamond lasers.

Outside of the world of academics I have to thank the person that has been at my side for almost the entire duration of my thesis Haya, my partner whose boundless support and care made it all possible. I am also deeply grateful to my parents and my entire family for their unwavering support and encouragement. Finally, I would like to extend my thanks to everyone else who has helped me throughout my PhD, enabling me to reach where I am today.

Contents

List of Figures

List of Tables

List of Tables

Chapter 1

Introduction

This work aims to evaluate the feasibility of a novel method to achieve a high-power laser system in the eye-safe wavelength range of 1.5-1.6 µm while maintaining its spatial and spectral quality. Such a system would be of use for many applications, including light detection and ranging also known as LIDAR. This thesis will explore these goals by reviewing a proof-of-concept diamond master oscillator power amplifier or D-MOPA and will present the ways to optimise such a setup through both experimental and theoretical means.

Due to the numerous advantages of diamond combined with the advancements in the synthesis and fabrication of diamond in the last 20 years [1, 2] it has increasingly become an attractive option for research and industry. Not only is it incredibly hard, it also has a transparency range of 220 nm up to 2.5 µm and exhibits attractive properties for Raman lasers [3, 4] and amplification designs described in more detail in [5, 6].

This thesis will assess the feasibility of developing a setup that might allow a laser at the eye-safe range with TEM_{00}, 1.5 MHz repetition rate, at least 100 µJ pulse energy with 1-2 ns duration and 150 W average power.

1.1 Motivation for developing a D-MOPA

To better understand the motivation and context for the aims, a brief explanation of LIDAR and its requirements will be provided. LIDAR is used in many applications from range finding and 3D mapping to our focus in this thesis of wind surveying [7–

11]. LIDAR operates on the same basic principle as radar: a signal is transmitted, and its reflections are collected by a sensor. However, instead of radio waves, LIDAR uses light as the probing medium. This enables it to be generally more precise and accurate than radar [12–14]. LIDAR is used in four main methods: elastic, inelastic, differential absorption and heterodyne systems [15, 16].

The elastic method uses the reflections or refractions off a target most commonly by either scanning a pulsed laser beam over an area using mobile optical elements or by flashing a single high energy pulse to characterise the target. For range sensing and 3D mapping it determines the distance to the target by using the time of flight of the laser such that a distance, $d = \frac{c \times \delta t}{2}$ where c is the speed of light, δt the time of flight and a factor of 2 indicates the round-trip from the source to the detector. From this the resolution of the distance is determined by the pulse duration of the laser such that: $\Delta d = \frac{c \times \Delta t}{2}$, where Δt represents the pulse duration. Thus, when the laser pulse width is longer than the round-trip time the value of Δt can not be resolved.

Inelastic LIDAR by comparison uses many different inelastic interactions such as Raman, fluorescent or Brillouin effects which can then be used to determine the physico-chemical composition of the target medium. These systems analyse the wavelength offset of the scattered light with respect to the emitted light which is determined by the molecules, atoms or both that make up the targeted medium.

Differential absorption systems are used to measure molecular concentrations of a target component. These systems emit light at two neighbouring wavelengths. One of these wavelengths will be chosen to be strongly absorbed by the target. Therefore, comparing to the adjacent wavelength the ratio of the energy of the backscattered pulses between the two wavelengths is proportional to the molecular concentration of the target.

The last method is heterodyne systems. They are mainly Doppler LIDAR systems which are used to measure wind speed. They use the Doppler effect to determine the velocity of the target by measuring the shift in the back scattered light such that $v = \frac{\Delta f \lambda}{2}$ where v is the velocity of the target, Δf the Doppler frequency shift of the returning laser and λ the emitted wavelength. This method has requirements of narrow linewidth

Technology	Wavelength	Energy	Repetition rate	Pulse duration	Average power
Pulsed laser diode	905 nm	< 10 µJ	several kHz	30-200 ns	≈ 10 mW
Er fibre laser	1550 nm	< 400 µJ	several 10 kHz	5-100 ns	≈ 4 W
Yb fibre laser	1064 nm	< 200 µJ	several 10 kHz	5-100 ns	≈ 2 W
DPSS Nd:YAG	1064, 532, 355 nm	60, 30, 10 mJ	< 100 Hz	5-10 ns	≈ 5 W

Table 1.1: Overview of the laser sources used for LIDAR systems. [15]

sources as the accuracy of the frequency shift determines the measured resolution of the velocity.

These methods each have different requirements in their laser sources and the detection for their optimal use. This thesis will focus on the laser source requirements of scanning and Doppler LIDAR. Examples of such laser sources with wavelengths in the near infra-red can be found in table 1.1.

As shown in table 1.1, LIDAR laser sources have a wide range of characteristics depending on system architecture, measurement range and eye-safety constraints. These factors also lead to operation over different wavelength ranges, determined both by sensing requirements and by practical limitations of available laser technologies. Because of this, not all sources operate within the eye-safe range of 1.5–1.6 µm. The operating wavelength is therefore a key design parameter, as the intended environment of use can strongly influence the choice of laser source. In particular, safety standards such as the maximum permissible exposure defined in [17] impose wavelength-dependent limits on the allowable optical power. Since the average power of a pulsed system is directly related to the pulse energy through: $P_{avg} = E_{pulse}f$, where f is the frequency of the pulsed signal, operation within the eye-safe wavelength range enables the use of higher pulse energies, which can be required for certain LIDAR applications.

In the case of LIDAR for wind surveying, as mentioned before, it is used in an open air environment and therefore the source has a chance to reach a person's eye. From figure 1.1, which is a graph adapted from the American National Standard for safety of lasers, the maximum permissible exposure at the 1.5-1.6 µm is five orders of magnitude higher than at 1 µm. Therefore, using a source at this range enables LIDAR sources to have higher average power ,pulse energies or both which mean better signal to noise ratio of the measurements taken. In addition, the increase in allowable average power can also be distributed over a larger number of pulses, enabling higher pulse repetition rates and consequently higher scanner rates.

The requirements of a laser source for LIDAR based on this overview would be: operating within the eye-safe range (1.5-1.6 µm), a high repetition rate and high average power; MHz regime and above 100 W to allow for high signal to noise ratio, and fast scanning rates with around ns pulse duration to get acceptable distance resolution and very high beam quality for a low divergence beam from the source which improves the signal to noise ratio and the maximum operating distance of the LIDAR. In practice the selection of laser parameters must balance several competing requirements such as range performance, velocity sensitivity, eye-safety limits and system architecture. These targets would therefore make such sources suitable for a broad range of LIDAR applications beyond Doppler LIDAR measurements [15, 16]. Considerations regarding possible laser sources that emit at the eye-safe range and at high powers will be discussed

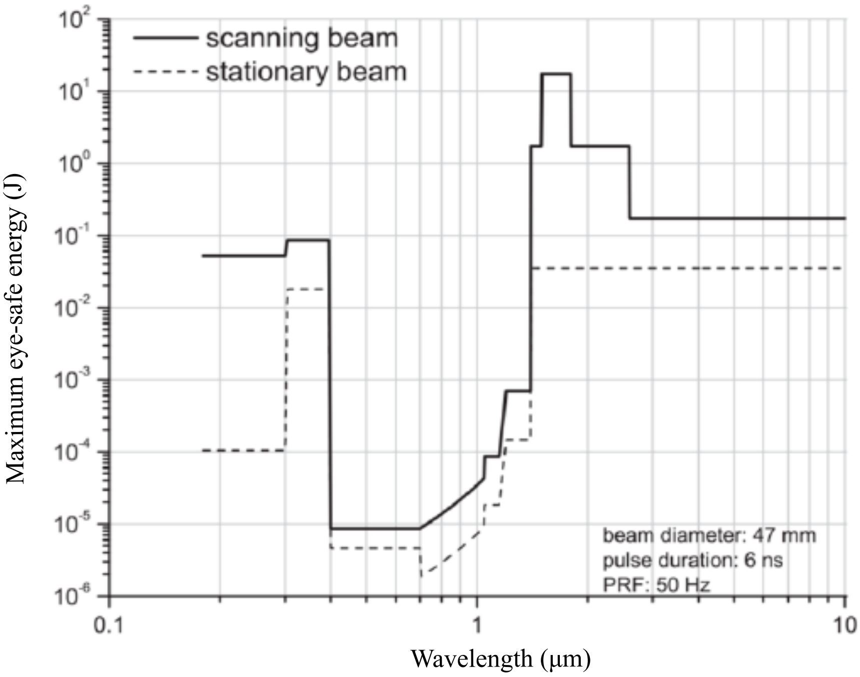

Figure 1.1: Graph adapted from the ANS showing the maximum permissible eye exposure depending on the wavelength of a laser, based on a 10 s exposure time
. [17]

to clarify the choice of a diamond master oscillator power amplifier.

1.2 Wavelength Considerations

The range between 1.5-1.8 µm is called the "eye-safe" range due to it being a peak in the maximum permissible eye exposure with a peak from 1.5 µm to 1.6 µm as shown in figure 1.1. This is due to the difference in how the eye absorbs energy depending on the wavelength. Indeed, above 1.4 µm laser light is primarily absorbed in the cornea and lens which are significantly more tolerant to optical energy than the retina. In contrast, below this wavelength, the light can reach the retina and potentially cause serious, irreversible injury or scarring [18]. At the eye-safe range, the maximum permissible exposure to the eye can be an order of magnitude more intense than at 1.4-1.5 µm and 1.8-2.5 µm, enabling high-power sources to operate safely in open-field environments. Careful consideration must still be given to power and the placement of high power sources, however, as the standard is specified for intensity and exposure time and as such a better name for eye-safe wavelengths would be retina-safe, as with long exposure or high enough intensity damage can still occur [19].

Various techniques exist to reach the eye-safe range for e.g. fibre doped amplifiers and lasers such as Yb:Er fibre and Er doped fibres. Other techniques modify existing lasers' wavelength through non-linear effects such as optical parametric oscillators (OPO) and Raman lasers. The focus in this thesis will be on the use of the Raman effect and more specifically diamond Raman lasers and amplifiers which uses χ^3 non-linear wavelength conversion to achieve longer wavelengths, This method will be covered in more detail in its own section 1.5 and will be compared to the other sources described above.

1.3 High Average Power Considerations

High power in any laser source comes with many considerations that need to be taken into account at the design stage. One such consideration is heat deposition in the lasing medium. In a solid state system, the quantum defect of a material, which represents the energy difference between the pump and laser emission wavelength, causes the extra energy to be deposited as heat in the laser gain medium. For example, in a commonly used laser system such as a diode pumped Nd:YAG at least 25% of the pump power is deposited as heat [20, 21]. At high powers the amount of energy and heat deposition can lead to severe degradation and, in extreme cases, damage to the laser gain material. Additionally, this heating tends to be non-uniform within the material with pump spot radiuses in the hundreds of micrometers being required to reach the threshold intensities, further exacerbating this effect. This leads to other consequences that need to be examined. One such consequence is non-uniform expansion of the material which affects its physical properties. The refractive index of the material for example is one such property that is impacted and has a great effect on its optical attributes. Uneven change of the refractive index causes a lens like effect where the optical path of light through the material changes depending on the area it goes through. This greatly affects many aspects of a laser setup and has to be taken into account when designing any high average power systems. It is called thermal lensing and affects the mode size of the laser and the stability of the laser cavity. Another consequence of this in materials such as Nd:YAG, is the induction of birefringence within the material which can influence the polarisation of the laser output, and because of this, the efficiency and quality of it.[22, 23]

It is important to find and implement measures to minimise these consequences. To better prevent these effects from happening first we will examine what happens to the heat deposited in the material. The dn/dT effect, with dn the change in refractive index and dT the change in temperature within the medium, will be investigated. In some solid-state laser setups the pump of the cavity can be modelled as a spatial Gaussian profile, though other profiles also cause thermal lensing to occur. This means that the power of the laser will be higher in the centre of the beam profile and weaker on the edges following a Gaussian distribution. Because of this the heat deposited within the material will be higher at its centre which in turn means that the change in refractive index of the material will also be bigger there. This induced refractive index gradient over the profile of the laser mode can lead to the thermal lens effect within the gain material. This lens effect behaves similar to traditional lenses within a cavity and will affect the laser mode and because of this the stability within the cavity. The focal length that this lens, in end pumped configuration pumped with a Gaussian pump, can be determined by:

$$f = \frac{K \pi w_p^2}{\eta P_p \frac{dn}{dT}} \tag{1.1}$$

Where K is the thermal conductivity of the laser material, w_p is the Gaussian radius of the pump beam, P_p is the absorbed pumped power, η the proportion of the pump converted to heat and dn/dT is the change of refractive index with temperature [21, 24, 25]. This equation shows that the thermal lens strength is proportional to the thermal conductivity of the material. As such an argument can be made that a higher thermal conductivity in the lasing material would make it easier to manage high powers. When taking this into consideration the choice of diamond as a high power lasing material becomes evident. Indeed, the thermal conductivity of a single crystal high purity diamond was measured to be $K = 2400\ Wm^{-1}K^{-1}$ [26]. This is two orders of magnitude higher than even the thermal conductivity of a YAG crystal ($K = 11\ Wm^{-1}K^{-1}$) which is already according to [27] a relatively high thermal conductivity for a laser crystal. This makes diamond unequalled when it comes to thermal management and therefore is a strong contender for any high power laser setup. In addition, the thermal lens focal length equation is an approximation for low and medium pump intensities. At higher pump levels the end bulging of the material contribution needs to also be considered as this can have as substantial an impact as the thermal index variation described above [21]. Here again diamond shines having a low thermal expansion coefficient [28]. As such it requires high temperatures to deform and presents itself to be a suitable material for high power laser applications.

When talking of high power lasers there are different avenues that have been explored to mitigate the effect of the heat deposition. To this point I have only discussed the material used in a solid-state cavity has been discussed but other laser system geometries also manage to minimise the heat deposition within the lasing material. For example in fibre lasers the choice of using a low absorption but very long gain medium such as rare earth doped glasses allows thermal lensing to be a negligible problem [29]. Instead the damage in fibre lasers tends to come from sources other than thermal effects. The long interaction length combined with the small core area and the high peak power cause high intensity effects such as Raman (described in more detail in section1.5) or Brillouin scattering (nonlinear scattering effect involving acoustic phonons). These non-linear interactions cause a multitude of non-desirable effects such as self-focusing, back-scattering and spectral broadening. [30–33]. Because of this for most lasers high power generation is a balancing act between the output power and the quality of the output which explains the many different current solutions to the high power source problem at “eye-safe” wavelength that LIDAR has.

1.4 Exploration of current eye-safe laser sources

With the aims and consideration now properly defined for what might be considered a useful laser source for LIDAR use, the current solutions that fit these parameters will be explored. As mentioned earlier these need to be lasers that are within the so-called “eye-safe” range of 1.5 to 1.6 µm to ensure that external use of the LIDAR is allowed with the highest possible power. This can be achieved through several methods. First using conventional laser materials which have a gain range within the eye-safe range and second using non-linear processes to convert the wavelength of an existing laser source by using for example the Raman effect or optical parametric oscillation (OPO).

1.4.1 Conventional Lasers

Conventional lasers in this context is used to designate lasers that use population inversion as the laser producing mechanism. Of these the most popular gain material that produces laser emission at the eye-safe range must be erbium doped glass. This material is part of the rare earth doped glasses that are commonly used especially in fibre setups. These use, for lanthanide ions such as erbium, the trivalent level of ionisation to form optically active centres within the doped glass. Of the rare earth glasses the ones typically used in fibre lasers are ytterbium, erbium and thulium each of which have slightly different characteristics due to their different energy transitions and more importantly in this case different wavelength emission ranges [34]. Yb fibre lasers tend to have a window of emission between 1050-1160 nm due to only having two manifolds; however, this also allows them to be free from a number of cooperative effects such as an energy transfer process, a cross-relaxation process, nonradiative energy transfer, cooperative emission, and excitation. They also benefit from a very high level of quantum efficiency reaching close to 100% and with relatively low quantum defect. As such they have the highest reported output powers reaching up to 8 kW [35]. Comparatively Er although having the more desirable, in the context of this work, emission range of 1530-1590 nm for the $^4I_{13/2}$ to $^4I_{15/2}$ manifold transition has a relatively small cross-section and as the doping concentration is limited by the need to avoid excessive quenching process it is more difficult to reach high power levels [34]. Additionally, by comparison with Yb, Er has a higher quantum defect. One solution found to compensate these unfortunate characteristics is to co-dope the glass with Yb [36]. The Yb ions can more efficiently absorb pump radiation and then transfer the energy to Er ions. This allows the fibre laser setups to reach higher power more easily. However there are still several limiting factors, the two biggest being Yb band amplified spontaneous emission which can cause parasitic lasing and self-pulsing. The second is even with using a fibre setup, the thermal effects are still a problem due to the increased quantum defect between emission and pump photons (∼1530 nm and 9xx nm) [37]. Because of this although both Tm and Yb fibres have surpassed the kW maximum power benchmark Er still lags behind [38].Tm with emission ranges around 1900 nm and 2100 nm which are far from our target range will not be explored in further depth in this work.

Currently the highest, as far as this author knows, maximum continuous wave power achieved in an Er doped fibre laser was reported to have an output power of 656 W at 1601 nm. This was presented by Lin et al in a paper published in 2018. An Er doped Yb free fibre laser was used to reach this record-breaking power output. It used a relatively large core of 146 µm and 0.7 mm inner cladding to suit the pump core [39]. Although an impressive and so-far unsurpassed output power at this wavelength range this setup would not be suitable for the LIDAR application we are studying. Indeed, the poor beam quality (M^2 over 10) and its continuous emission nature do not fit the requirements laid earlier.

Looking at pulsed systems that use Er,Yb:glass, the groundbreaking 3.2 mJ pulse energy reported by Sakimura et al [40] in 2019, with a repetition rate of 4 kHz and pulse width of 0.6 µs has already been improved to 45.2 mJ by the same group reported in Nomura et al [41] in 2023. It has a wavelength of 1540 nm compared to the 1550 nm of the earlier result. However the pulse width of 1.7 µs is longer than the previous one and the repetition rate is much lower at 150 Hz. The M^2 has also worsened from an average M^2 of 1.29 for Sakimura et al to 1.84 for Nomura et al. These were both achieved by using a master oscillator power amplifier or MOPA design to achieve such high pulse energies. Although in this example both lasers are pulsed, they again fall short of the targets set out in the initial goals. Indeed, not only are both repetition rates lower than the target of MHz but the pulse width is too long compared to the couple of nanosecond aim. As is recognised within the paper the long pulse duration has important consequences on the accuracy of the wind velocity sensing with the "standard deviation of the wind velocity within the probed atmospheric volume becomes large because of the effects of turbulence" [40].

From these examples, it is clear that although groundbreaking research has advanced the average and peak powers of fibre laser setups within the "eye-safe" range, several limitations remain, requiring trade-offs in other performance characteristics to achieve these results. There are also the limitations that come from choosing to use fibre lasers such as the non-linear effects found in high-intensity narrow linewidth pumping regimes such as Brillouin scattering etc. These effects can cause back-scattering, impact the spectral, temporal and spatial purity of the fibre laser, can lead to unwanted laser emissions and even ultimately damage[30]. The exact mechanism of these limitations although mentioned in passing in this section will not be examined in more detail due to being outside the scope of this work.

In conclusion, although these types of lasers have shown great promise and are already used in LIDAR based applications there are still many limitations which prevent these lasers from attaining the targets set out in this work. For that we will examine another area that achieves emission within the "eye-safe" range: wavelength conversion.

1.4.2 Wavelength Conversion

One method that is used to convert the wavelength of a pump laser to the desired "eye-safe" range is by using so-called optical parametric oscillation or OPO. Unlike traditional lasers which use stimulated emission to achieve optical gain nonlinear crystals such as BBO, LBO or LiNbO3 use parametric amplification to generate coherent light. This method takes a pump and generates two subsequent emissions called an idler and a signal. These are determined by a phase-matching condition and as such the wavelength of an OPO laser can be varied in wide ranges. This has made it an attractive method to access wavelengths which would otherwise be difficult or downright impossible in addition to a wide wavelength tuneability. In the studied context here OPO's make perfect sense as a potential source of otherwise difficult to achieve "eye-safe" wavelength. This is modelled similar to second harmonic generation or difference frequency generation such that the coupled equations for OPOs are [21, 42]:

$$\frac{dE_1}{dz} = i\omega_1\sqrt{\frac{\mu_0}{\epsilon_1}}d_{eff}E_3E_2e^{-i(k_3-k_2-k_1)z} \tag{1.2}$$

$$\frac{dE_2}{dz} = i\omega_2\sqrt{\frac{\mu_0}{\epsilon_2}}d_{eff}E_3E_1e^{-i(k_3-k_2-k_1)z} \tag{1.3}$$

$$\frac{dE_3}{dz} = i\omega_3\sqrt{\frac{\mu_0}{\epsilon_3}}d_{eff}E_1E_2e^{-i(k_3-k_2-k_1)z} \tag{1.4}$$

Where d_{eff} is the nonlinear optical coefficient which has a direct relation with nonlinear optical susceptibilities. ω is the frequency of the three waves and k the wavevectors which, to obey to energy conservation, are $w_3 = w_1 + w_2$ and to obey momentum conservation $\delta k = k_3 - k_1 - k_2$. μ and ϵ are permeability and permittivity of vacuum and when specified of the designated wave.

In the past OPOs and Raman lasers have been compared due to their similarity in both being wavelength conversion mechanisms with OPOs being described in, for example, the work of G. Roy and P. Mathieu published in 1996 [43] as the optimal choice above Raman. This has been contextualised with the choice in the paper to compare a more mature solid-state OPO setup to a high pressure gas cell. Gas cells are difficult to use especially in high energy designs with, in this paper, the need to continuously rotate the gas to mitigate some of the worst consequences of such a setup. This further highlights the importance of the development of more robust solutions for solid-state Raman sources at the "eye-safe" wavelength.

Recent work on OPO sources have reported both high peak power capabilities and high repetition rate, however, rarely are these both combined. For example, in the paper by M. Kaskow et al published in 2018 [44] a peak power of 1.4 MW or pulse energy of 28 mJ with a wavelength of 1570 nm was achieved. This used an intracavity KTP OPO pumped by a Q-switched Nd:YAG laser. The setup was also reported to have a relatively short pulse duration of 20 ns which can be considered to be within the target laid out in this work. However, it had a repetition rate of 20 Hz and the quality of the output both spatially and spectrally is not reported on other than the full-angle beam divergence being measured to be 2.5 mrad. Comparatively, in the paper by Guo et al published in 2015[45] although also using a similar setup of an intracavity KTP OPO but with a Q-switched Nd:YVO_4 laser instead, managed to reach a repetition rate of 10 kHZ. While not being the MHz target it is still significantly higher than the 20 Hz of the previous paper. This increase in repetition rate however can be found to be at the cost of peak power with the reported peak power being 25 kW (pulse energy of 150 µJ) for a pulse duration of 6 ns.

Other setups have shown promise such as the one in Liu et al which was published in 2021 [46]. This work used a self-optical parametric oscillator (SOPO) which uses a single Nd:MgO:PPLN crystal to act as both Q-switched pump and OPO to reach the "eye-safe" wavelength. This SOPO design was reported to have a peak power of 1.26 kW (15.3 µJ) at 1512 nm but with a repetition rate of 60 kHz with a pulse width of 12.16 ns.

From these examples even though OPOs offer a very compelling solution to achieving "eye-safe" wavelengths there is a clear distinction between the reported very high energy sources (above ~1 mJ) and the high repetition rate sources (above ~10 kHz). This can be found to be related to the difficulty in managing the thermal limitations of the non-linear crystals used in OPOs and, as in the MW source, the appearance of ASE at other wavelengths [44].

1.5 The Raman effect and uses

Another wavelength conversion method that is commonly used to reach the eye-safe wavelength like OPOs is the Raman effect. This also uses a non-linear interaction between certain materials and light to convert the wavelength to another. This will be the effect on which this thesis will be focused and as such will receive a more in-depth review of its background, theory and what the potential design consequences of choosing this route are. Finally, the choice of Raman active material and a review of eye-safe Raman sources will be investigated.

1.5.1 Theory

Discovered in 1928 by C.V. Raman and K.S. Krishnan, the Raman effect describes inelastic scattering of photons by matter [48]. Most photons are scattered elastically as described by the Rayleigh effect [49]; however, a small percentage are scattered inelastically through other methods such as Raman interaction. It describes, as shown

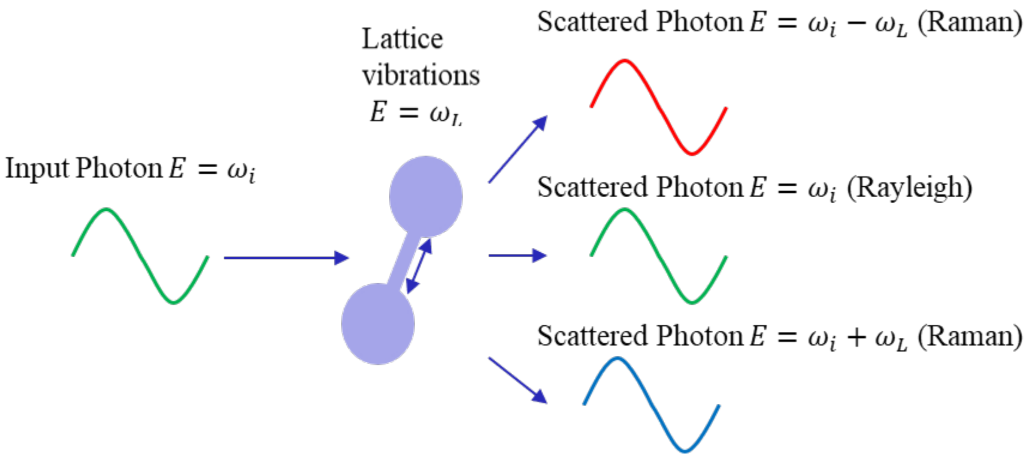

Figure 1.2: Diagram of the Raman scattering in its two forms: Stokes Raman and anti-Stokes Raman scattering compared to the more common Rayleigh scattering. Where E is the energy of the scattered photon, ω the angular frequency of either the incident photon designated by the subscript i or of the lattice vibrations designated by the subscript L. Natural units are used here ($\hbar = 1$) as a shorthand. [47]

in figure 1.2, the interaction of an input photon with the lattice vibration within certain mediums which changes the energy of the scattered photons. When the photon gains energy it is called anti-Stokes and when it loses energy it is called Stokes after the Irish physicist G. G. Stokes [50].

As the scattered photons experience a change in energy, they also experience a change in wavelength described by equation 1.5 for the Stokes shift where lambda is the wavelength of the photons either emitted or incident as shown by their subscript e and i respectively. For the anti-Stokes shift which will not be explored in as much detail the subtraction in the denominator becomes an addition.

$$\lambda_e[nm] = \frac{1}{\frac{1}{\lambda_i[nm]} - \frac{\omega_L[cm^{-1}]}{10^7}} \tag{1.5}$$

In this equation ω_L is called the Raman shift and is often given, as shown in the equation, in units of wavenumber. This shift is an intrinsic property of the Raman active material and will determine the change in wavelength of the scattered photons. This is the key to the wavelength conversion property of the Raman effect.

An energy diagram presented in figure 1.3 provides more context to its use as a laser mechanism. This shows how an incoming photon creates a virtual energy state in the scattering medium. It is important to note there is no electronic absorption of the incoming photon and the virtual state is not a real electronic level and is merely used as a way to visually represent Raman scattering. The difference in energy and thus wavelength between the incident and scattered light depends on the energy of the phonon which will be an intrinsic property of the scattering medium. This difference in energy is also called the Raman shift of a material or ω_L in equation 1.5 which enables the calculation of the wavelength of the scattered light from the incident wavelength.

The scattered photons described above are considered to be spontaneous and have random direction and phase. This spontaneous Raman scattering is a rare occurrence and required an intense source to be first demonstrated and measured. This spontaneous scattering can in turn stimulate more scattering resulting in photons with identical characteristics creating a coherent output. This stimulated Raman scattering is what

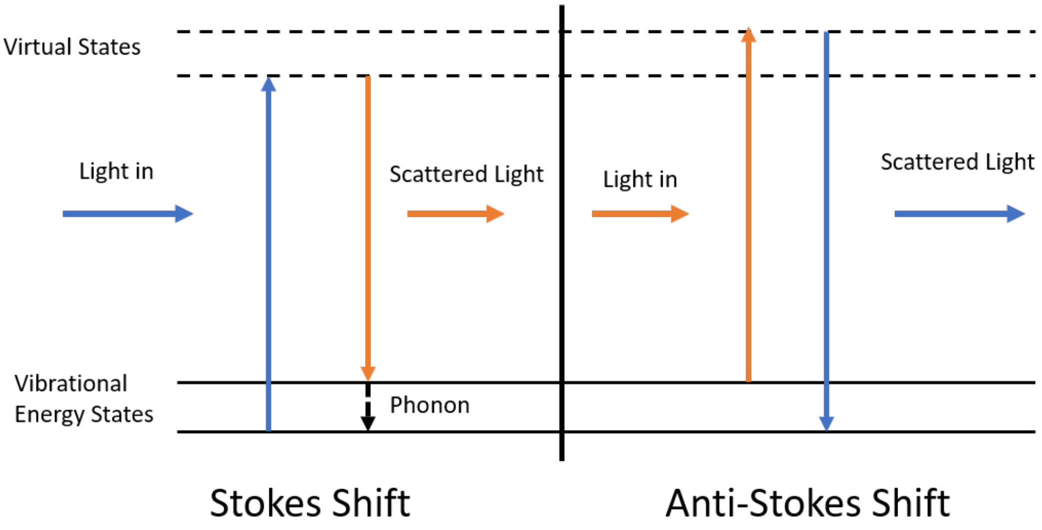

Figure 1.3: Diagram of the energy levels involved in Raman scattering in its two forms: Stokes Raman and anti-Stokes Raman scattering. The incident light in the Stokes case is absorbed into a virtual energy level and de-excites leaving behind some energy in the material in the form of a phonon. For anti-Stokes the incident light excites into a higher virtual energy level due to pre-existing phonons and then is scattered with higher energy when it de-excites to a lower energy level. [47]

enables the Raman effect to be used as a lasing or amplifying mechanism.

1.5.2 Raman laser characteristics

Due to the differences in the mechanisms behind the generation of coherent photons, conventional lasers and Raman lasers have different characteristics ,some beneficial and others not, as presented in Williams et al [5]. This paper specifically reviewed the state of high power diamond Raman lasers in 2018 as part of an invited paper. The main drawbacks as presented in the paper of using Raman scattering are first that it requires very bright pump sources. Indeed, the figure of merit for the threshold required to achieve lasing in a Raman laser with a Raman crystal of Raman gain of approximately 10 cm/GW is "well above tens of MW/cm^2" according to the paper. As such most Raman setups require pumps with complicated designs such as Q-switched solid state lasers for their high peak powers. In addition to the high intensity required for Raman lasers the pump also needs to have a narrow linewidth. As the Raman gain mechanism relies on the coherent generation of a phonon field in the medium this imposes stringent requirements on the linewidth compared to the more accepting broad absorption bands of conventional lasers, the origin of which will be explored in more detail in section 1.6.2. In general, the pump bandwidth is preferred to be smaller than the Raman linewidth of the material as a larger bandwidth leads to a proportional reduction in gain.

However, the advantages of a Raman setup do balance the pump requirements First is the larger output wavelength choice. As the Raman effect is not wavelength dependant, Raman active materials can generate gain across their whole transmission band being only dependant on the pump laser wavelength. Additionally the effect can be cascaded to second and higher order Stokes fields to generate wavelengths further spaced from the pump. Thus, broadly tuneable output is achieved by tuning the wavelength of the pump itself. Another major difference from conventional lasers is the lack of energy storage within the material. As the Raman gain depends on the pump intensity it exists only so long as the pump duration. This does mean that there is no possibility of Q-switching in Raman lasers. One consequence of the lack of energy storage within the material is the lack of any kind of spatial hole burning. This is the preferential depletion of energy from anti-node regions of a standing-wave cavity mode in population inversion lasers. Because of this, Raman lasers avoid the added complexity spatial hole burning brings in laser setups such as longitudinal mode instabilities and high intensity noise in intracavity frequency doubled configurations.

The last major advantage is that the output of a Raman laser is automatically phase matched due to being a process which relies solely on the inelastic scattering of photons with a material's vibrational fields. This enables the generation of high brightness output from low-beam quality inputs and the ability to have multiple non-collinear pumps and side-pumped configurations. This has been shown to lead to what is called a "beam clean-up" or brightness enhancement effect where for example in the paper by S. Antipov et al a relatively poor pump quality of a $M^2 = 15$ had a Raman laser output quality of $M^2 = 3$ [51] which is a considerable improvement of a factor of 5.

Because of these advantages we chose to use the Raman effect to convert a pump wavelength to the "eye-safe" range. Given this choice we shall first explore the considerations especially in terms of how the target wavelength will be reached and what kind of setup will be used. Finally, we shall briefly review some of the other examples of eye-safe Raman lasers which already exist.

1.6 Raman laser setup for eye-safe wavelength

1.6.1 Choice of material

From the way the Raman effect determines the wavelength conversion of an incident photon, it is important to choose the right material to allow us to achieve a wavelength within the eye-safe range in as few shifts as possible. This is especially important as, as discussed in the previous section, the pump source has to be high energy and low linewidth which limits the potential choice of pump lasers. Ideally, a Raman material that would allow a pump source of around 1 µm would be the target as there exists many different laser setups that reach high pulse energy around that wavelength range. Unfortunately, the Raman effect is found only in very specific materials. Gases such as hydrogen and methane and liquids such as carbon disulphide and benzene were the first materials discovered and investigated that exhibited the Raman effect. However both liquids and gases have fundamental limitations that make them difficult to setup. More recently crystals which have an inversion symmetry within their lattice have been found to also exhibit the Raman effect. Such crystals include various tungsten materials such as potassium gadolinium tungstate which is known more frequently as KGW, but also barium tungstate and strontium tungstate. Doped glasses such as the ones in fibre lasers also exhibit the Raman effect where, although they have a low Raman gain coefficient, the long interaction length coupled with a small effective mode area allows them to achieve a large Raman gain. Lastly diamond is also a Raman "active" material which exhibits some of the highest Raman gain and largest Stokes shift of them all. [3, 52]

Indeed, when comparing diamond to KGW, which is one of the most commonly found Raman materials as shown in table 1.2, it is evident that diamond is better in almost every property. Given our aim, the most important material specific property is

Parameter	Diamond	KGW
Thermal conductivity, k (W/mK)	2000	3.8*
Thermal expansion, α_{th} ($\times 10^{-6}K^{-1}$)	1.0	17.4*
Thermo-optic coefficient, dn/dT ($\times 10^{-6}K^{-1}$)	9.6	-17.3*
Typical length of crystal, L (mm)	6	25
Max. Raman gain coeff., g at 1064 nm fundamental, (cm/GW)	21	5.7*
Raman shift (cm^{-1})	1332	767/901

Table 1.2: Table comparing the characteristics of diamond to the commonly used KGW. *Property not isotropic - the maximum value is given for the purposes of comparison [52]

that of the Raman shift. This comes from, as shown earlier, the phonon energy which dictates the difference between the incoming and scattered photons. In diamond this phonon energy is of 1332 cm^{-1} whereas in KGW the highest phonon energy is of 901 cm^{-1}. Of the Raman crystals, diamond has the highest Raman shift with the next highest $CaCO_3$ being 1086.4 cm^{-1}.As a comparison diamond has a higher Raman gain of 21 cm/GW at 1064 nm compared to KGW 5.7 cm/GW [52]. Because of this, diamond can achieve an eye-safe wavelength when pumped with a source with wavelength above 1070 nm. Although unfortunately this is higher than the commonly found Nd:YAG 1 µm systems, other neodymium doped sources such as Nd:YAP or Nd:YVO_4 or even the Yb fibres discussed earlier are compatible with such a requirement. Although typical Yb based sources operate around 1.06µm the fibre amplification bandwidth does theoretically reach 1.15 µm which would be enough for diamond to reach the “eye-safe” range in only 2 Stokes shifts.

Another area in which diamond is notably better than most other materials are its thermal properties. Diamond has one of the highest thermal conductivities known and its thermal expansion coefficient is also very low when compared with KGW and other commonly used laser materials. One key area, however, where diamond is worse is in its availability, which is why there are relatively fewer published studies. Due to the difficulty in its production and its cost, diamond is more difficult to source and has on average a smaller length than KGW making it less attractive to research. However, there have recently been significant improvements in the quality and quantity in part due to significant advancements in the chemical vapour deposition or CVD technique which has allowed for high purity and quality synthetic diamond to be more readily available.

1.6.2 Theoretical Requirements

Having chosen a material, we can explore the details of the Raman effect theory further and calculate important parameters from it. We revisit the previously introduced Raman gain coefficient for diamond, outlining its theoretical origin and presenting the equations that describe its dependence on linewidth, polarisation, and related parameters, together with the resulting implications for setup design. Considering equation 1.6 which models the growth from an individual Stokes mode with wave number k_s such that [53]:

$$\frac{dn(k_s)}{dt} = N\left(\frac{\partial\alpha}{\partial q}\right)^2 \frac{4\pi^3\omega_s}{\mu_L\mu_s^2 m\omega_0 c}(1+n(k_s))I_L\rho(\omega_s-\omega_L+\omega_0) \tag{1.6}$$

Where $n(k_s)$ is the occupation number of a single Stokes mode, N is the number density of scattering molecules, $\frac{\partial\alpha}{\partial q}$ represents the molecular polarisability alpha in function of the local coordinate q, m is the reduced mass, μ denotes the refractive index of either the laser or Stokes photons specified by the subscript L and s respectively, I_L is the laser intensity, $\rho(\omega_s-\omega_L+\omega_0)$ is the spectral distribution which depends on the frequencies of the Stokes ω_s, the laser ω_L and the transition frequency of the molecules considered ω_0.

Equation 1.6 describes the growth of the occupation number of an individual Stokes mode as a result of Raman scattering. The rate of growth is proportional to the laser intensity I_L, highlighting the stimulated nature of the process. The term $(1+n(k_s))$ indicates that once a significant population of Stokes photons has been generated, further scattering is enhanced, leading to exponential amplification. The strength of the interaction is determined by the material-dependent polarisability term $\left(\frac{\partial\alpha}{\partial q}\right)^2$, while the spectral distribution function $\rho(\omega_s-\omega_L+\omega_0)$ introduces a dependence on the Raman linewidth and therefore the frequency range over which efficient scattering can occur. These dependencies underpin the macroscopic description of Raman amplification in terms of the Raman gain coefficient discussed in the following section.

Once a large occupation of the individual Stokes modes has been reached ($n(k_s) >> 1$), equation 1.6 predicts an exponential growth of the scattered photons which is the hallmark of the stimulated Raman regime. This behaviour can be modelled using the Raman gain coefficient g_s, which relates the pump intensity I_p to the growth of generated Raman signal I_s along an interaction path x as: $I_s(x) = I_s(0)e^{g_s I_p x}$. This equation highlights the exponential dependence of the signal intensity, and so Stokes photon number, on both the pump intensity and the length of the Raman active material.

Another consequence of note from equation 1.6 is that for a narrow laser line and for homogenous broadening of the molecular transition, a Lorentzian line shape of the spectral distribution ($\rho(\omega) = \omega_s - \omega_L + \omega_0$) may be expected of the form:

$$\rho(\omega) = \frac{\Gamma/\pi}{(\omega_s - \omega_L + \omega_0)^2 + \Gamma^2} \tag{1.7}$$

Where Γ is the linewidth of the distribution. Γ is also related to the dephasing time T_2 of the crystal lattice phonons such that $\Gamma = \frac{1}{T_2}$. For synthetic diamond $T_2 = 7$ ps which corresponds to a linewidth Γ of 143 GHz or 1.5 cm^{-1} [54]. This linewidth can also be related to the pump linewidth by observing that the threshold of a Raman laser can be modelled by:

$$I_i^{th(b)} = (1 + \frac{\Gamma_P}{\Gamma_R}) I_i^{th(m)} \tag{1.8}$$

Where $I_i^{th(b)}$ and $I_i^{th(m)}$ are threshold intensities for a broadband and monochromatic pumps and P and R stand for pump and Raman respectively. From this relation we can see that narrowing the pump linewidth reduces the Raman threshold. Additionally, the efficiency of a Raman laser falls off for a ratio of pump over Raman linewidth larger than unity which explains why a narrow linewidth pump for Raman lasers or amplifiers are preferred. This was shown in [54] where narrowing a pump laser linewidth from 5 cm^{-1} to 2 cm^{-1} increased the Raman gain of a diamond laser by 8%.

From equation 1.6 and 1.7 the optimum Raman gain g_s which is found at the centre of the Raman line where $\omega_s = \omega_L - \omega_0$ is found to be:

$$g_s = N \left(\frac{\partial \alpha}{\partial q}\right)^2 \frac{4\pi^2 \omega_s}{\mu_L \mu_s m \omega_0 c^2 \Gamma} \tag{1.9}$$

With a better understanding of what the gain in the Raman effect depends upon, we can explore the Raman gain in diamond. As the gain is wavelength dependent, paper [54] presents the gain found at several wavelengths. For example, at 1064 nm $g_s = 17\ cm/GW$, whereas at 355 nm $g_s = 78\ cm/GW$. This allows us calculate important parameters such as the pump power necessary for a Raman laser setup.

One part of the equation for the Raman gain that we have not explored yet is the dependence on the molecular polarisation. From [52, 55, 56] it is determined that the Raman gain g_s is proportional to the Stokes polarisation e_S, pump beam polarisation e_P and the Raman tensor R_i such that:

$$g_s \propto (e_S \cdot R_i \cdot e_P) \tag{1.10}$$

Thus, rotating the pump beam polarisation will have an effect on the gain coefficient, as the Stokes polarisation will depend on the highest gain coefficient available in the cavity.

For a diamond Raman laser the maximum Raman gain was observed when the polarisation of the pump was aligned with the <111> direction of the crystal which is the direction of the bonds between carbons in the material[57, 58]. Specifically in [57] it was found that a pump polarised along <111> had a Raman gain 1.33 times that found when the pump is polarised along <110>. An unpolarised pump has also been investigated in[56] and has been found to be less efficient and had a higher threshold compared to a polarised pump.

Reviewing the theory shown, it has given us the tools to calculate the expected Raman gain of a Raman laser setup and the threshold of such a system. Additionally, careful consideration as to the choice of pump laser source was deduced from the equation used to determine the Raman gain. Specifically, the linewidth of such a source and its polarisation were shown to affect the potential gain of a Raman laser setup. Further exploration of the theory behind the Raman effect and the proof for the equations presented here are given in the paper by A. Penzkofer et al. [53]. However, for this thesis, these are outside the scope of what will be presented here.

1.6.3 Examples of Raman systems in the eye-safe range

Having gone through some of the critical theory and concepts which govern the Raman effect we will review in this section some of the examples of setups which use the Raman effect in or near the eye-safe spectral region. Examples are drawn from a range of Raman platforms, including solid state, fibre-based, and self-frequency Raman systems, in order to illustrate achievable output power and performance. Particular attention is given where relevant to diamond Raman systems, which form the primary focus of this thesis.

Returning to the paper by Williams et al. [5], which reviews high-power diamond lasers, it is evident that high-power Raman lasers continue to achieve frequent breakthroughs, pushing the boundaries of what is possible in this field. Its review spans papers ranging from the first external-cavity CW diamond Raman laser reported in 2012, which achieved 10 W of pump-limited output power [59], to what was then the highest reported diamond Raman laser power of 750 W. This progression illustrates the remarkable rate of increase in power achieved in less than a decade. Indeed, a year later a paper from the same group reached the milestone 1.2 kW quasi-steady state laser power [51]. This is according to [5] powers which are 2-3 orders of magnitude higher than other Raman crystals operating at room temperature. Other Raman lasers based on Raman fibre architectures have been reported to reach even higher powers with one such paper [60] reaching powers of 3.89 kW at 1123 nm using a Yb doped fibre setup and bidirectional pumping. Higher powers have been published more recently in 2023 by the same group reaching a staggering output power of 10.7 kW at 1125 nm [61]. This uses a high-spectral-purity all-fibre ytterbium–Raman fibre amplifier (Yb-RFA) to achieve such a feat. Collectively, these works demonstrate the potential of Raman lasers for high-power applications, with particular emphasis on CW or quasi-CW diamond Raman lasers. This preference arises from the strong resistance of diamond to thermally induced degradation effects, which in other crystals can lead to reduced conversion efficiency and deterioration of beam quality under high-power operation.

Coming back to the eye-safe range and Raman lasers it has been difficult to reach the over 1500 nm bar as most common high power pump sources are those just under the 1072 nm target. Indeed the most common solid state high power sources used as a pump for Raman laser setups are Nd:YAG lasers which have a main output wavelength of 1064 nm. As such many papers either find other more difficult to deal with pump sources or have Raman output wavelengths of just under 1500 nm. One such laser presented in [62] exhibited a 21.8 W CW output power using a diamond Raman laser pumped by a 1080 nm Yb doped fibre laser which, when Stokes shifted twice, gave an output wavelength of 1516 nm. Other works with complex setups have also been reported such as a self-frequency Raman conversion in a Nd:YVO_4 Q-switched laser operating at 1342 nm described in [63]. This setup achieved an average output power of 2.2 W at 1525 nm with a repetition rate of 40 Hz which corresponds to pulse energies of 55 µJ. Another setup which uses self-frequency conversion can be found in [64]. This used a Nd:KGW Q-switched laser operating at 1351 nm to pump the Raman cavity achieving pulse energies of 31.8 mJ in 2 ns pulses and 10 Hz repetition rate with output wavelength of 1538 nm. In his thesis [65], Lukasz Dziechciarczyk presented a diamond Raman laser cavity which is the most relevant to the one discussed in this thesis. This setup achieved an output pulse energy of 130 µJ at 1515 nm with a repetition rate of 20 Hz when pumped by a Q-switched 1079 nm Nd:YAP laser. The performance of this setup was limited by thermal issue arising within the pump laser. Also reported in the thesis was a 13 W average power at 1521 nm diamond Raman laser with a repetition rate of 150 kHz and pulse duration of 12 ns. This was achieved by replacing the pump laser setup with an unpolarised Yb fibre laser setup emitting at 1082 nm. Another recent publication [66] using a compact Q-switched Nd:YVO_4/YVO_4 Raman laser has also achieved remarkable average power of 4.2 W with a pulse width of under 2 ns at a repetition rate of 50-150 kHz at 1525 nm.

This shows that already many different setups of Raman lasers have achieved powers and repetition rates that are almost, if not, reaching some of the aims set out at the beginning of this thesis. One side of Raman lasers, however, that will be investigated here is Raman amplification. Indeed, although more complicated than Raman lasers, Raman amplifier setups have the great advantage of being able to retain much of the characteristics of the seed laser. This is especially beneficial when you consider the wavelength consideration for LIDAR sources explored earlier as it would allow already existing narrow linewidth sources such as the fibre amplifier setups described in section 1.4.1 to reach powers they would otherwise struggle to achieve. One such example although not using a fibre laser as a seed is the 2015 paper by A. McKay et al [6]. This paper showed that it was possible to achieve a ratio of amplified to pre-amplified power (aka amplification ratio) of 5.8 by using a diamond master oscillator power amplifier setup. This setup used a Nd:YAG Q-switched laser as a pump which first got split by a 50% beam splitter to pump a 1.2 kW peak power 1240 nm diamond Raman cavity which will be referred to as the seed and use the remaining 50% of the pump power to pump a diamond sample at the same time as the seed to amplify the seeds' power. This allowed the resulting amplified seeds' peak power to grow to over 6 kW giving the 5.8 amplification factor. Although not at the eye-safe range due to being at 1240 nm, this is a paper which will be very important for the rest of the thesis.

1.7 Diamond Master Oscillating Power Amplifier Setup

The setup that will be introduced in this thesis was first presented as a proof of concept setup in the thesis of Lukasz Dziechciarczyk [65]. This original concept will be introduced briefly in this section The end setup and its results will be investigated and analysed in a later chapter, Chapter 3, to find its limitations and possible improvements.

As defined earlier the main goal of this thesis is to find a setup which emits a laser with high average power while also having high quality. Presented in the previous sections when compared with other available setups in the "eye-safe" range the Raman effect offers the possibility of reaching this range and additionally achieving high power and quality.

There are two main configurations of Raman laser cavities as shown in figure 1.4. Some as shown in some of the papers discussed earlier make use of the commonly used extra-cavity configuration[59, 62]. This is where the pump has a separate cavity which is focused into a stand-alone Raman cavity resonant at whichever Stokes wavelengths used. This configuration tends to be simpler to design due to being able to separately consider the mode size designs of both cavities.

An intracavity configuration by comparison, which was also used in some of the papers presented earlier, combines both the pump and emitting cavities into one[63, 64]. Although this doesn't change the threshold intensity required it does allow the emitting cavity to enhance the power at the pump wavelength due to the high reflectivities of the output couplers of most laser cavities. This does mean however that the mode size of both resonant wavelengths has to be taken into account when designing the cavity due to the wavelength dependence of the resonator mode parameters.

In this thesis the configuration used to achieve the goals presented was a Raman

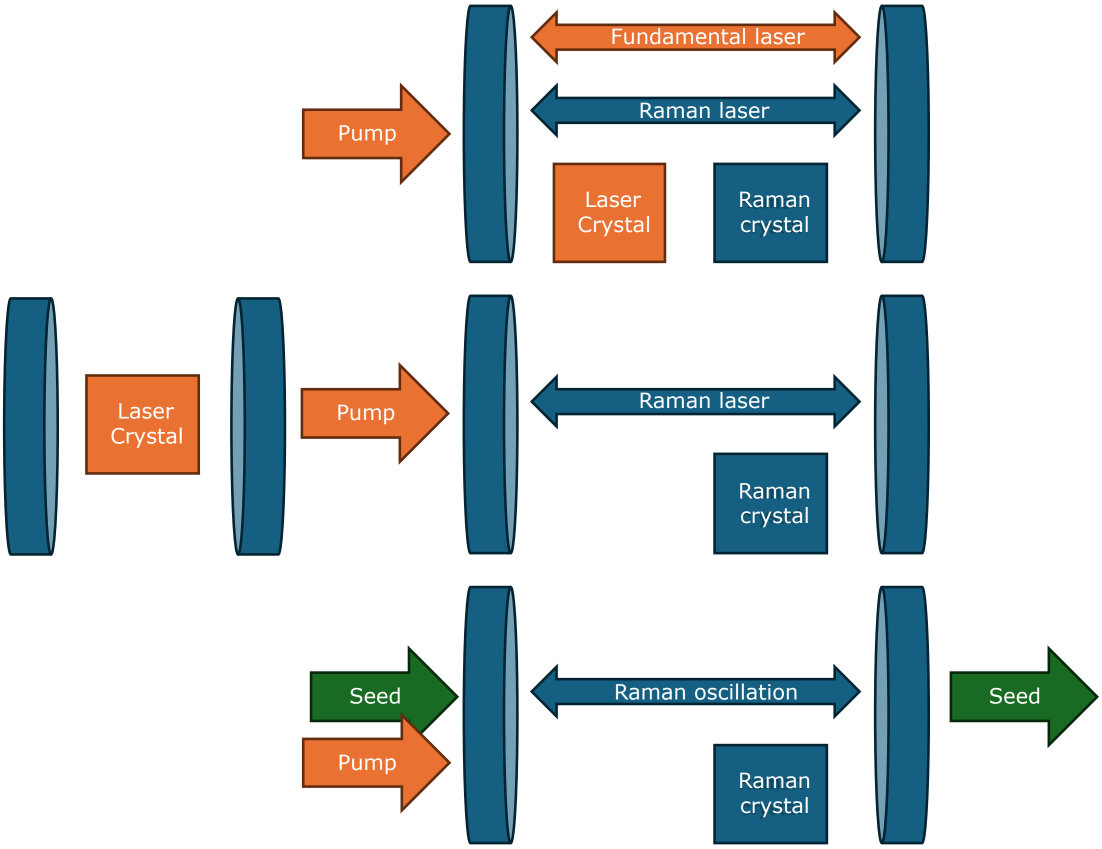

Figure 1.4: Diagram of two different types of Raman lasers and one Raman amplifier . The first showing an intracavity Raman laser where the laser crystal of the pump and the Raman crystal share the same cavity. Then a diagram of a Raman laser where the pump laser crystal and the Raman crystal are in two different cavities and finally a diagram of a Raman amplifier which this thesis will focus on.

amplifier setup. As shown in figure 1.4, unlike a Raman laser where a pump laser pumps the intra- or extra- Raman cavity which then emits its own laser, the Raman amplifier generates an intracavity oscillating field which then amplifies a seed laser. This allows us to take advantage of the unique qualities of the Raman effect to generate high power while not impacting the quality of the seed laser. A diamond master oscillator power amplifier (D-MOPA) was used as a proof-of-concept setup.

This setup differs from the other diamond Raman amplifier presented in this thesis [6] where, to maximise the potential amplification, an intracavity amplifier setup was chosen. This design decision gives us a setup consisting of three main parts. First is the pump source which was chosen to be a Q-switched 1079 nm Nd:YAP laser. The wavelength of which was especially important as, with diamond as the Raman crystal, a 2^{nd} Stokes shift above the 1500 nm target is reached (1515 nm). Second was the seed laser for which a 1515 nm distributed feedback diode (DFB) amplified by an Er doped fibre amplifier (EDFA) similar to those discussed early was chosen. Using an EDFA allows us to take advantage of its wavelength range but also its impressive linewidth and beam quality as presented in section1.4.1. A limitation of the D-MOPA configuration is the requirement for precise temporal synchronisation between the pump and seed lasers in order to achieve efficient amplification. Finally as already discussed a diamond crystal was chosen as the Raman crystal inside the amplifier cavity. The coating of the crystal was chosen to maximise the performance of the diamond Raman cavity and is reviewed in more detail in section 3.4.

A small correction to the earlier statement that the Nd:YAP laser is the pump is required. Indeed, although the Nd:YAP was used to pump the diamond Raman cavity, technically the pump of the MOPA is the intracavity first Stokes field which oscillates at 1261 nm when pumped by 1079 nm. This first Stokes field transfers its power to the seed which has a wavelength matching the second Stokes. This was achieved by carefully choosing the coatings of both input and output coupler to maximise the power of the first Stokes field while inhibiting any resonance of the second Stokes field so that a maximum amount of energy is transferred to the seed laser. This is because two Stokes shifts are required to achieve the “eye=safe” range amplification which was desired. This also had important consequences on the design of the cavity used which will be presented in more detail in Chapter 3. For clarity within the rest of this thesis the part referred to as the pump for the system will be the Q-switched Nd:YAP laser.

1.8 Conclusion

To summarise, in this thesis I will present a diamond master oscillator setup (D-MOPA) first shown in the thesis by Lukasz Dsziechciarczyk [65]. This proof of concept method shall be used demonstrate a possible way to reach the aims set by the requirements of LIDAR sources particularly for Doppler LIDAR used in external measurements. This application has stringent requirements for power, repetition rate, pulse duration, wavelength and linewidth which as shown in this Chapter have been difficult to attain. In particular, the need for both a high average power and quality source in the “eye-safe” range is something that conventional solid state lasers have not been able to reach, however, other solutions do exist. Several solutions were explored in the literature: fibre lasers, which can achieve high average powers and beam quality although typically not simultaneously at the levels required to reach the targets laid out in this thesis; optical parametric oscillators (OPOs), which are limited in average power due to the nonlinear nature of the materials and challenges in thermal management; and Raman effect based solutions, which is the focus of this thesis. I present a D-MOPA setup to take advantage of the qualities of the Raman effect especially in diamond shown by the high average powers achieved by many papers but also the conservation of the high quality of seed lasers in Raman amplifier setups.

In Chapter 2 we will first investigate the theory behind the power exchanges that happen within the cavity and attempt to model a Raman cavity so as to determine the optimum parameters to be used in a D-MOPA setup. In Chapter 3 the original setup and the results presented by Lukasz Dziechciarczyk will be explored with additional results being added to enable us to better ascertain the limitations and possible improvements of this setup. In Chapter 4 the design of the Q-switched Nd:YAP laser used to pump the diamond amplifier cavity will be highlighted and a novel 1083 nm Q-switched Nd:YAP laser will be presented. Finally, Chapter 5 presents an improved D-MOPA configuration, in which the optimisations developed throughout the previous chapters are combined. The resulting system is designed, built, and experimentally tested.

Chapter 2

Theory and Modelling of a resonant Raman cavity

To better understand and determine the design and parameters of a diamond Raman master oscillator power amplifier system, a computer program was created to model the energy interactions between the Stokes orders resonant within the designed cavity. This program is based on the model developed by Rini et al [67] of Raman interactions to calculate the change in energy of the various Stokes shift oscillating within the cavity depending on initial parameters such as input energy and pulse duration. The model was adapted for the intracavity Raman amplifier geometry considered here and implemented numerically in MATLAB. This not only gave an indication of the necessary design choices for the laboratory setup but also allowed us to explore scenarios that would not have been difficult to access experimentally.

In this chapter, we will present the theory of energy exchanges within Raman interactions, highlighting the associated assumptions and approximations. We will also describe the computer program written in the MATLAB coding environment that uses this theory to model Raman interactions within a cavity, detailing the chosen parameters. Finally, we will show the expected results of the program and clarify their implications for the design of an experimental setup.

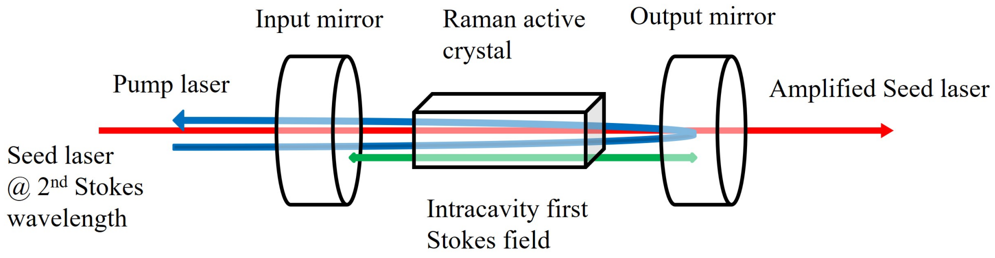

Figure 2.1: Diagram of the diamond amplifier cavity. In blue is the double passed pump laser, in green the intracavity first Stokes field and in red the seed laser with wavelength equal to that of the pump wavelength Stokes shifted twice.

2.1 Theory of power interactions within a Raman cavity

The Raman effect model that much of the work presented here is based upon is that presented in the papers written by Rini et al [67] and Ding et al [68]. In Rini et al the Raman effect is modelled in a fibre amplifier setup. Although seemingly very different from the D-MOPA configuration presented in Chapter 3, which is the focus of this thesis, both setups can be regarded as Fabry-Perot resonant cavities. As such they can both be described by the same set of mathematical equations. In the paper, the feedback elements of the resonant cavity are provided by fibre Bragg gratings whereas in the D-MOPA setup, mirrors form the diamond Raman cavity as shown in Figure 2.1. For both setups, however, the way to model the energy exchanges within the cavity is to first take an initial input of power (in our case the pump laser pulse) and then calculate the transfers of energy between the pump and the number of Stokes orders considered in the model. To ensure clarity in the explanation of the equations used to model the energy interaction the shorthand "Stokes" will be used to refer to the waves which have been shifted following a Raman interaction. A wave having experienced a single Stokes shift will be referred to as first Stokes.

One detail which sets apart the paper by Rini et al from preceding models is its inclusion of the interaction between co- and counter-propagating waves compared to only modelling co-propagating waves. This provides, from the results shown in the paper, a more realistic evaluation for the performance of the Raman effect within a Fabry-Perot resonant cavity. The equations that describe the evolution of the pump and Stokes power in a Raman active cavity can be described by a set of ordinary non-linear differential equations or ODEs. These equations specifically model the effect in "steady-state" and not in any transient Raman gain scenarios (ie sub ns timescales). The ODEs enable us to calculate the gain and losses of the intensities of the Stokes shifted waves inside the cavity.

$$\frac{dP_P^{F/B}}{dz} = \mp\alpha_P P_P^{F/B} \mp \frac{\nu_P}{\nu_{s1}} \frac{g_R^1}{A_{eff}^1}(P_{s1}^F + P_{s1}^B)P_P^{F/B} \tag{2.1}$$

$$\frac{dP_{sk}^{F/B}}{dz} = \mp\alpha_{sk} P_{sk}^{F/B} \mp \frac{\nu_{sk}}{\nu_{sk+1}} \frac{g_R^k}{A_{eff}^k}(P_{sk+1}^F + P_{sk+1}^B)P_{sk}^{F/B} \pm \frac{g_R^{k-1}}{A_{eff}^k}(P_{sk-1}^F + P_{sk-1}^B)P_{sk}^{F/B} \tag{2.2}$$

$$\frac{dP_{sn}^{F/B}}{dz} = \mp\alpha_{sn} P_{sn}^{F/B} \pm \frac{g_R^n}{A_{eff}^n}(P_{sn-1}^F + P_{sn-1}^B)P_{sn}^{F/B} \tag{2.3}$$

In these the superscripts F and B determine whether the wave is propagating forwards or backwards in the cavity. P is the power of either the pump detailed by the subscript p or a kth order Stokes detailed by the subscript sk and ν is their frequencies. A_{eff} is the effective area of the two beams involved in the equation and α is the linear attenuation coefficient. Finally g_R is the Raman gain coefficient which as described in section 1.6.2 scales inversely with wavelength. The equations provided can accommodate any number of Stokes shifts, with sn representing the count of Stokes shifts considered. Consequently, the number of equations will increase accordingly, as each equation computes the intensity of a single Stokes shifted wave resulting from its interaction with preceding and subsequent orders. Indeed the only difference between equation 2.2 and 2.3 is that there is no loss term for energy transfer between the kth Stokes order and the final Stokes order n. Of note in these equations is that, due to neglecting the contribution of spontaneous Raman scattering, the system does not have a unique solution. For example a possible solution would be where the pump is depleted totally only by linear absorption without any power being transferred to Stokes orders. To ensure this is not the case we introduced, as is suggested in the paper [67] and worked through in [68], an extra spontaneous scattering term in the equations: $K_{sp}(P_{prev}^F + P_{prev}^B)$. Here K_{sp} is a chosen constant that represents the percentage of spontaneous Raman scattered photons and the subscript *prev* shows that the power gained is from the previous power term such that the full equations become:

$$\frac{dP_P^{F/B}}{dz} = \mp\alpha_P P_P^{F/B} \mp \frac{\nu_P}{\nu_{s1}} \frac{g_R^1}{A_{eff}^1}(P_{s1}^F + P_{s1}^B)P_P^{F/B} \tag{2.4}$$

$$\begin{aligned}\frac{dP_{sk}^{F/B}}{dz} &= \mp\, \alpha_{sk} P_{sk}^{F/B} \mp \frac{\nu_{sk}}{\nu_{sk+1}} \frac{g_R^k}{A_{eff}^k}(P_{sk+1}^F + P_{sk+1}^B)P_{sk}^{F/B} \\ &\pm \frac{g_R^{k-1}}{A_{eff}^k}(P_{sk-1}^F + P_{sk-1}^B)P_{sk}^{F/B} + K_{sp}(P_p^F + P_p^B)\end{aligned} \tag{2.5}$$

$$\frac{dP_{sn}^{F/B}}{dz} = \mp\alpha_{sn} P_{sn}^{F/B} \pm \frac{g_R^n}{A_{eff}^n}(P_{sn-1}^F + P_{sn-1}^B)P_{sn}^{F/B} + K_{sp}(P_{sn-1}^F + P_{sn-1}^B) \tag{2.6}$$

Looking closer at equation 2.5 we will take some time to investigate what each term of the equation does. The first important detail, is that the sign of the terms depends on whether the forward or backwards propagating waves are being considered. Therefore, for a forward-propagating wave, the change in Stokes power over a small spatial segment in the Raman-active material experiences a loss due to the linear attenuation coefficient. This is a generalised term accounting for all the possible losses within a cavity that can affect a certain wavelength such that: $\alpha = \frac{2(R_1+R_2)}{L} + \alpha_{abs} \times L$. Where R is the reflectivity of the input and output couplers determined by the subscript number and L is the length of the crystal. α_{abs} is the absorption within the crystal. The next term calculates the power lost from the forward-propagating Stokes wave to the next Stokes shift within the cavity. The fraction of power lost is determined by the quantum efficiency, which is calculated from the frequencies of both Stokes orders considered, and the gain of the next Stokes shift over the effective area. Additionally, because this emission is stimulated, the existing power of the next Stokes shift, both forward and backward propagating, affects the power of the current Stokes order, explaining the presence of these terms in the equation. It is interesting to take a moment here to analyse how the effective area of the Raman effect is being calculated as it is deceptively more complicated than might be initially thought. Indeed, within the cavity different wavelengths will have different oscillating mode sizes and because of this different Stokes orders will have different mode sizes. Because of this the calculation has to take into account the overlap of each of the involved modes within the Raman active material such that: $A_{eff} = \frac{\pi(\omega^2(\lambda_{S,z})+\omega^2(\lambda_{F,z}))}{2}$ the working of which can be found in the conference proceeding by Y. Tsutsumi and M. Ohashi [69]. Where ω is the mode radius at position z for either the fundamental $\omega^2(\lambda_{F,z})$ or Stokes $\omega^2(\lambda_{S,z})$ wavelength. The last unexplained term represents the gain for the current Stokes order, which depends on the power of the previous Stokes order (or the pump for the first Stokes shift), the Raman gain of that previous order, and the effective area of the interaction.

Of course, these equations only model "ideal" conditions which can be extremely hard to replicate in a real world environment with for example the alignment of each element in the cavity being considered as perfect.

2.2 Introduction of the program

To achieve results which would help design an intracavity Raman amplifier setup, the model needed to be able to calculate the power changes of the pump pulse, the first and second Stokes pulses and a seed pulse as a function of the initial operating parameters which are presented in table 2.1. This was attained by modifying and improving upon a code used to model a second Stokes laser cavity that had been developed by Lukasz Dziechciarczyk and Florian Worme who were part of the same group as that of the author of this thesis. This code was written in the Matlab coding language. It uses a numerical solution approach to solving the ordinary differential equations that model the Raman effect from a list of defined initial parameters.

The code used can be divided into three parts as shown in figure 2.2. In the first stage of the code, the variables used in the remainder of the simulation are initialised. This includes parameters such as the Raman gain coefficient, the reflectivities of the mirrors and diamond surfaces, and the effective interaction areas, which are either specified as input values or calculated where required. The size of the output arrays is defined at this stage to allow efficient numerical propagation of the pulse dynamics, as preallocation avoids repeated memory operations during the iterative solution. These are then filled such that the initial power of each Stokes order is set to a starting noise

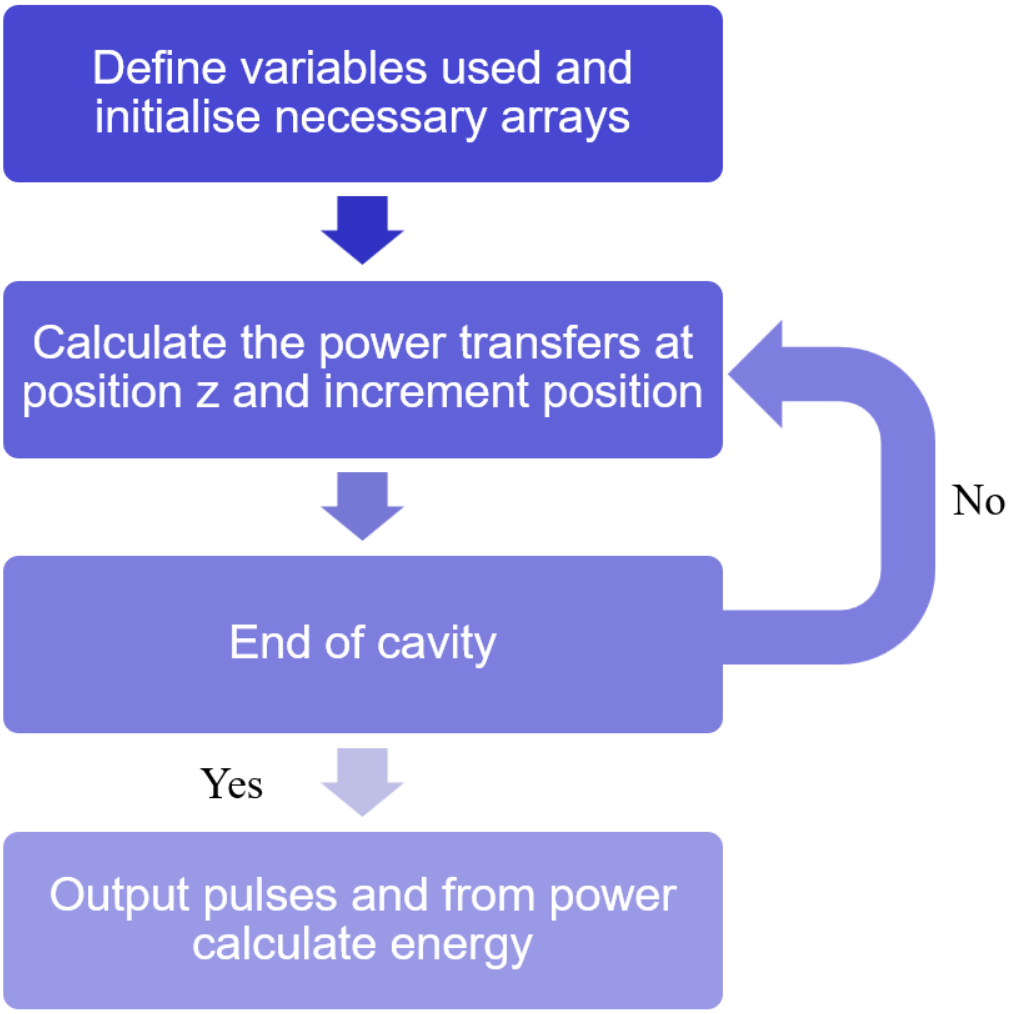

Figure 2.2: Flow chart of the organisation for the code used to model the Raman interaction between a pump, the first and second Stokes shift and a seed laser within the diamond Raman cavity.

value of K_{sp} described earlier. Its magnitude was chosen to be sufficiently small relative to the pump power to initiate Stokes growth without influencing the predicted steady-state behaviour. The step size used for the calculation dz is also initialised in this segment. It is defined by the size of the Raman active material and the speed of light in the material such that the simulation step is equal to three times the six sigma width of the Gaussian pump pulse divided by the time step defined by the time light takes to travel through one section, the size of which is chosen by the user, of the Raman crystal.

The next part of the code is solving the ODEs presented earlier to calculate the power exchanges in the cavity. Here the pump and seed pulses are initialised using the time step *dt*. This allows us to synchronise the temporal and spatial profile of the pulses such that one step in time for the pulses is equivalent to one step in position for the program. This allows the program to have the same spatial frame of reference as the model presented earlier where the ODEs modelled the changes in power in function of a change in space. As a result using the pulses initialised the program can calculate using the equations presented at each step the change in power of all the desired waves within the cavity until the predetermined number of steps is reached. This produces as an output an array with a spatial and thus temporal profile for each initialised wave.

The last part of the code deals with the processing of the output arrays and any analysis that was performed on them. First the outputs were smoothed using a Butterworth filter implemented using a predetermined Matlab function called butter where the cut-off frequency was chosen to be 215 MHz at a 3 dB point. This was used to reduce the spikes in the unfiltered simulated pulses and to emulate experimentally measured data where a 350 MHz photo-detector was used similar to what was done in [70]. Various analyses were performed on the results to quickly identify the key results such as integrating the outputs to find the pulse energy of each output and calculating the amplification ratio of the modelled cavity.

This structure allowed for flexibility in arranging the code to achieve results for any combination of parameters that would need to be tested such as different initial pump powers or different mirror reflectivities etc. The writing of the code was a cumulative effort from the group and myself. My contribution focussed on significantly reworking the code to get it to model a Raman amplifier setup and modifying parts of the code to optimise it and ensure it matched experimental results more closely.

2.3 Results

The aim of this modelling chapter is to explore different combinations of initial parameters and examine their impact. Since many parameters will be modified, the reference

Parameter	Value	Parameter	Value
K_{sp}	$1e^{-9}$	Refractive Index	2.45
Crystal Length	4 mm	Absorption	0.3 m^{-1}
Pump Wavelength	1079 nm	Input Coupler	[0.02;0.999;0.02]
Pump Diameter	144 µm	Output Coupler	[0.999;0.999;0.02]
First Stokes Diameter	189 µm	AR Coating	[0.032;0.005;0.003]
Second Stokes Diameter	203 µm	Seed Pulse Energy	90 nJ
Seed Diameter	70 µm	Pump Pulse Duration	21 ns
Gain at 1079 nm	16.7 cm/GW	Seed Pulse Duration	100 ns
Gain at 1261 nm	7.7 cm/GW	Pump Pulse Energy	100 μJ

Table 2.1: Table of the initial parameters used that best match the parameters of the proof-of-concept setup before any optimisations. In the reflectivity arrays, the entries are ordered as pump, first Stokes, and second Stokes wavelengths.

set of initial parameters is presented in Table 2.1. These parameters were chosen as they align with the characteristics that the lab setup was measured to have most closely.

Initially, the code was setup such that both the pump pulse and the seed pulse were initialised as a Gaussian pulse temporal shape. Although this is not completely accurate the temporal shape of a Q-switched pulse laser can be approximated as having a Gaussian shape. The seed laser, on the other hand, does not exhibit a Gaussian pulse shape. The pulse shape is determined by the electrically driven distributed-feedback diode and is influenced by the waveform of its voltage driver as well as by the response and stabilisation time of the diode. Unfortunately, due to the stabilisation time of the diode being longer than the desired pulse width, the shape of the pulse in the lab setup was double peaked with different amplitudes which is more difficult to model. Therefore, it was chosen to model the double peak as only an idealised Gaussian temporal profile with a full width half maximum of 100 ns which reflects better the ideal condition of the amplification coinciding with the peak of the larger of the two peaks.

As shown in figure 2.3 the seed laser in light blue has a wide Gaussian pulse where the peak of the pulse is temporarily matched with the peak of the 1^{st} Stokes power, in green in the figure, in the cavity. As the 1^{st} Stokes is where the amplification draws its energy, this is critical to ensure maximum amplification of the seed laser. A seed laser with a top-hat temporal shape was also modelled to reflect another setup which used an EOM to control the temporal shape of the pulse the details of which can be found in section 5.1.2. This is shown in figure 2.4. While only minor differences are observed between the Gaussian and top-hat temporal profiles, both pulse shape modelling results

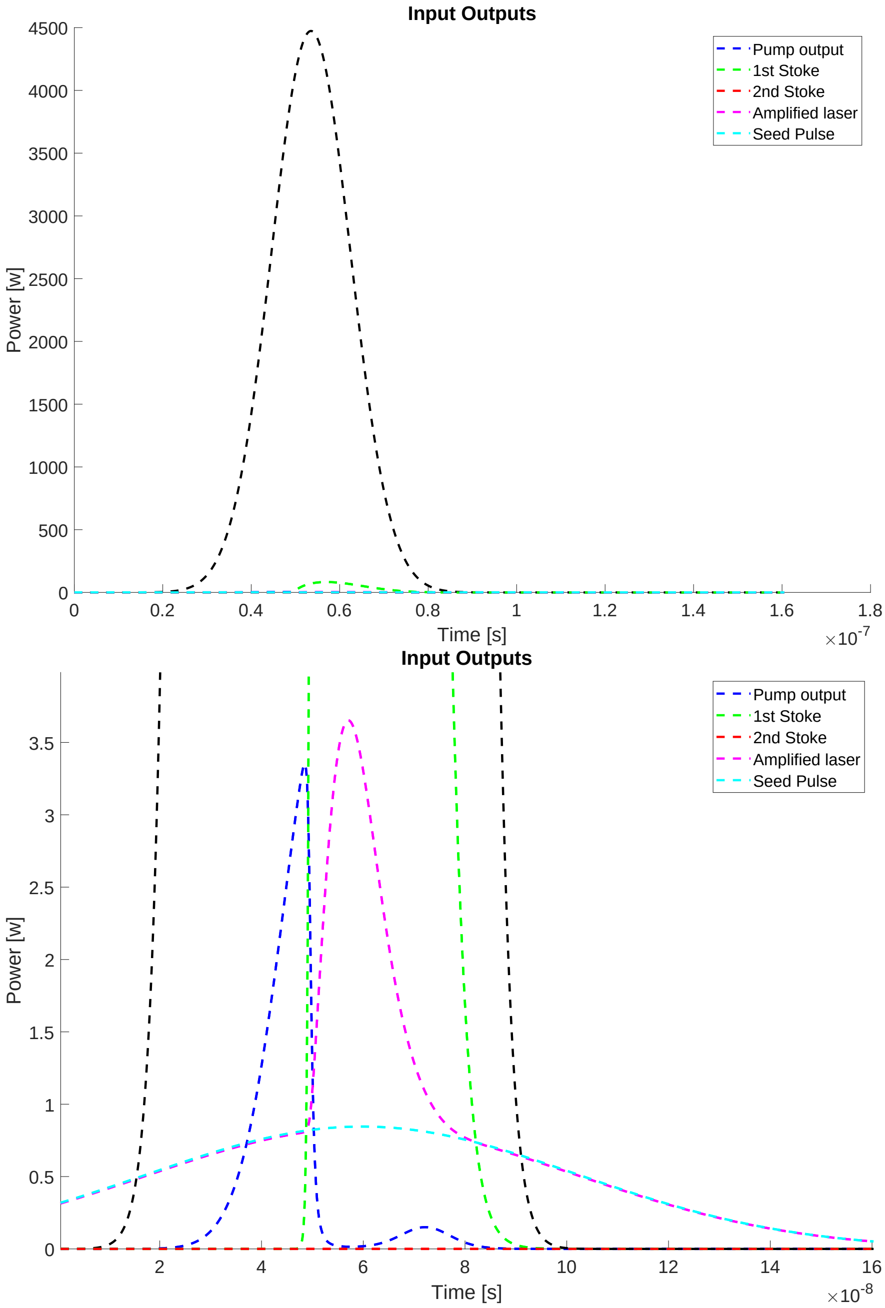

Figure 2.3: Graph of the different inputs and outputs of the program modelling the power changes within the amplifier cavity when the seed has a Gaussian shape. The bottom graph shows the same data as the top graph with a reduced y-axis range to emphasise the signal shapes.

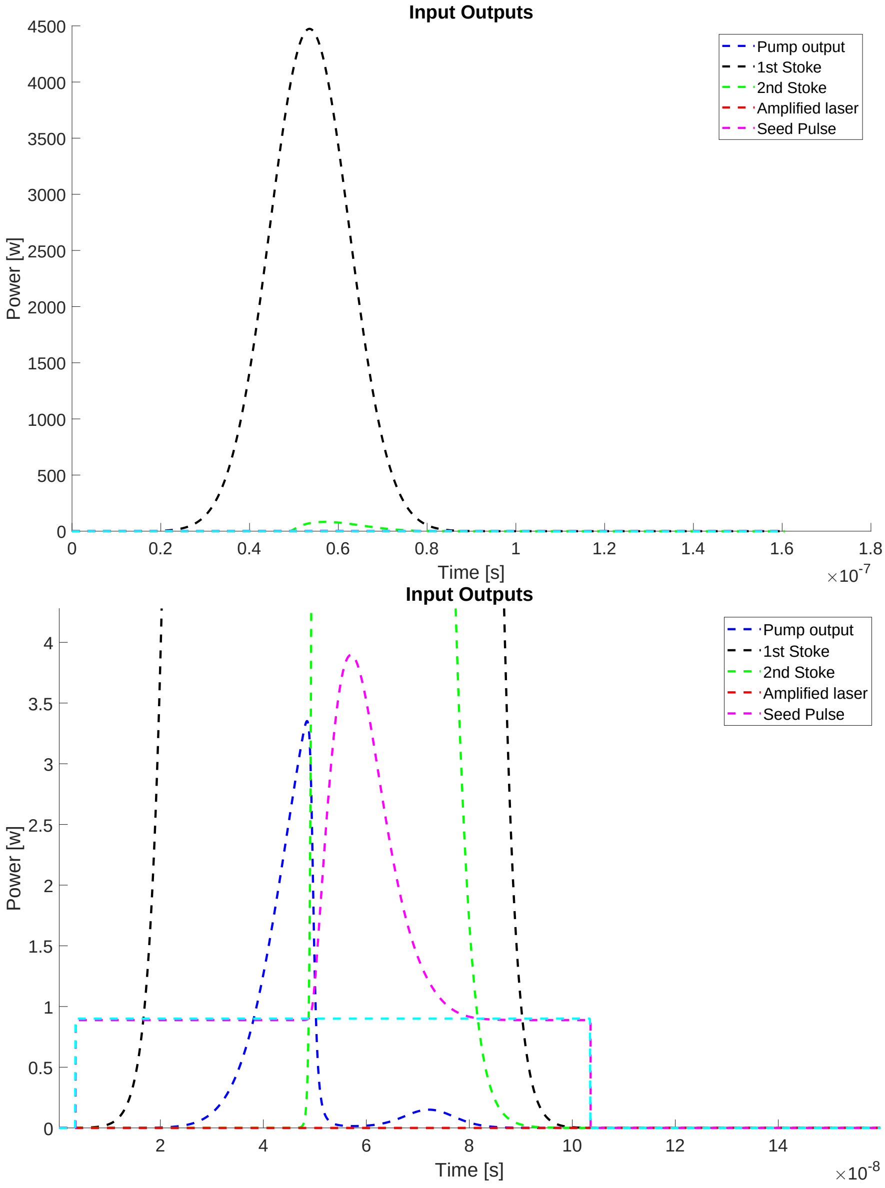

Figure 2.4: Graph of the different inputs and outputs of the program modelling the power changes within the amplifier cavity when the seed has a top-hat shape. The bottom graph shows the same data as the top graph with a reduced y-axis range to emphasise the signal shapes.

are included here to demonstrate the operating conditions experienced in the laboratory and to provide a reference point to the subsequent optimisation discussions.

In this thesis, the majority of the model results obtained using the top-hat seed pulse shape are presented, as these provide the most representative comparison with the experimentally optimised operating conditions. Certain results also make use of the Gaussian pulse shape, which will be indicated where relevant, as it influenced optimisation choices related to parameters in particular for determining the optimal pump to see temporal delay.

The first parameter that was investigated was the delay on the seed laser. That is the time difference between the peak of the pump and the seed laser. This was important as the seed laser needed to be temporally aligned with the 1^{st} Stokes power peak rather than the pump's. The delay was studied by analysing the impact that it had on the energy of the amplified seed laser output. This study allowed the optimal delay to be identified from the model results and provided a quantitative assessment of the sensitivity of the system to temporal misalignment, which is difficult to determine experimentally.

Figure 2.5 shows that the delay has a strong impact on the energy of the amplified seed laser. Especially when the seed has a Gaussian shape a difference in delay of 5 ns can reduce the amplified seed energy by almost 10% . By comparison when the seed laser is given a top-hat shape that same decrease is only found when the delay is over 20 ns. This makes it obvious that a top hat seed pulse minimises the degree of accuracy required to achieve optimal temporal alignment of the pump and seed pulses. As presented in Chapter 3 this temporal alignment was initially a major limitation of the system which was in part solved by changing how the shape of the seed pulse was determined.

Another parameter investigated was the length of the diamond crystal. Available to the lab were two diamond samples of quoted identical specifications other than the length of the crystal with one being 4 mm and the other being 7 mm. Due to the design of the cavity both crystals could be accommodated within it and the mode diameters of each relevant field were calculated and were found not to change significantly between the two crystal lengths. The design of the cavity and the mode sizes will be explored in more detail in Chapter 3. As such, an analysis to determine what might be the best possible length of an active crystal in such a cavity was examined. Thanks to the simulation, lengths other than the two available could be analysed and compared up to

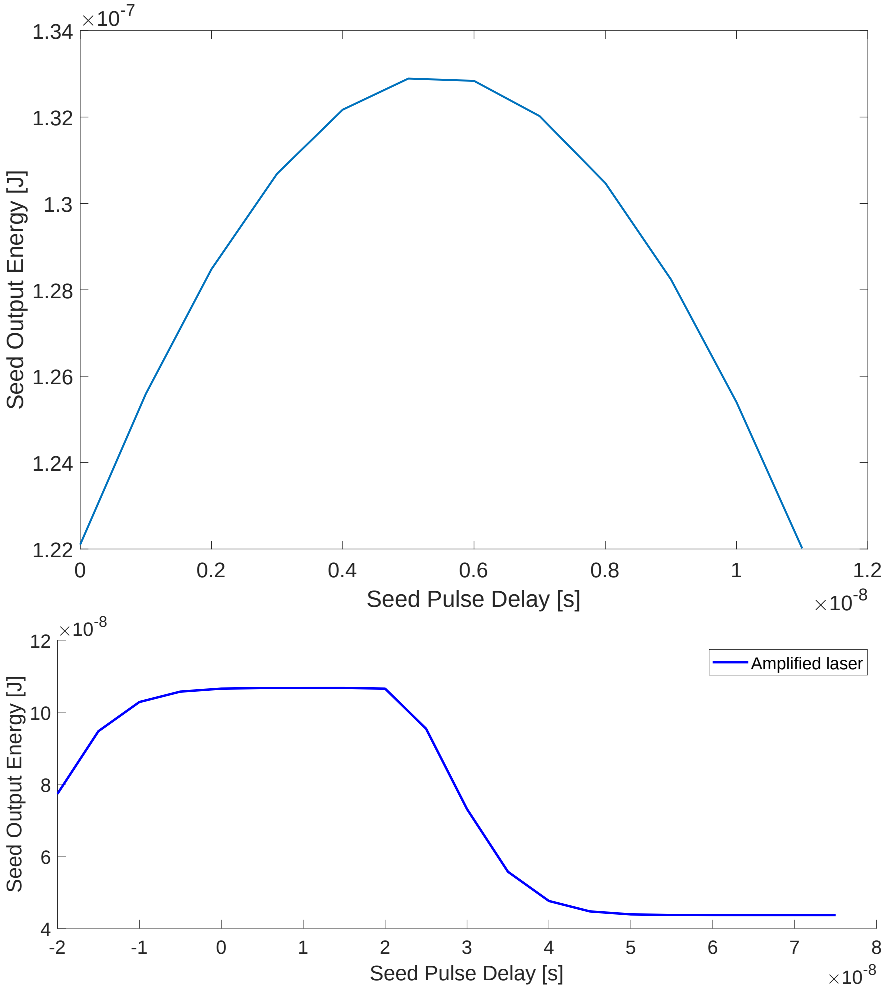

Figure 2.5: Above is a graph of the output energy of the amplified seed laser in terms of the delay parameter. Under is the same graph but instead of the input seed laser being given a Gaussian temporal shape a top-hat shape is used.

10 mm as after that the size of the cavity designed would be too small for the crystal. For all sizes tested here the mode sizes were recalculated and the losses incurred by the increased length was scaled using the per centimetre value quoted by the supplier of the samples ($0.005cm^{-1}$ at 1064 nm). In the lab the size of diamond crystals, as touched upon in Chapter 1 are currently limited by the CVD method used to synthesise them. However, this is an area of intense study allowing for ever increasing sizes of high purity diamonds which could enable further research in high power Raman laser cavities. [5]

From graph 2.6 it is immediately obvious the advantages that a longer crystal would bring. As the length of the crystal increases to 10 mm the amplification factor increases

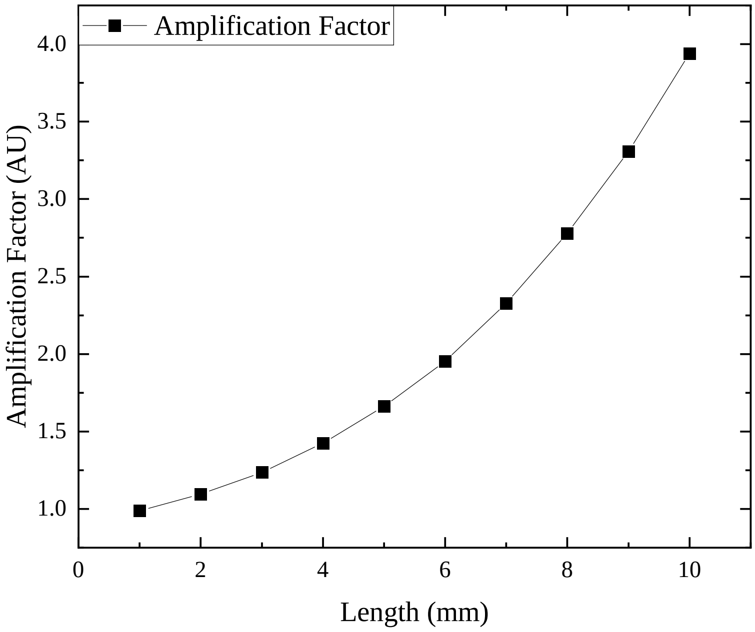

Figure 2.6: Graph of the amplification factor in terms of the length of the diamond crystal. All other parameters were left as default.

four fold. In this comparison the amplification factor rather than amplified seed pulse energy is used as it provides a value that was easier to measure in lab. For the model the amplification factor is simply the ratio of the pulse energy of the amplified output to that of the initial seed laser pulse. The increase was found to be cubic when fit with a polynomial. This fit is purely empirical and reflects the behaviour of the numerical model over the range studied rather than a theoretical scaling law. Over the length range studied, no clear saturation behaviour was observed in the model. These results are specific to the cavity design studied here and relies on the assumption that the per-centimetre absorption of all crystals, regardless of their lengths, are identical. This study made it evident that, within the cavity geometry considered, it would be better to use as long a crystal as possible.

The next parameters that were tested were the pulse energies of the pump and seed lasers in the D-MOPA. These parameters can be difficult to manipulate in real life to

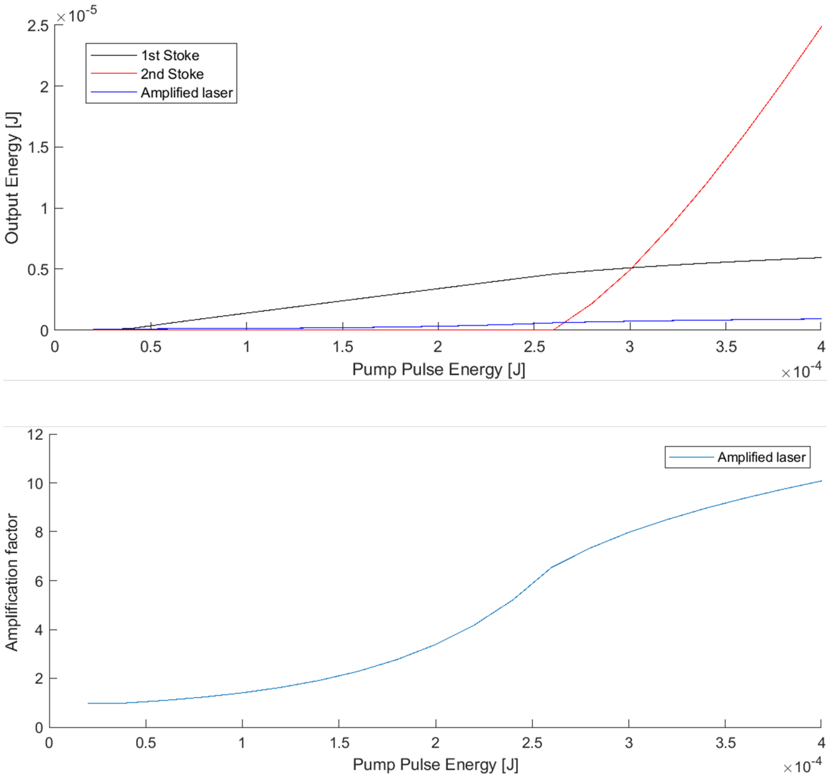

Figure 2.7: Top graph is the output energies of the various modelled outputs of the diamond Raman cavity in function of the pump pulse energy. Underneath is the graph of the amplification factor depending on the pump pulse energy.

extreme scales but are critical to inform the design of the setup. These pulse energies and their ratio play a crucial role in determining the system's performance. The ratio of the pump to seed power directly influences the pump depletion rate, a key factor in the overall efficiency of the setup.

For context, McKay et al. [6] demonstrate how design choices, such as strong focusing, can simplify the calculation of efficiency for the Raman effect. However, the design discussed in this thesis involves an intracavity amplifier, which prioritises achieving higher pump powers over maximising efficiency. This trade-off means that simple theoretical efficiency estimates are less directly applicable in our setup. As a result the model developed and the aforementioned program were used as a tool to determine the powers required to achieve the targeted results.

In figure 2.7 the pump pulse energy was modified from 0.2 µJ to 400 µJ in steps of 0.2

µJ. The top graph shows the evolution of the output energy of the 1^{st} and 2^{nd} Stokes and the output energy of the amplified seed while the bottom graph shows how the amplification factor of the amplified seed changes depending on the pump pulse energy. The initial seed energy in this case was chosen to be 90 nJ which was the estimated energy of the seed pulse in the lab.Both figures show the potential for high amplification is there with amplification factors of almost ×12 being theoretically achievable with pump pulse energy of 400 µJ which, as shown in Chapter 3, can be experimentally reached with the type of pump lasers considered. However, there is a limitation which affects the amplification factor and so the output energy. This limitation is the parasitic oscillation (Raman laser operation) within the cavity at the 2^{nd} Stokes wavelength. This oscillation is considered parasitic because, unlike the amplified seed laser, the desirable characteristics of the seed laser such as its spectral purity are not conserved. Indeed, once oscillation and/or output of 2^{nd} Stokes starts at around 250 µJ pump pulse energy, the curve of the amplification factor is altered to one which seems to tend towards a steady state. This is especially problematic as the design of the cavity in our case would need to be radically rethought to limit this effect due to it having the same wavelength as well as being collinear with the seed laser. As discussed in Chapter 3 this problem was also experienced in the laboratory and limited the potential of the intracavity amplification setup.

Having investigated the effect of modifying the input pump pulse energy we can do the same to the other input laser of the setup which is the seed laser. Using this we can observe the effect different seed laser energies will have on the performance of the Raman amplification cavity. To do this we set the pump pulse energy to one attainable in the lab and which was used for the early proof of concept testing of the setup of 100 µJ. This allowed both to observe the evolution of the amplification but also of the saturation of the cavity.

The seed pulse energy was varied between 0 and 200 nJ in steps of 10 nJ. From figure 2.8 it is evident that in this system the seed pulse energy required to saturate the cavity is not reached even when seed pulse energies are above what was available in our labs which was of the order of hundred nJ. Additionally, within this seed energy range, the

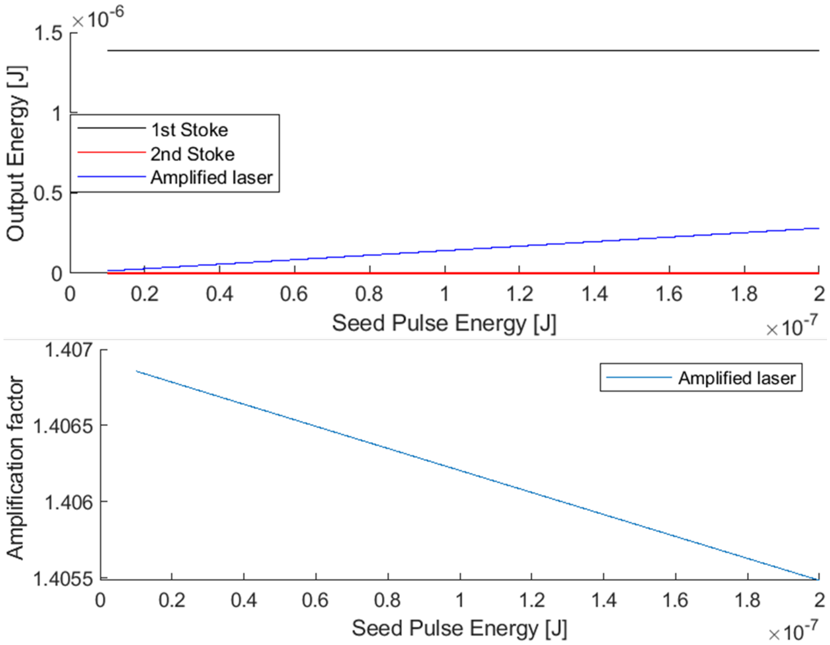

Figure 2.8: Top graph is the output energies of the various modelled outputs of the diamond Raman cavity in function of the seed pulse energy. Underneath is the graph of the amplification factor depending on the seed pulse energy.

amplification factor varies only by amounts too small to be perceptible in a typical lab measurement and was therefore not a concern. Further simulations were performed to find the point at which the depletion rate reached similar levels to those observed in [6]. To reach an extraction efficiency of the pump of approximately 50% it was found that the seed pulse energy would have to be of the order of 100 µJ ie. equalling that of the pump laser. This would notably impact the amplification factor; however, in this case, as we are trying to achieve a last stage amplifier setup, working within saturation regime does not necessarily pose a problem as the amplification factor is mainly used here as an indicator of performance rather than being a key design limitation in real-world applications.

The last parameter which was investigated using the program is the anti-reflection coatings within the cavity. This parameter is very difficult to change in the lab as it requires multiple different samples with different coatings. This is both very costly and time consuming. In comparison, this simulation gives the possibility to analyse in depth the consequences of modifying the coatings of all the elements within a cavity rapidly and without any cost. From existing papers [5, 68] the optimum input and output mirror coatings have already been determined and as such were chosen to maximise the first Stokes intracavity energy and minimise the second Stokes oscillation. This gave a reflectivity at the first Stokes for both mirrors of over 99.9% and at the second Stokes a reflectivity of less than 2% limited by commercially available mirrors. With the optimal coatings for the mirrors already being determined, the main focus of this set of simulations is the anti-reflection coatings of the diamond surfaces themselves. These coatings especially were very interesting as the coatings on diamond are known to be difficult to manufacture. In addition to this, the damage threshold requirements for the coatings in our setup made it impossible to have a complex coating which meant having to use an extended V-shape reflection curve. The consequence of this limitation was that only one wavelength could be minimised at the detriment of others.

As minimising the partial reflectivity (PR) of the coatings at all wavelengths was not feasible we instead used our program to determine which wavelength should be minimised to ensure maximum amplification. To achieve this goal, the reflectivity of the coatings was varied at the three critical wavelengths within the cavity: the pump wavelength of 1079 nm, the first Stokes wavelength of 1261 nm and the second Stokes wavelength of 1515 nm. The reflectivity of one wavelength was modified between 0% and 1% with steps of 0.2% while the reflectivities of the two other wavelengths was kept at 0.5%. For each combination of reflectivities, the pump pulse energy was also varied between 0 and 0.9 mJ in steps of 0.1 mJ to determine which wavelength had the most impact on the performance of the cavity.

This experiment yielded over 700 values and as such had to be synthesised and simplified for better clarity. As the aim of these results was to identify the wavelength reflectivity which had the greatest impact on the performance of the cavity, the output energy of the amplified seed was chosen to be the focus. To visualise the 180 output values of amplified energies results were separated by the varied reflectivity of each wavelength.

From figure 2.8 the variation in reflectivity which had the most impact was that of the reflectivity at 1261 nm. In addition to that, it is clear that the maximum amplified

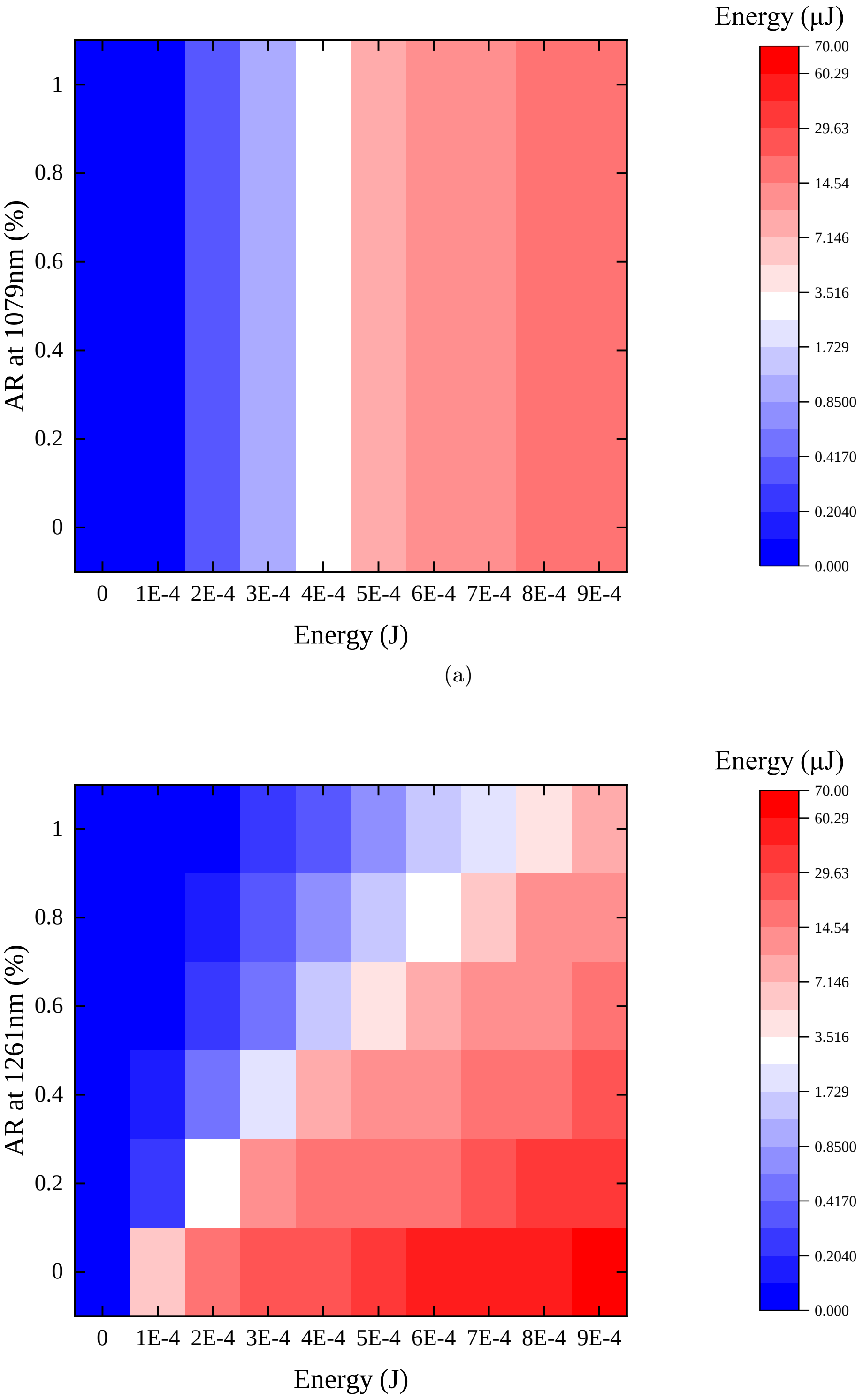
Energy (μJ)
70.00
60.29
29.63
14.54
7.146
3.516
1.729
0.8500
0.4170
0.2040
0.000
AR at 1079nm (%)
1
0.8
0.6
0.4
0.2
0
0
1E-4
2E-4
3E-4
4E-4
5E-4
6E-4
7E-4
8E-4
9E-4
Energy (J)
Energy (μJ)
70.00
60.29
29.63
14.54
7.146
3.516
1.729
0.8500
0.4170
0.2040
0.000
AR at 1261nm (%)
1
0.8
0.6
0.4
0.2
0
0
1E-4
2E-4
3E-4
4E-4
5E-4
6E-4
7E-4
8E-4
9E-4
Energy (J)

(a)

(b)

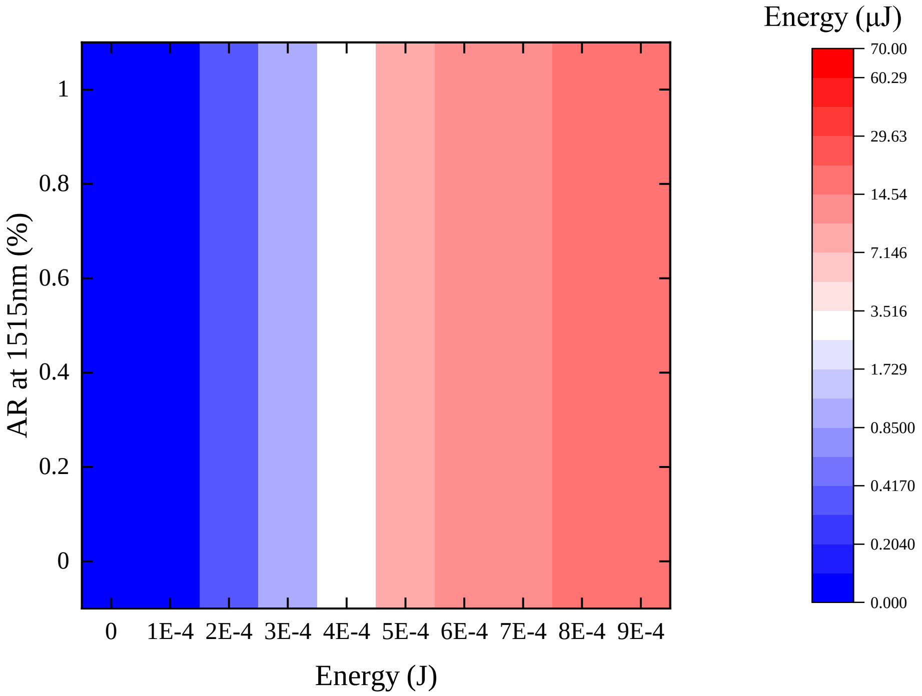

(c)

Figure 2.8: The series of heatmaps show the energy of the amplified seed laser output depending on the reflectivity of the AR coating on the diamond surfaces and on the pump pulse energy. a) is when the reflectivity at 1079 nm is varied, b) the reflectivity at 1261 nm and c) is at 1515 nm. On the heatmaps the energy is represented by a blue to red colour shift in a logarithmic scale from 0 to 70 µJ.

seed output pulse energy calculated was when the reflectivity of 1261 nm was 0%. This maximum energy was calculated to yield an amplification factor of ×724 at 0.9 mJ pump pulse energy. Although more difficult to figure out due to the large impact the first Stokes has, the reflection at 1515 nm was the second most important to minimise which is also reflected in our aim to minimise the second Stokes shift within the cavity. This is likely due to the resulting increase in parasitic second Stokes emission as the reflection is increased similar to what was seen in figure 2.7. From this, the choice was made to ensure the anti-reflection coatings on any diamond sample used were minimised specifically for the first Stokes and if possible, the second Stokes wavelength.

2.4 Conclusion

In conclusion, using the theory which models the Raman effect in crystals, I adapted and improved an existing program to better fit the setup in the lab and to calculate the amplification of a seed laser at the second Stokes wavelength in a Raman amplifier cavity. This allowed me to perform simulations to determine the theoretically optimal parameters for the in-lab setup. From this it was determined that the shape and timing of the seed laser were especially important. A top-hat temporal shape for the seed was found to allow for a more forgiving timing between the pump pulse and the seed pulse. Considering the difficulty in controlling the timing of a Q-switched laser this will greatly help improve the lab setup as is shown in Chapter 5. Another parameter which would have otherwise been expensive and laborious to analyse is the size of the diamond sample used in the setup. For the geometry of the cavity presented it was found that the longer the crystal the better the performance of the cavity. The simulations also allowed us to explore a wide range of energies for both pump and seed pulses which revealed that even with the precautions currently taken in the design of the cavity, such as limiting the pump pulse energy and the choice of coating reflectivities, oscillation within the cavity at the second Stokes wavelength and therefore emission of a second Stokes laser was possible at pump pulse energies of 250 µJ. Finally the program was used to investigate the effects of minimising the reflections from various wavelengths of the AR coatings of the diamond surfaces. This helped tailor the desired reflection curves of AR coatings on new diamond samples.

Naturally, the results of the theoretical model presented were primarily used to guide experimental decisions in the lab. It is important to acknowledge that these models are built on several assumptions discussed throughout this chapter, such as perfect alignment, fixed loss parameters, and the simplified treatment of spontaneous Raman scattering, which means their predictions may not perfectly mirror real-world outcomes. As such the next chapter will explore the initial setup that was used as a proof of concept and the limitation that were found, some of which have already been discussed in this Chapter.

Chapter 3

Diamond Master Oscillator Power Amplifier Proof-of-Concept setup

From the simulated results presented in Chapter 2, the theoretical potential of an intracavity Raman amplifier and the initial parameters for optimal operation were established. This chapter introduces an initial proof-of-concept setup, first presented by Lukasz Dziechciarzyk [65], used to investigate the practical feasibility of such a setup. It begins with the theoretical considerations and their implications, followed by a detailed description of the experimental design. The setup is then re-characterised by the author. The experimental methodology used to obtain amplification results is outlined, followed by an examination of results in Dziechciarzyk's thesis and additional findings that provide further context. Based on these results, and the modelling in Chapter 2, potential improvements are proposed. The results presented demonstrate that an intracavity amplifier is possible and lay the foundations for the experimental investigation presented in Chapter 4 and 5 of potential means to improve the experimental set-up.

To help visualise the comments and design decisions made during this chapter a simplified version of the D-MOPA setup is presented in figure 3.1. On the left of the diagram both the Nd:YAP pump laser and the EDFA seed laser setups are shown. Their emitted wavelengths, 1079 nm for the Nd:YAP and 1515 nm for the EDFA are represented by the coloured arrows emanating from the simplified boxes designating separate setups. The wavelength of the EDFA is chosen to match that of the 2^{nd} Stokes

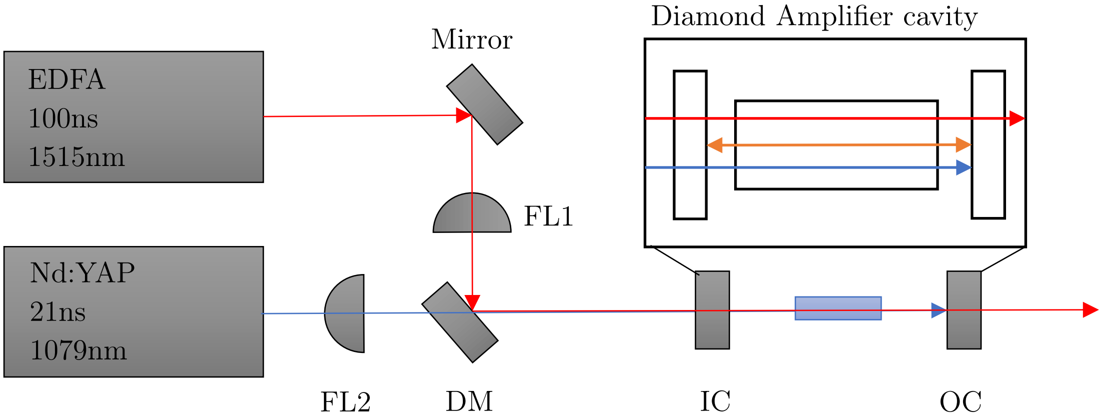

Figure 3.1: Diagram of the D-MOPA proof-of-concept setup simplified. In the figure FL stands for focusing lens and IC and OC are the input and output couplers. The three colours represent different wavelengths with: in blue the pump laser wavelength of 1079 nm, in orange the 1^{st} Stokes wavelength of 1261 nm and in red the seed laser wavelength of 1515 nm.

wavelength in a diamond Raman cavity of the Nd:YAP. In blue is the pump laser and in red the seed laser. The orange arrow within the cavity indicates the resonant 1^{st} Stokes wavelength at 1261 nm, which serves as the effective pump for seed amplification. For simplicity, the Nd:YAP source will continue to be referred to as the pump laser.

3.1 Pump laser considerations

The first component that will be considered is the pump of the D-MOPA. Due to the unusual aspects of this setup the pump setup had to be carefully thought through to ensure that it matches its requirements. Indeed, with the aim of reaching the eye-safe range of above 1.5 µm as the output, the wavelength of the pump needs to be carefully chosen. From equation 1.5 and knowing the Raman shift in diamond is 1332 cm^{-1} we can calculate backwards that a pump wavelength of at least 1072 nm is required to reach the eye-safe range assuming two Stokes shifts. As explained in section 1.6.2 the linewidth of the pump laser for optimal performance is required to be less than the Raman gain bandwidth in diamond of 2 cm^{-1} which at 1070 nm is 0.2 nm.

3.1.1 Material choice

The material that was chosen to perform the task of gain medium in our pump cavity was Nd:YAlO$_3$ more commonly know as Nd:YAP for neodymium doped yttrium aluminium perovskite. As discussed in the introduction a gain material more often used at around 1 µm is Nd:Y$_3$Al$_5$O$_{12}$ or Nd:YAG. The main reason for Nd:YAP over Nd:YAG was the pump wavelength required for 2^{nd} Stokes amplification at >1.5 µm, that is to say a pump wavelength of 1072 nm or more. Although the same Nd^{3+} ions are responsible for the laser transitions in both materials, the host crystal influences the exact emission wavelength because differences in the lattice environment modify the energy level spacing. Indeed, Nd:YAG has its highest emission cross-section at the wavelength of 1064 nm whereas Nd:YAP has it at 1079 nm. From our earlier calculations of the required wavelength with diamond as the Raman material we can see that 1064 nm would be under the 1070 nm target and would results in a 2^{nd} Stokes emission wavelength of 1485 nm whereas the 1079 nm emission of Nd:YAP would result in a 2^{nd} Stokes emission wavelength of 1514 nm. Although Nd:YAG does have other longer emission wavelengths such as 1077.9 nm which would reach our target, according to [71] its emission cross-section at this wavelength is of σ_e= 12×10^{-20} cm^2. Compared to $\sigma_e = 71 \times 10^{-20}$ cm^2 at 1064 nm [71], such an emission cross-section would require a more complicated cavity design to ensure that the 1077.9 nm laser would oscillate over the 1064 nm emission. Additionally, the emission cross-section of Nd:YAP at 1079 nm is of $\sigma_e = 46 \times 10^{-20}$ cm^2 [71], making it higher than that of Nd:YAG at comparable wavelength. Of note it is important to mention that Nd:YAP at 1% doping level of Nd^{3+} has an excited state lifetime of τ = 156µs [71], which is approximately 100 µs shorter than that of Nd:YAG. This potentially makes Nd:YAG a better choice for storing the energy for extraction in the Q-switch process. However, the wavelength consideration outweighs this characteristic.

The absorption spectrum for Nd:YAP is broad and has multiple peaks that are dependent on the polarisation of the pump due to the anisotropy of the crystal lattice of Nd:YAP. We choose to target the peak found at 803 nm that has a bandwidth of

7 nm with at 1% doping a 4.8 cm^{-1} absorption coefficient due to the ease in finding high power diode lasers with which to pump the cavity[71, 72]. Another difference which arises due to Nd:YAP being anisotropic versus Nd:YAG being isotropic is in how the heat deposited by a pump laser is managed. Indeed, in Nd:YAG, as discussed in section 1.3, the isotropic nature of the crystal means that heat deposited by the pump laser induces thermal stress, which leads to birefringence and consequently affects the polarisation of the output [25]. While stress-induced birefringence also occurs in Nd:YAP, the crystal is already strongly birefringent, so the simpler intrinsic birefringence dominates, and the more complex stress-induced birefringence has very little effect on the output. This can lead to requiring more complicated optics, for Nd:YAG based setups, inside the cavity whereas due to the anisotropic nature of Nd:YAP the output is already polarised. To summarise the performance of both crystals, Nd:YAG and Nd:YAP are similar with various difficulties arising for both materials however in the end the reason why Nd:YAP was chosen resides in its more suitable main emission wavelength.

3.1.2 Pulse Energy Requirement

To find the pump peak intensity required to reach the Raman laser threshold the following inequality needs to be fulfilled such that:

$$R_1R_2exp(2g_eI_pl) \geq 1 \tag{3.1}$$

Here R represents the reflectivities of the laser cavity's input and output couplers which can be assumed to respectively be $R_1 = 0.99$ and $R_2 = 0.8$. l is the length of the Raman crystal which, for a diamond sample, can be around 5 mm and g_e is the gain coefficient which as given in section 1.6.1 is of the order of 10 cm/GW depending on the wavelength. This requires that the pump peak intensity be above tens of MW/cm^2 to achieve threshold. For a focused pump beam, the corresponding peak power can be estimated by multiplying the threshold intensity by the beam area. This corresponds, for a pump spot focus diameter of approximately 100 µm, to a pump pulse peak power a little over 3 kW to reach the threshold of a Raman laser. From the literature, this estimate seems reasonable and consistent with what has been reported [6, 70, 73]. Therefore, assuming a pump beam diameter at focus of 140 µm, the reasons for which will be explained later in section 3.5 and a typical pulse duration of around 20 ns for a compact Q-switched 1 µm laser such as Nd:YAP, this implies a required pulse energy of 100 µJ to reach the necessary peak power of several kilowatts. Additionally, although the cavity configuration and parameters differ from those used in the modelling, the estimated threshold of approximately 50 µJ remains of the same order of magnitude, which provides confidence in the reasoning presented. To ensure that the conversion efficiency of the Raman cavity becomes essentially independent of the pump intensity, it is good practice to aim for 4 or even 5 times higher than the expected threshold intensity, as detailed in [74, 75]. This entails a pump pulse energy target for the pump laser of the desired set-up of approximately 500 µJ.

3.1.3 Q-switching theory

To achieve high average and peak power I chose to use a Q-switched laser. To better understand this choice and the design consequences that result from this the theory of Q-switching will be explored in this subsection. Q-factor in an optical cavity is a measure proportional to the ratio of stored energy to energy lost per oscillation cycle. A low Q-factor is a representation of a large amount of loss per round trip and therefore laser oscillation is extremely dampened and if low enough all the stored energy is lost to spontaneous emission. On the other hand, if the Q-factor is high, the round-trip losses are low, allowing laser oscillation to be sustained. In this case, the energy stored in the gain medium is extracted via stimulated emission with minimal spontaneous emission.

In a Q-switched laser during the period of low Q-factor the laser is pumped and energy is deposited within the lasing medium. Due to the lack of stimulated emission, this energy increases the excited state population within the laser gain medium following: $\frac{dN_2}{dt} = R_p - \frac{N_2}{\tau}$. Where N_2 is the excited state population, R_p the pumping rate and τ the lifetime of the excited state. To ensure that no stimulated emission occurs, even with low Q-factor, the time delay between pumping start and the Q-switch is set to the time needed to approach a maximum in the excited state population. This maximum is reached when the increase in excited state population due to pumping is balanced by spontaneous emission. When the Q-factor is switched, noise from spontaneous emission triggers stimulated emission which builds up quickly into a giant high energy pulse which causes most of the excited state population to be brought back down to ground state. The energy of this emitted pulse in a four-level laser material with a negligible Q-switching time is modelled by equation 3.2 [76]:

$$E = (\frac{\gamma_2}{2}\frac{N_i}{N_p}\eta_E)(\frac{A_b}{\sigma})h\nu \tag{3.2}$$

γ_2 is the loss at the output coupler i.e. its transmission, $\frac{N_i}{N_p}$ is the ratio of the initial excited state population when the q-factor is low and the excited state population at the peak of the Q-switched pulse. η_E is the energy utilisation factor such that $\eta_E = \frac{N_i - N_f}{N_i}$ with N_f the excited state population after the Q-switched pulse. A_b is the mode area and σ is the emission cross section of the gain medium and $h\nu$ the photon energy at the lasing wavelength. The expected energy of pulses achieved using the Q-switch method are of the order of mJ.

The duration of the Q-switched pulse defined in equation 3.3 is approximately proportional to the cavity photon decay time $\tau_c = \frac{L}{c\gamma}$ where L is the length of the cavity, c the speed of light and γ the logarithmic cavity loss such that:

$$\Delta\tau_p = \tau_c\frac{(N_i/N_p)\eta_E}{[(N_i/N_p) - \ln(N_i/N_p) - 1]} \tag{3.3}$$

Pulse durations for lasers using the Q-switch method are typically of the order of tens of ns.

3.2 Pump Laser Cavity Design

Having detailed what was required of the pump laser system, we then need to design the cavity itself. In a Q-switched laser cavity, there are several optical components that need to be considered. First, the input and output couplers and their respective radii of curvature are considered, followed by the gain material itself, which can greatly change the final characteristics of the laser, and its position within the cavity, which can also influence performance. And finally for a Q-switched system the component which allows

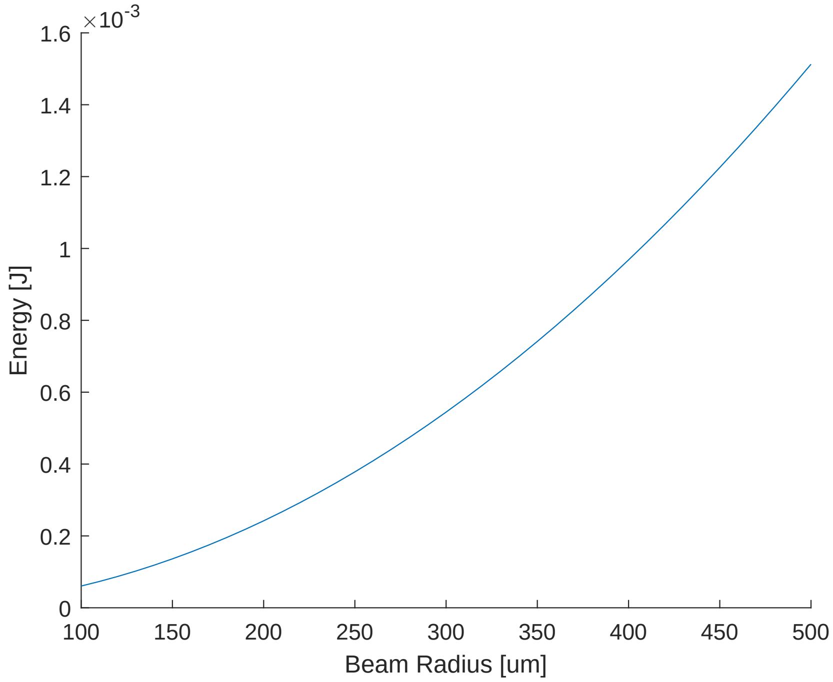

Figure 3.2: Graph of the calculated energy of a Nd:YAP Q-switched laser system in function of the beam radius.

for the quality switching in the first place, which in our setup will be an acousto-optic modulator or AOM.

Using the desired pulse energy calculated of 0.5 mJ we can determine the laser mode radius inside the cavity depending on the choice of output coupler and material. For this the equation for the pulse energy of a Q-switched laser equation 3.2 presented in section 3.1.3 can be used. Choosing an output coupler with partial reflectivity of 70% from the mirrors available to us, a curve of the pulse energy as a function of the mode radius can be modelled. Assuming a reasonable extraction efficiency of $\eta_E = 0.9$, in accordance with literature, which corresponds to a pumping ratio of $\frac{N_i}{N_p} = 3$ using the following equation from [76] $\frac{N_i}{N_p} = \frac{-\ln(1-\eta_E)}{\eta_E}$. With this value, along with knowing the emission cross section of Nd:YAP and the desired wavelength of 1079 nm, the curve can be calculated. Figure 3.2 shows the resultant curve. We can determine that to reach the 0.5 mJ pulse energy required, a mode radius of approximately 290 µm is required.

Before being able to decide on the position of optics within the cavity, the pump lasers for the Nd:YAP laser need to be considered. Due to the pump energy required in this setup and the available pump lasers at the time, double side pumping geometry for the laser cavity was chosen. This method, as the name implies, is where the gain medium is pumped from both sides simultaneously. An L-geometry cavity was chosen to allow for the double side pumping. Both diode lasers used to pump the gain medium had a fibre output and required a pair of lenses to collimate and focus the beam to the desired radius. This design decision also implied the addition of a dichroic mirror to redirect the 1079 nm output to its desired output path. The resulting geometry and position of the optics are shown in figure 3.5 which shows the full D-MOPA setup.

With the mode radius of 290 µm established and the constraints of the double-side pumping geometry taken into consideration, the cavity design can be determined using ABCD matrices. This is achieved with the help of an ABCD matrix modelling software (ReZonator). Using the software, and introducing within the modelled cavity all the optical components needed, the spacings of the components and the curvature of the input and output couplers can be modified to to ensure the oscillating mode radius matches that of the pump focus radius within the laser crystal. As the mirrors available to us were limited, a compromise was reached to have a mode radius of 330 µm. This design had an input coupler with radius of curvature (ROC) of 750 mm and an output coupler with ROC of 1000 mm with a total cavity length of 230 mm. The length was chosen to achieve a stable cavity while still being long enough to accommodate all the necessary optical components.

Stability of a cavity can also depend on the thermal effects that can be found in a cavity. Probably the most important effect that has already been introduced in Section 1.3 is that of thermal lensing. This is an effect whereby the deposition of heat in a material leads to localised changes in its refractive index which causes the material to act like a lens. To manage this, a quasi-continuous wave pumping scheme was employed. This approach uses pulses that are long enough (typically of the order of 100–300 µs, i.e. comparable to the excited state lifetime) to reach steady-state lasing conditions, while the low duty cycle coupled with the short on-time, relative to thermal diffusion timescales (which are of the order of µs to ms), keeps the average heat load manageable. This allows the system to achieve performance similar to continuous-wave pumping while reducing thermal stress on the gain medium. Furthermore, as the desired output of the cavity is pulsed, the pump laser only needs to last long enough to reach the Q-switch requirements making QCW pumping a more efficient and practical choice. Additionally, the Nd:YAP rod was placed within a water cooled copper block. This, although unlikely to have much of an effect on thermal lensing, does allow us to regulate the overall temperature of the material and reduce the likelihood of thermally induced damage.

3.3 Seed laser considerations

Due to the proof-of-concept nature of the setup and the magnitude of pulse energies required to achieve saturation within the cavity, as calculated in Section 2.3, the pulse energy of the 1.5 µm seed laser does not have as specific requirements as that of the pump laser presented beforehand. As the main concern for this setup was the feasibility of the concept, through measurement of the amplification ratio, there were no strict requirements on the seed pulse energy. The focus was not on achieving high efficiency or matching the performance targets outlined in the introduction. As such, the seed pulse energy used here was not intended to compete with the eye-safe laser examples presented in Section 1.4.

One aspect of the seed laser that did have stringent requirements however, was its wavelength. The wavelength of the seed laser has to match as closely as possible that of the 2^{nd} Stokes shift of the pump laser, in other words 1514 nm, to ensure optimal Raman amplification. Additionally, to ensure not only maximum performance as described in Section 1.6.2, but also the high resolution required for Doppler LIDAR as explored in Section 1.2 the linewidth of the seed laser should be as narrow as the Raman linewidth of diamond of 143 GHz or 1.5 cm^{-1} [54].

To achieve these considerations, a distributed feedback diode (DFB) amplified by an erbium doped fibre amplifier (EDFA) was chosen. A DFB was chosen, due to its excellent linewidth characteristics as quoted by the provider of $<$1 MHz , availability and tuneability around the desired wavelength of $\sim$1515 nm, and max CW output power of 10 mW. The tuning of the DFB was achieved by control of the operating temperature through a PID temperature controller. The DFB has a quoted ratio of 0.1 nm/°C giving a range of approximately 3 nm. Detailed measurements of this wavelength tuning can be found in section 5.2.2. As the max output of the DFB is still too low for the intended application further amplification is required. The EDFA was chosen to amplify the DFB as it has a large amplification bandwidth around 1.5 µm which allows it to overlap with the required wavelength of 1514 nm of the DFB. The DFB was coupled to the EDFA through spliced fibres. The design and setup of the EDFA was the work of our collaborators on this project at the University of Southampton the group of Pr. Johan Nilsson.

3.4 Gain material considerations

As already discussed in section 1.6.1 diamond was chosen as the Raman gain material in this setup due to its impressive Raman characteristics. Of diamond samples the most suited for Raman lasers and which show the best performance and characteristics are synthetic single crystal samples with as few defects and inclusion as possible. Therefore the diamonds used in the setup were single crystal synthetic samples of "optical grade plus" provided by Element 6. The grade is given and determined by Element 6 in their CVD diamond handbook [77] and designates a very low concentration of Nitrogen (20 ppb) and minimal birefringence ($<2 \times 10^{-5}$). These samples are typically grown using chemical vapour deposition (CVD) along the <100> direction. This gives a crystal sample with (100) oriented surfaces and (110) edges. These samples also have a very low quoted absorption coefficient of less than 0.005 cm^{-1} at 1064 nm.

Five 4×2×2 mm and one 7×2×2 mm diamond samples coated with an AR coating on the square surface of both ends of the rectangular prism, to minimise reflections at their surfaces, were available for this work. The AR coating on the surfaces was especially important as diamond has a high refractive index of 2.42. The coating chosen was focused on reducing the reflectivity of the diamond surface at three wavelengths (1079 nm, 1261 nm and 1515 nm) while minimising the chance of damage. As shown in section 2.3 as the wavelength with the highest impact is 1261 nm a single large range V-shape coating was chosen with minimum at approximately 1350 nm. This was done as, from

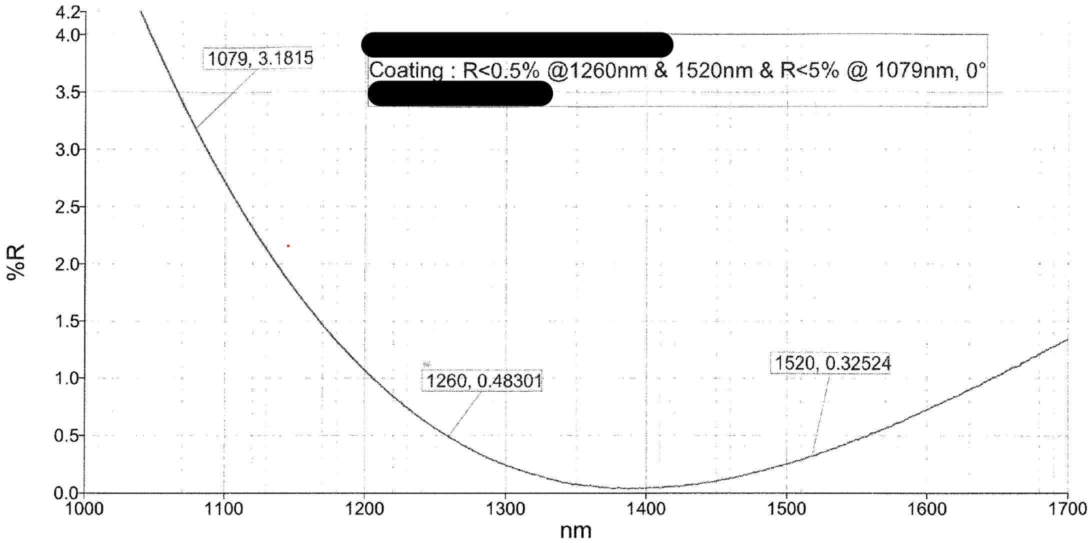

Figure 3.3: Graph of the engineered reflectivity, depending on wavelength, of the diamond surface when coated with its anti-reflection coating. The graph was provided by Lamda Photonics Inc.

the group's experience, multiple band coatings tended to have poor adhesion making it easier to damage. Further exploration of coatings and their damage thresholds can be found in section 5.3.3. The coatings were provided by Lambda photonics and had a quoted reflectivity of 3% at 1079 nm, 0.5% at 1261 nm and 0.3% at 1515 nm as shown in figure 3.3. The coating was observed to have a laser induced damage threshold (LIDT) of approximately 10 J/cm^2 [65].

3.5 Diamond Amplifier Cavity Design

From Chapter 2 it was determined that the energy of the intra-cavity 1st Stokes field is critical for the efficiency of the amplifier. The cavity therefore, was designed such that the 1st Stokes field, which, in this setup, acts as the pump for the amplifier, is maximised. The elements within the cavity are, compared to the Nd:YAP laser, relatively simple comprising of two mirrors and the diamond sample. This was chosen due to the power requirements to reach the Raman threshold and to minimise any potential losses within the cavity to maximise the potential amplification. As for the Nd:YAP laser, the cavity chosen for the D-MOPA was first modelled using the ABCD matrix software ReZonator.

From section 3.1.2, which detailed the requirements for the pump laser fluence required to reach the Raman threshold, it was determined that a pump focus diameter of 100 µm was optimal. This focus diameter was chosen to maximise fluence without making it too difficult to reach the required peak energy with the Q-switched Nd:YAP laser. Trying out the different available input and output mirrors in the software a plane input mirror and a curved output mirror with an ROC of 50 mm were selected. These provided the smallest mode diameter over the diamond's length. With overall cavity length of 11 mm to ensure stability, this gave at the middle of the 4 mm diamond mode diameters of 187 µm at 1261 nm and 202 µm at 1515 nm. This allowed both the 4 mm and 7 mm diamond samples to fit within the cavity and be stable. Additionally, there was only a

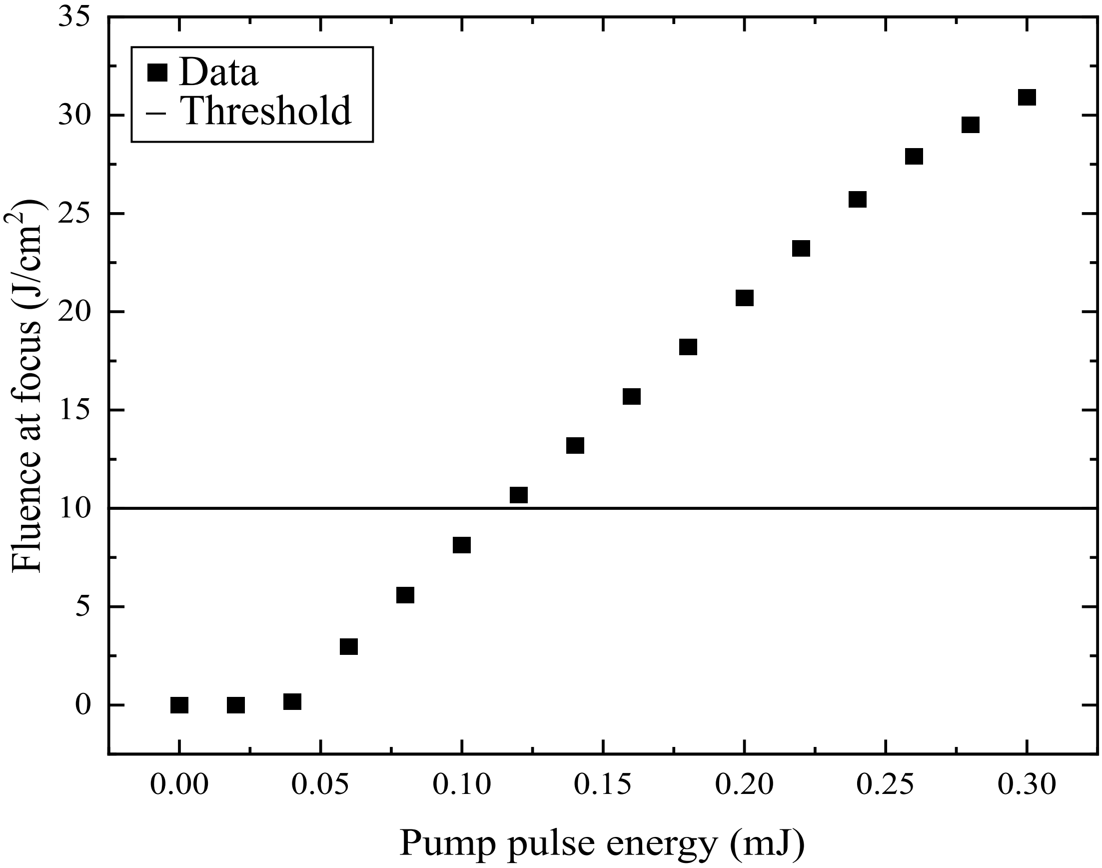

Figure 3.4: Graph of the fluence within the diamond Raman cavity depending on the pump pulse energy. The energy within the cavity was calculated using the simulation presented in Chapter 2 and compared to the damage threshold of the diamond AR coating.

small difference between the mode diameters at the middle of the 4 and 7 mm samples with the 7 mm being slightly smaller at 168 µm at 1261 nm and 189 µm at 1515 nm.

The optimal pump spot size for a 2^{nd} Stokes Raman laser cavity reported in Lukasz Dziechciarczyk's thesis [65], which considers a cavity design very similar to the one presented here, was used as a reference to refine the initially assumed pump focus diameter. In that work,a diameter of 150 µm was found to be preferable to the previously assumed 100 µm. This was because when focused too tightly it was found that the fluence within the cavity could surpass the damage threshold of the AR coating of the diamond. Knowing the pump diameter at focus and using the results of the simulation presented in Chapter 2 the fluence of the energy within the cavity can be found and therefore the available pump pulse energy before reaching the damage threshold of 10 J/cm^2. Figure 3.4 shows the evolution of the fluence within the cavity depending on the pump pulse energy. This was calculated by using the model to first find the output energy of the different wavelengths present in the cavity and then working out the intracavity energy since the reflectivity of the output coupler for all the wavelengths is known. In this context, the calculated fluence represents the combined contribution of the pump fluence and the intracavity energy from all oscillating wavelengths. From the figure we can see that the damage threshold is reached at a little over 125 µJ pump pulse energy.

3.6 Diamond Master Oscillator Amplifier Setup

The complete setup for the proof-of-concept D-MOPA setup, first presented in Lukasz Dziechciarczyk's thesis [65], is presented in detail in figure 3.5. This setup was re-characterised for this thesis, and the source of any measurements not retaken will be clearly indicated. The re-characterisation was performed to enable direct comparison with the model developed in Chapter 2 and to underpin the subsequent improvements explored in Chapters 4 and 5. The D-MOPA is composed of three main parts. First, is the Nd:YAP pump highlighted in green. This is a double pumped Q-switch laser cavity with an output coupler of 70% reflectivity at 1079 nm which is the main peak of emission of the Nd:YAP. The Nd:YAP is a ⌀3 × 5 mm rod with a 1at% doping.

An a-cut was chosen to maximise the emission cross-section at 1079 nm [71] and was provided by Crytur. The setup was chosen to have an L shaped cavity to allow for double side pumping. Two laser diodes were used as the pumping elements for the cavity with one being a Coherent FAP-808-25C-800-B and the other a unit from LIMO GmbH connected to pulsed current drivers (Newport ILX Lightwave and LIMO) to allow for them to be syncronised. These diodes were used in a q-CW regime with 20 Hz repetition rate and 0.47 ms pump on time to reduce the thermal load on the crystal. The cavity was operated in a Q-switched regime with LD1 (Coherent) at 25 A and LD2 at 20 A which resulted in a 0.23 W q-CW average power and a maximum measured pulse energy of 0.27 mJ measured just after the PBS in the setup. The Q-switch parameters are presented in the thesis of Lukasz Dziechciarzyk's as being found experimentally. The trigger delay was chosen to be 440 µs so as to maximise the output energy while minimising any other emission when the Q-switch is closed. The width of the Q-switch "on" time was determined to be 220 ns which gave an output pulse width of approximately 21 ns as measured on PD1. The characteristics of the laser are described in the thesis when under q-CW operation with a measured M^2 of 1.2 and a linewidth as measured on an optical spectrum analyser (OSA205C from Thorlabs) of less than 0.3 nm. The linewidth was achieved by introducing both a glass 2 mm etalon inside the cavity which width corresponds to a free spectral range of 74.7 GHz or 0.3

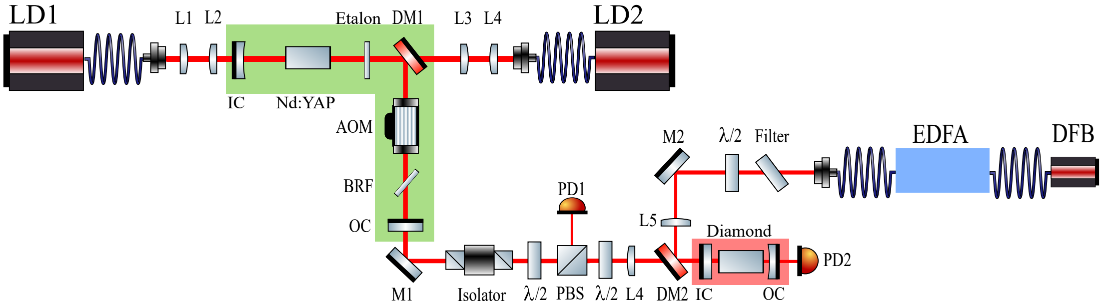

Figure 3.5: Diagram of the proof-of-concept D-MOPA setup. In green is the pump laser cavity, in blue the EDFA seed laser and in red the diamond amplifier cavity. In the diagram L stands for lens, IC and OC stands for input and output coupler, DM is for dichroic mirror and M mirror. AOM is acoustic optic modulator, BRF is birefringent filter and PBS polarising beam splitter. Finally LD is laser diode, PD is photodiode and $\lambda/2$ signifies a half-waveplate.

nm at 1080 nm and a quartz BRF for wavelength and polarisation tuning. After the Nd:YAP Q-switch cavity a couple of optical elements are inserted before the diamond cavity. First is a Faraday isolator to eliminate any reflections from any of the optical elements afterwards which could have an impact on the performance of the Nd:YAP. The half-wave plates ($\lambda/2$) and polarising beam splitter (PBS) perform several duties. As the output of the Nd:YAP is horizontally polarised this combination allows us to control the power going into the diamond cavity by rotating the first half-wave plate which directs the beam into PD1 by way of the PBS. The second half-wave plate also rotates the beam so as to align the polarisation of the pump beam with the <111> direction within the diamond to maximise the gain inside the cavity as discussed in Section 1.6.2.

The second part of this setup is the seed of the MOPA shown in blue on the diagram. This is composed of a DFB seed laser (EP1514-5-DM-B01-FA) provided by Eblana operating at 1514.5 nm with maximum power output of 15 mW with a linewidth of less than 1.5 MHz. The pulse width of the seed laser is 100 ns which is determined by the minimum possible pulse length of the precision pulsed current source (LDP-3811 ILX Lightwave) driving it. This laser is first pre-amplified in a custom made EDFA which was made by our collaborators Professor Johan Nilsson's group from the University of Southampton. The EDFA has three different distributed feedback diode lasers as pumps. The first operating at 1468 nm and the other two operating at 1473 nm in a CW regime with maximum power for each laser diode being around 160 mW. The peak wavelength of the EDFA gain bandwidth was adjustable using an etalon integrated within the EDFA setup. The pulsed current source of the seed laser was triggered from the same frequency generator as the AOM so as to more easily align the laser pulses temporarily. As shown in figure 3.5 the output of the EDFA was first filtered by a 1550 nm band pass filter with a FWHM of 12 nm angled such that its centre wavelength was tuned to that of the desired output. This is used to filter out any potential amplified spontaneous emission (ASE) or pump emission that might be output by the EDFA. It is then also polarised similar to the Nd:YAP laser using a half-waveplate so that the polarisation is parallel to the <111> orientation within the diamond.

The last part of the setup is the amplifier cavity itself. The pump and seed laser of the D-MOPA are focused by respective focusing lenses and combined into the cavity by a dichroic mirror. The diamond initially used in the results is a 2×2×4 mm sample. The plane input coupler was highly transmissive at 1079 nm and 1515 nm (R<2%) and highly reflective at 1261 nm (>99.9%). The curved (ROC = 50 mm) output coupler was highly transmissive at 1515 nm (R<2%) and highly reflective at 1079 nm and 1261 nm (>99.9%). The input and output couplers were chosen to achieve a high intracavity first Stokes field and inhibit any second Stokes oscillation. The mode size radius of the pump at focus was measured in air to be 72 µm.

3.7 Pump and seed characterisation

To measure the performance of the D-MOPA careful consideration had to be given as to what was exiting the cavity. Indeed, although the output coupler exhibits high reflectivity at wavelengths other than the desired 1515 nm was used, the output coupler did not completely eliminate the other wavelengths from the output. To properly monitor the desired wavelength rather than the others, two different methods were used. First, was to introduce optical filters with cut-on or off chosen to minimise the intensity of the unwanted wavelengths before the photodetector. The other method was to use a monochromator to isolate a desired wavelength just before the photodetector. The monochromator used in this instance was an Edmund Optics mini manual monochromator with a range of 750-1700 nm and input and output slits of less than 300 µm. The photodetector used was a Thorlabs 1000-1700 nm, 350 MHz InGaAs detector connected to an oscilloscope.

This oscilloscope, which was triggered temporally by the pump laser through PD1, made it possible to visualise the amplification of the seed pulse. This amplification can be measured by measuring the ratio of the area under the trace with and without the pump laser. The amplification mainly expressed as an increase in the seed laser peak height. Care was taken to operate the photodiode well below saturation to ensure a linear response to the detected optical signal. Additionally, using an energy meter (Thorlabs, ES11C) just before the second half-wave plate for the pump laser the input pulse energy of the pump laser can be measured.

1^{st} Stokes emission from the cavity was found to have a threshold at 80 µJ of pump pulse energy and became stable around 100 µJ. Due to the relatively low damage threshold of the diamond coatings and the difficulty in minimising the risk of damage when operating with high pump pulse energies, the experiments were conducted with pump energies in the range of 100 µJ to 150 µJ.

The choice of high reflectivity at the 1^{st} Stokes wavelength for the output coupler made the output of the cavity at that wavelength relatively weak. This made it difficult to accurately determine the intracavity first Stokes field energy as the instruments available in the laboratory were not accurate enough to measure the signal. This was in part due to both the small amount of output energy at that wavelength but also the low repetition rate of 20 Hz meaning that determining the energy from an average power reading was also difficult. An attempt was made with the pump pulse laser at 200 µJ giving an average power of 570 µW (28.5 µJ) however the meter varied greatly and is therefore unlikely to be accurate. It does however, give a similar order of magnitude for the pulse energy as the results calculated from the theory in Chapter 2.

The output of the EDFA pre-amplifier was measured to have a linewidth of less than 0.3 nm in CW regime. Under pulsed mode an average power of 100 µW was measured with the pumps for the EDFA set to 700 mA for the two pumps of the first and second stage of amplification (1468 nm and 1473 nm respectively) and 500 mA for the last amplification stage pump (1473 nm). Although the average power in pulsed mode of the EDFA is very high it is mostly due to the ASE driven by the pump lasers of the EDFA being run in a CW mode while the EDFA seed was run in pulsed mode. Due to this large background, it was difficult to measure the small pulse energy of the EDFA accurately. To circumvent this, as the exact energy of the D-MOPA seed pulse was not the point of interest in our experiments, the change in amplitude of the detector response was equated to the change in pulse energy and measured using a photodetector and an oscilloscope. The amplitude of the trace will then change proportionally to the energy of the signal.

3.8 Dziechciarzyk's methods and results review

This section will review the methodology and results found in the thesis of Lukasz Dziechciarzyk [65]. It is important to note that these results will be examined in closer detail as is usual in a review due to several reasons. First, much of the methodology used to obtain the results is reused in subsequent chapters and will serve as a benchmark for evaluating future modifications to the setup. Second, is that a lot of the parts within the setup stayed constant and thus their quality and performance can be reliably linked to the results in the thesis. Finally, some of the later results were obtained after the commencement of my PhD studies. Efforts will be made to clearly distinguish between the results generated by the research group and presented in Dziechciarzyk's thesis, and those that were carried out independently as part of my own work.

3.8.1 Seed characterisation results

From measurements shown in graph 3.6 the amplification of the seed laser of the EDFA was very dependent on its gain amplification range. The range is determined by the material chosen to supply gain to the system, in this case erbium, which has a natural gain range of 1530 to 1570 nm. As mentioned in the presentation of the EDFA setup, the gain bandwidth could additionally be tuned by use of an etalon integrated within the EDFA. Because of this the reported lowest seed wavelength possible to amplify in this setup was found to be 1514.6 nm. The power of the output spectrum however included 28% ASE. The value was found by calculating the ratio of the area of the spectrum intensity at 1514.6 nm to the intensity of the spectrum over a range of 1513-1537 nm.

One characteristic of the seed that is important to go into more detail is the tuning of the seed. To maximise the Raman gain in the diamond, the wavelength of the seed needs to be as close as possible to the wavelength of the 2nd Stokes wavelength. To achieve this, the temperature of the seed laser of the EDFA can be tuned which will modify the resultant wavelength of the laser at a rate of 0.1 nm/°C. This is shown in more detail in Section 5.2.2

The dependency of the EDFA on wavelength is further demonstrated by figure 3.6.

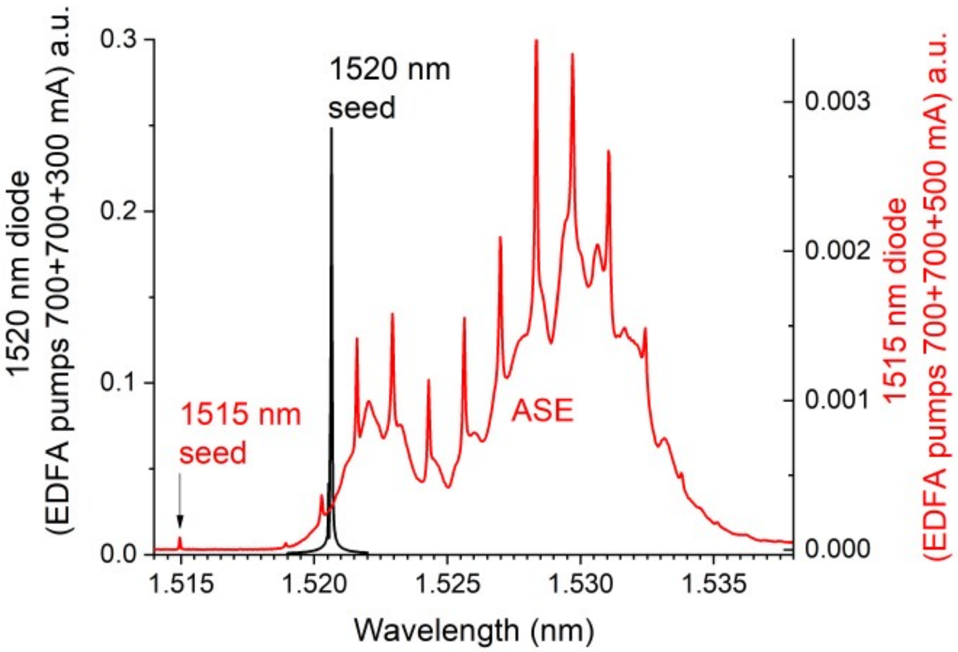

Figure 3.6: Graph of the EDFA output spectrum when seeded by two different wavelengths. The gain bandwidth of the EDFA was tuned for the 1520 nm seed but not for the 1515 nm seed showing the amount of ASE that results. Figure reproduced from [65].

In black is the spectrum of the EDFA output operating in a CW regime with a 1521 nm DFB laser as the seed adjusted to output 1520 nm. The pumps were set such that the first two lasers were driven by 700 mA whereas the third was driven by 300 mA. The etalon was adjusted to optimise the gain bandwidth of the EDFA so that the peak was at the same wavelength as the seed of the EDFA and the background was negligible. Comparatively the red curve shows the EDFA when seeded by a 1514 nm laser adjusted to 1515 nm. For this curve the pump of the last amplification stage was driven by 500 mA. For both, the seed laser of the EDFA was measured to have an output power of 6 mW. For the red curve, unlike the black one, the etalon was not tuned to maximise the EDFA seed wavelength. As a result, the seed laser peak is attenuated, and the spectrum is dominated by ASE. Additionally, this ASE has a range of 1520 nm to 1535 nm showing a preferential operating range of which the 1515 nm seed is outside of. As shown in [65], when the seed wavelength lies outside the centre of the EDFA gain bandwidth (e.g. around 1515 nm), the seed is only weakly amplified and the output spectrum becomes dominated by ASE rather than amplified signal.

The amplification measurements were performed with the 1514.5 nm DFB diode laser as the EDFA seed, as its wavelength closely matches that of the twice Stokes shifted Nd:YAP pump operating at 1079 nm of 1515 nm. This made it unfeasible to use the 1521 nm seed even though it had better performance for the EDFA. Further work will be presented in Chapter 5 to change the D-MOPA pump to take this into account and enable the use of the 1521 nm EDFA seed.

3.8.2 Proof-of-concept setup amplification results

The amplification was defined as the ratio of the areas of the photodiode temporal response for the 1515 nm cavity output when both the pump and seed were on and when only the seed was present, since this area is proportional to the pulse intensity and direct pulse energy measurements were limited by the available instruments.

The signal used is the average of 64 measurements using a photodetector after the monochromator taken using an oscilloscope, in order to minimise measurement noise

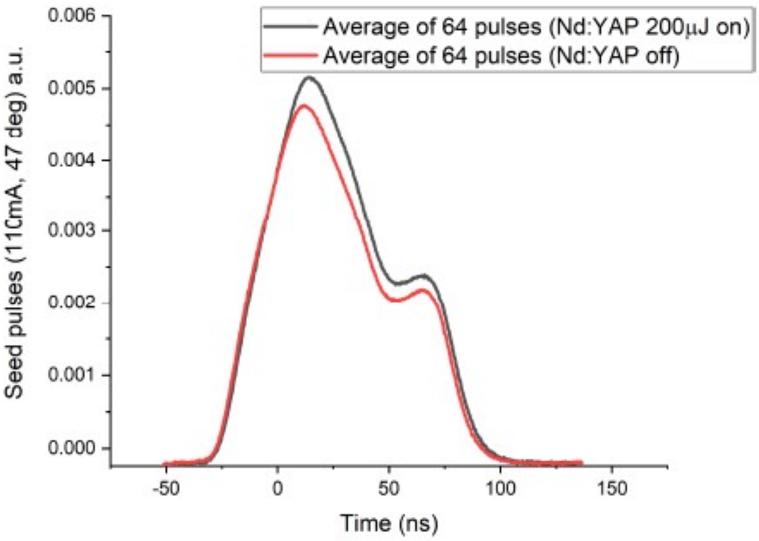

Figure 3.7: Graph of the average temporal response of the photodiode (in arbitrary units), proportional to the detected optical pulse intensity, situated after the D-MOPA cavity. In red is the curve when the Nd:YAP pump laser is off ie only the EDFA seed laser and in black with the Nd:YAP laser on ie when the seed laser is amplified. Figure reproduced from [65].

and random instability. The measurement of the signal was temporally triggered by the pump signal on the PD1 photodetector shown on figure 3.5 such that the timing of both signals are comparable. This gives a ratio which will be named amplification ratio.

This result shows that when using 200 µJ of 1079 nm pump pulse energy the setup was measured to have an average amplification factor of 1.08. During the measurement of this result, parasitic 2^{nd} Stokes emission was observed, manifesting as a weak peak around 1515 nm. As this 2^{nd} Stokes emission draws energy from the 1^{st} Stokes field, it potentially reduced amplification efficiency. To ensure that the measurement of the amplification was not affected by this, neutral density filters were added between the cavity and the photodetector. Although the 2^{nd} Stokes emission was weak and only the ratio of intensities was being measured, it was still possible to measure the amplification by reducing the 2^{nd} Stokes intensity until it disappeared from the measurement. It is likely that because of this some amount of error to the measurement of the amplification was introduced. This is explained in more detail in the thesis of Lukasz Dziechciarczyk

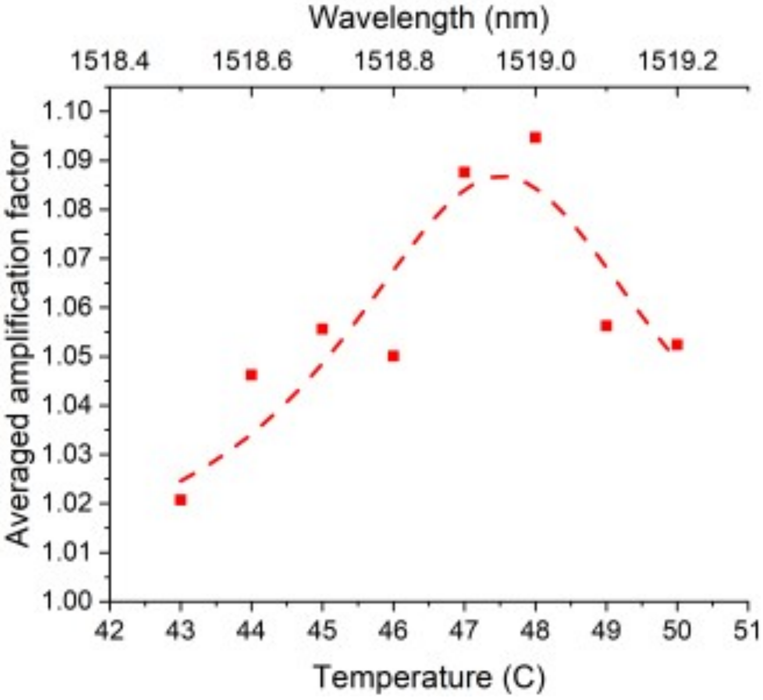

Figure 3.8: Graph of the measured amplification in function of the temperature and therefore wavelength of the DFB seed laser. A Lorentzian fit of the curve is also represented by a dotted line. Figure reproduced from [65].

[65].

To ensure that what was measured was the amplified seed, a measurement of the amplification as a function of the wavelength of the seed was performed. The wavelength of the seed was tuned by changing the temperature of the DFB using the PID controller. Due to the linewidth of the Raman effect, changing the wavelength of the seed laser should show the amplification factor diminishing when the wavelength of the seed laser is no longer aligned with that of the 2^{nd} Stokes. In graph 3.8, as expected, we can see that that is indeed the case with the amplification falling from almost 1.09 to parity proving that what was observed is indeed amplification. The dashed line in the graph represents a Lorentzian fit of the curve. This was found to have a full width half maximum of 0.5 nm which, when compared to the bandwidth of the Raman gain in diamond at 1519 nm of 0.4 nm, shows that what was measured can be assumed to be amplification of the seed. An improvement which could be made, would be to include more data points especially in the higher temperature area. This was limited in the experiment due to the damage threshold of the DFB of 50 °C. The large errors in the fit to the data points can be attributed to multiple factors. First the lack of baseline due to the small temperature range of the DFB but also the instability of the Nd:YAP laser which impacts the averaged amplification factor which shall be explored in the next section.

3.9 Re-Characterisation results and additional considerations

When re-characterising the setup for this thesis the amplification factor was measured again using the same parameters and an amplification factor of ×1.05 was found as presented in figure 3.9. Other characteristics were also measured to illustrate additional considerations.

One aspect of the results which merits further discussion is the temporal shape of the D-MOPA outputs. As shown in figure 3.7 the seed pulse has a double humped shape. This is due to how the pulsed current source driving the seed DFB was used. The current generator has a ramp-on time before it reaches a stable current output which is characterised by an overshooting of its target current and a dampened sinusoidal pattern around that target before reaching stability. As the pulse duration we were working with (100 ns) was lower than this ramp-on time, the shape of the DFB signal was affected. This is what gives the double humped shape. At this stage the aim was to characterise the limitations of the proof of concept setup rather than to optimise the drive electronics. Improvements to the seed pulse stability and timing are therefore discussed in Chapter 5. As mentioned in Dziechciarczyk's thesis [65] parasitic 2^{nd} Stokes emission was also an issue and ND filters introduced between the cavity and the photodiode were used to suppress it. One interesting aspect to point out is that the parasitic oscillation and emission of the 2^{nd} Stokes occurred at lower pump energies ($\approx 100\mu J$) than predicted by the modelling presented in Chapter 2 ($\approx 250\mu J$). This discrepancy is likely due to the effective reflectivity at this wavelength being higher than assumed in the model, as

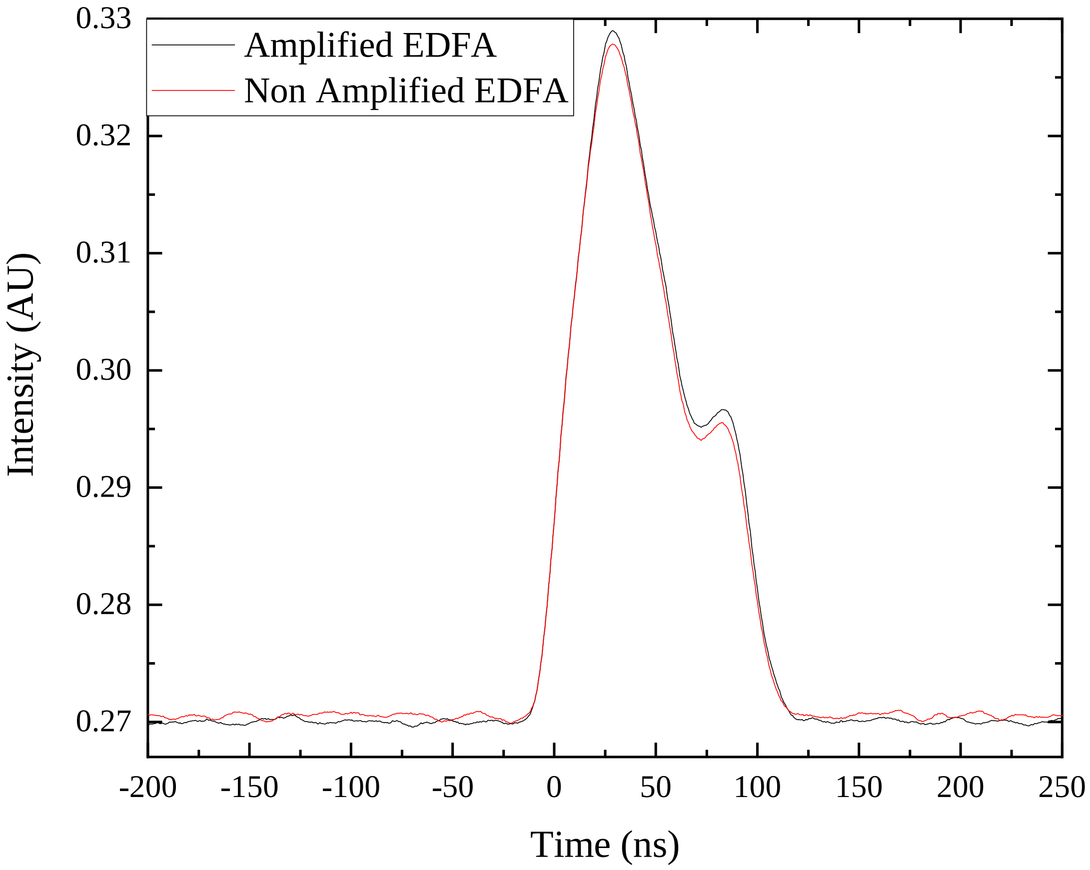

Figure 3.9: Graph of the average amplified and non-amplified proof-of-concept D-MOPA output taken when re-characterising the setup. These yielded an amplification ratio of ×1.05.

the anti-reflection (AR) coatings were specified only by nominal values.

Another aspect that made it difficult to measure the amplification factor, was the timing mismatch between the pump and the seed laser. This timing mismatch arises from the inherent timing jitter of the Q-switched pump laser, which causes random variations in the arrival of the 1^{st} Stokes field relative to the seed pulse. The delay was set up as detailed earlier in this Chapter by using a frequency generator which controlled the timing of the Q-switch and the timing of the pump of the EDFA. This mismatch and the double peaked shape of the seed laser made it complicated to setup an optimal timing that maximised the amplification. From Chapter 2 the delay of the seed to the pump is one of the crucial parameters that determines the efficiency of

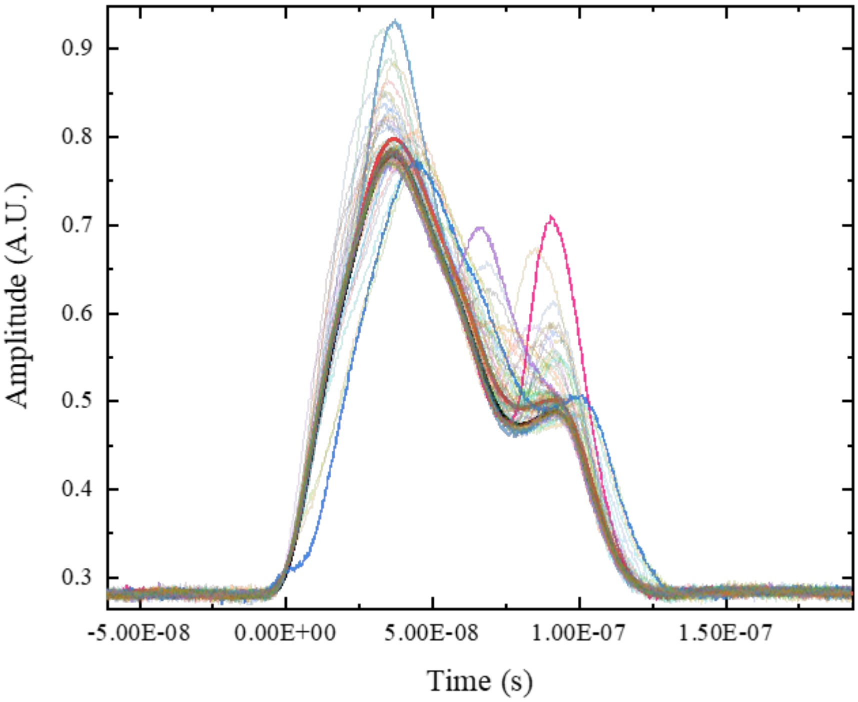

Figure 3.10: Graph of 64 amplified cavity outputs in function of time, their average and an unamplified cavity output. The thicker and opaque lines are the highlighted curves. In black is the unamplified output, in red the average amplified output and in colour (blue, magenta and purple) are three of the sixty-four curves highlighted to showcase extreme cases.

the system. This meant that on some pulses, the peak of 1^{st} Stokes field, which was expected to have a duration of 20 ns from the results in Chapter 2 and which was confirmed in the laboratory, was completely temporarily mismatched with the input of the seed. This can be seen in figure 3.10, which shows the traces of the averaged non-amplified cavity output (black curve), the averaged amplified output (in red) and the 64 single trigger traces which composed the averaged curves with certain traces being highlighted for clarity (other colours). This shows, that although the averaged outputs both amplified and non-amplified align well, the rest of the traces can vary significantly in their temporal characteristics. Indeed, if we take the peaks of the curves as amplification, we can see that this amplification is not always happening at the same time. This is due to the mismatch in peak 1^{st} Stokes field energy and peak seed energy. This reduces the calculated amplification ratio. As the seed arrival time varies by over 100 ns while the 1^{st} Stokes intracavity pulse width is only 20 ns, a longer seed pulse is required. With a pulse duration of 100 ns for the seed in this case, only one fifth of the pulse actually experiences amplification: as a result, the calculated amplification is proportionally reduced.

3.10 Conclusion

In conclusion, the innovative setup detailed in this chapter demonstrated a measurable amplification, exhibiting an average amplification factor of 1.08. However, the experiments also identified certain limitations which impacted the results significantly. Three primary limitations were found to affect the end results the most. Addressing these limitations will be crucial for further consideration and potential optimisations. Specifically: first the mismatch in the gain range of the EDFA and the current target wavelength of 1515 nm which limited the potential output energy of the seed laser and affected its spectral characteristics. Second, the emission of a parasitic 2^{nd} Stokes which impacts, not only the accuracy of the amplification measurement, but also the potential amplification in the cavity due to taking energy away from the intracavity 1^{st} Stokes field. Third, unoptimal parameters chosen due to instrument limitations such as the seed laser pulse duration, the timing jitter between the pump and the seed and the shape of the seed laser which, as shown in Chapter 2, have a great effect on the amplification factor. In the next Chapter, will first be investigated the wavelength and optimal EDFA amplification range mismatch and the implications this has on other components within the setup.

Chapter 4

D-MOPA pump laser improvements

As discussed in Chapter 3 although promising results were found using the proof-of-concept setup with amplification of the seed being measured several limiting factors were identified. One of the limiting factors, was the mismatch between the optimal amplification range of the EDFA (1520 nm to 1550 nm) and the wavelength of the 2nd Stokes shift in diamond (1515 nm) of the 1079 nm Nd:YAP pump. Changing the wavelength of the EDFA is relatively easy as it only requires a change of the seed of the EDFA, the DFB diode laser, from 1515 nm to a more suitable wavelength; however, as the seed laser wavelength and the 2nd Stokes wavelength need to be identical the pump wavelength of the Raman cavity needs to be taken into consideration as well. In this Chapter, the wavelength of the pump will be changed from 1079 nm to 1083 nm which yields a 2nd Stokes wavelength of 1521 nm which is well within the amplification range of the EDFA while still retaining the characteristics required for the setup detailed in the previous chapter. This was achieved by using a birefringent filter (BRF) introduced within the laser cavity. First, the fluorescence spectrum of Nd:YAP crystals will be investigated and the necessary considerations explained. Then, the theory of tuning components such as a BRF will be introduced and how such components can tune the wavelength of a laser. The new setup will be presented using models like the ones used to design the previous Nd:YAP pump as well as a program made in house to simulate the transmission spectrum of a BRF to justify its choice and characteristics. Finally, the characteristics and the results from the setup will be presented.

4.1 Tuning an Nd:YAP laser

Changing the wavelength of the EDFA is obtained by changing the DFB diode laser currently pumping the EDFA to a more appropriate wavelength such as the 1521 nm one as shown in graph 3.6 presented in section 3.8.1. This allows for greater amplification within the EDFA and better spectral purity of its output. This is beneficial as it leads to greater amplification within the Raman cavity due to the Raman gain bandwidth being 0.4 nm at 1521 nm. It is also a requirement for targets set in chapter 1 which should be kept in consideration even if this is only a proof of concept setup. An additional benefit, is that the extra average power gives a better signal to noise ratio for the D-MOPA amplification ratio measurement.

A consequence of changing the wavelength of the seed of the D-MOPA is that it will no longer match the wavelength of the 2nd Stokes shift when pumping the diamond Raman cavity with a 1079 nm Nd:YAP pump laser. Therefore a new pump needs to be designed to ensure that both wavelengths align. Fortunately another advantage that came from choosing Nd:YAP rather than Nd:YAG is that Nd:YAP has the potential for lasing at other wavelengths as shown in [78–80]. As the polarised emission spectra in [81] show, there is the potential to access a wider range of emission wavelength through the choice of crystal cut and laser polarisation. Notably the results of the paper show that a b-cut crystal pumped along its a or c-axis has an emission peak at 1083 nm with an intensity around a quarter that of the main 1079 nm peak. Although this drop in intensity is large, a 1083 nm laser emission would result in a 1522 nm 2^{nd} Stokes wavelength which is very close to the 1521 nm DFB diode laser discussed above and well within the tuneability range of the DFB. As shown in [78], designing and building a laser at the 1083 nm wavelength is possible; however, Q-switch operation which is critical to achieve the threshold for Raman lasing was not achieved.

The design used in [78] was based on an etalon to tune the wavelength dependant losses within the cavity and the use of Cr^{4+}:YAG saturable absorber to obtain passive Q-switch operation. In addition, the cavity and crystal itself were kept short to keep the oscillating laser mode size small and the cavity stable. Lasing was shown at 1083 nm and other wavelengths during CW operation of the pump laser. Q-switched operation at 1083 nm however, was not achieved as, due to high output coupler reflectivity of 94% and additional saturable loss of the Cr^{4+}:YAG crystal, the laser would revert to emitting 1079 nm. For the use presented in the previous chapter however, high energy pulses are critical to reach the threshold energy required therefore the setup presented is not suitable. One solution to this would be to use a birefringent filter also known as BRF. As described in the Waritanant and Major paper [82] that describes the theory and presents a multi-wavelength tuneable Nd:YVO_4 laser, a BRF introduces an increased discrimination between "low loss" and "high loss" wavelengths compared to something like an etalon. This is especially important as it demonstrated the possibility of tuning to emission peaks that were significantly less intense by only using a single optical component in this case a BRF. This solution has the potential to be applied to an Nd:YAP setup to achieve tuneability and even Q-switch operation at 1083 nm. To achieve this, the theory behind such a setup will first be explored focusing on birefringent filters and how they enable such tuning.

4.1.1 Birefringent filter theory

A birefringent filter is an optical component usually made of quartz which, due to the birefringent effect intrinsic to the material, will introduce wavelength dependent polarisation changes. These polarisation changes, when coupled with a polarising element, will introduce wavelength dependent losses the mechanism of which shall be explained here. To better understand what that means we will first explain what birefringence is and why this has such an impact on light. Birefringence describes the dependence of the refractive index of the material on polarisation with respect to the crystal orientation. In more technical terms, the interaction of an incident beam with the material will result in a phase retardation between the ordinary ray (o-ray) travelling with polarisation perpendicular to the optical axis and the extraordinary ray (e-ray) travelling with polarisation in the direction of the optical axis. By combining this effect with the polarisation selectiveness of a surface angled at the Brewster angle defined by the material, a wavelength dependent filter is achieved. Additionally this also limits the

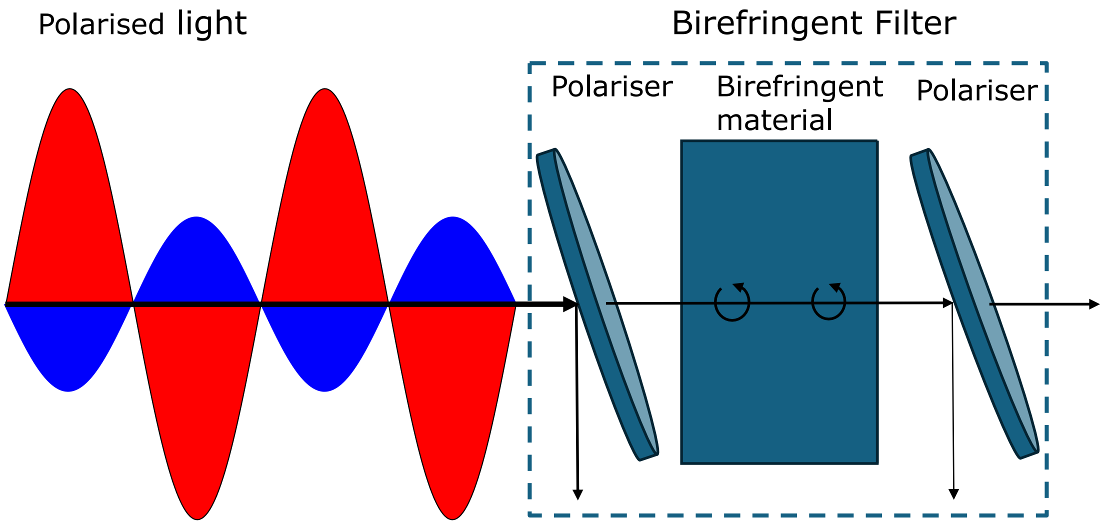

Figure 4.1: Diagram of the components that can be thought to make-up a birefringent filter set at Brewster's angle. The first Brewster surface selects the polarisation, while the birefringent plate introduces a wavelength dependent phase delay so that the second Brewster surface produces wavelength dependent transmission, forming the filtering effect.

losses for one of the polarisations at the surface of the optic components.[83]

From the description given a birefringent filter can be thought of as a birefringent material sandwiched between two polarisers as shown in figure 4.1. This can be found in the theory as well where using Jones matrices the wavelength dependent transmission of a birefringent filter can be calculated. From the paper Naganuma, Lenz and Ippen and surrounding literature [82, 84, 85] the losses experienced by a beam interacting with a BRF can be modelled by a series of Jones matrices such that:

$$M = \begin{pmatrix} 1 & 0 \\ 0 & q \end{pmatrix} \begin{pmatrix} \sin\alpha & \cos\alpha \\ -\cos\alpha & \sin\alpha \end{pmatrix} \begin{pmatrix} 1 & 0 \\ 0 & e^{i\delta} \end{pmatrix} \begin{pmatrix} \sin\alpha & -\cos\alpha \\ \cos\alpha & \sin\alpha \end{pmatrix} \begin{pmatrix} 1 & 0 \\ 0 & q \end{pmatrix} \tag{4.1}$$

To better understand what equation 4.1 represents we will separate the matrices representing the polarising effect and those representing the birefringent effect.

The two outer matrices model the losses at the surfaces at Brewster's angle which will impact no loss to the 'P' polarised wave whilst the amplitude of the 'S' polarised wave will be multiplied by $q = 2n/(n^2 + 1)$. Here, n represents the mean refractive

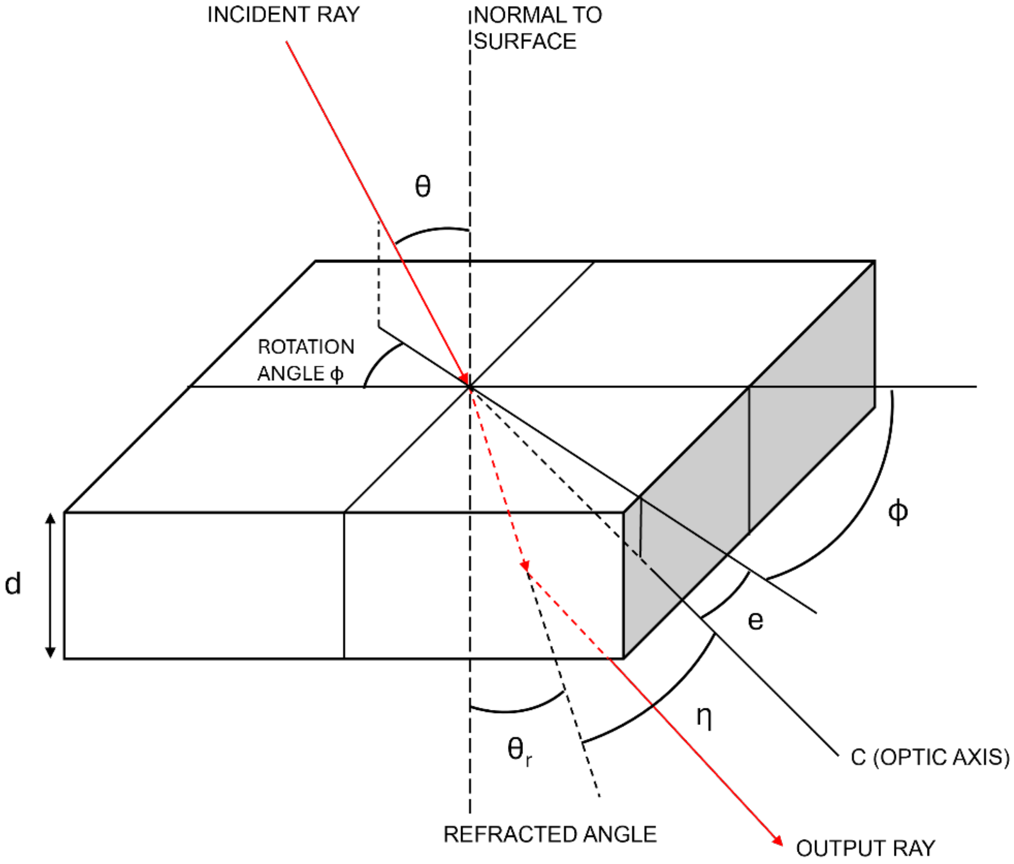

Figure 4.2: Diagram highlighting the different angles made by a ray interacting with a birefringent filter. These angles are critical to understanding the theory behind the transmission of a birefringent filter.

index of the material, which implies that $q < 1$, indicating a loss.

The matrices in the middle, meanwhile, will affect each beam polarisation differently depending on the angle α and the phase retardation δ. The angle alpha is the azimuthal angle between the plane of incidence and the plane containing the optical axis and the refracted ray such that :

$$\cos\alpha = \frac{1}{\sin\eta\sin\theta}(\cos\phi\cos e - \cos\eta\cos\theta) \tag{4.2}$$

Where from figure 4.2 θ is the angle of incidence, ϕ the rotation angle, e is the tilt angle between the surface of the birefringent plate and its optical axis and η is the polar angle of the refracted ray and the optic axis. η can also be defined from other easier to measure angles such that:

$$\cos\eta = \cos\phi\cos\theta\cos e + \sin\theta\sin e \tag{4.3}$$

Defining the equation for the retardation is outside of the scope of this thesis and a good approximation can be found in Principles of Optics by M. Borne and E. Wolf such that:

$$\delta = \frac{2\pi(n_e - n_o)d\sin^2\eta}{\lambda\sin\theta} \tag{4.4}$$

Where $(n_e - n_o)$ is the difference between the extraordinary and ordinary refractive index, d is the thickness of the optic and λ is the wavelength.

The $1/\lambda$ dependence of the retardation is what makes the birefringent filter introduce wavelength dependant losses. In addition to this, although the θ angle is generally fixed at Brewster's angle, η which is dependent on the rotation angle ϕ also affects the retardation. As such by rotating the birefringent filter around the axis normal to the surface the wavelength dependent retardation can be tuned which allows for selective wavelength losses.

To calculate the wavelength dependent transmission and using equation 4.2 and equation 4.4 we can combine the Jones matrix from equation 4.1 such that:

$$M = \begin{pmatrix} \cos^2\alpha + \sin^2\alpha\exp(-i\delta) & q\sin\alpha\cos\alpha[1-\exp(-i\delta)] \\ q\sin\alpha\cos\alpha[1-\exp(-i\delta)] & q^2[\sin^2\alpha + \cos^2\alpha\exp(-i\delta)] \end{pmatrix} \tag{4.5}$$

Further simplifications of the theory can be made by choosing components where for example the tilt angle e between the surface and optic axis is 0° or where α is set to 45°. For completeness sake we will not do either simplification in this theory section. However in the setup presented in the next section, the birefringent filter chosen has $e = 0^{\circ}$.

For a linear cavity which elements are a laser crystal and a quartz BRF the round-trip Jones matrix is $M_t = Q'Q'MM$. Q' is the Jones matrix that describes the polarisation dependent losses at the laser crystal such that:

$$Q' = \begin{pmatrix} 1 & 0 \\ 0 & q' \end{pmatrix} \tag{4.6}$$

For an eigenmode within the cavity it must fulfil the condition :

$$M_t E = tE \tag{4.7}$$

In this equation t is the eigenvalue of the eigenmode and usually a complex number. In general, eigenequation 4.7 produces two solution for t which for a Fabry-Perot cavity the larger of the two values of $|t|$ is determined to be the effective single-pass transmittance T of the filter.

4.1.2 Tuning with a BRF and modelling

From Waritanant and Major [82, 86] the BRF can be used as a tool to tune a cavity to a desired emission peak. This is because the wavelength-dependent losses of a BRF can be used to balance the losses between two emission wavelengths, enabling one to have a lower lasing threshold than the other. By introducing differential losses proportional to the ratio of their emission cross-sections, wavelengths with lower emission cross-sections can be made to lase preferentially over those with higher cross-sections following equation:

$$\frac{T_{\lambda_1} - \ln(R)}{\sigma_{\lambda_1}\eta_{\lambda_1}} > \frac{T_{\lambda_2} - \ln(R)}{\sigma_{\lambda_2}\eta_{\lambda_2}} \tag{4.8}$$

With in our case λ_1 being 1079 nm and λ_2 being 1083 nm. In the equation T is the round-trip intracavity loss, R the reflectivity at the output-coupler, η the quantum efficiency and σ the emission cross-section.

To help design the optimal cavity a program was developed that used equations 4.7 and 4.5 to calculate the transmission of a quartz BRF plate in a Nd:YAP laser cavity depending on the wavelength, the rotation angle, the angle of the optical axis to the surface and the thickness of the component. The refractive index of Nd:YAP was taken to be 1.925 [71] as specified by the distributor used. By comparing the resulting transmission of a theoretical BRF at 1079 nm and 1083 nm the thickness and rotation angle required to meet the condition described by equation 4.8 can be determined. Due to availability in the lab the BRF thickness explored were of 2,4 and 6 mm with all of them having an angle e of 0°.

Figure 4.3 shows the transmission at 1083 nm as a function of the rotation angle ϕ of 3 different BRF thicknesses (2,4 and 6 mm) calculated using the program. It is interesting to note that due to equation 4.4 for the retardation within the BRF, every wavelength for which the retardation is a full wave ($\delta = 2\pi m$, m an integer multiple of a full wave) will suffer no loss and will therefore experience a peak of transmission. From this graph the optimum rotation angle depending on the thickness can be found such that the transmission is at its highest but also that the slope around that point is

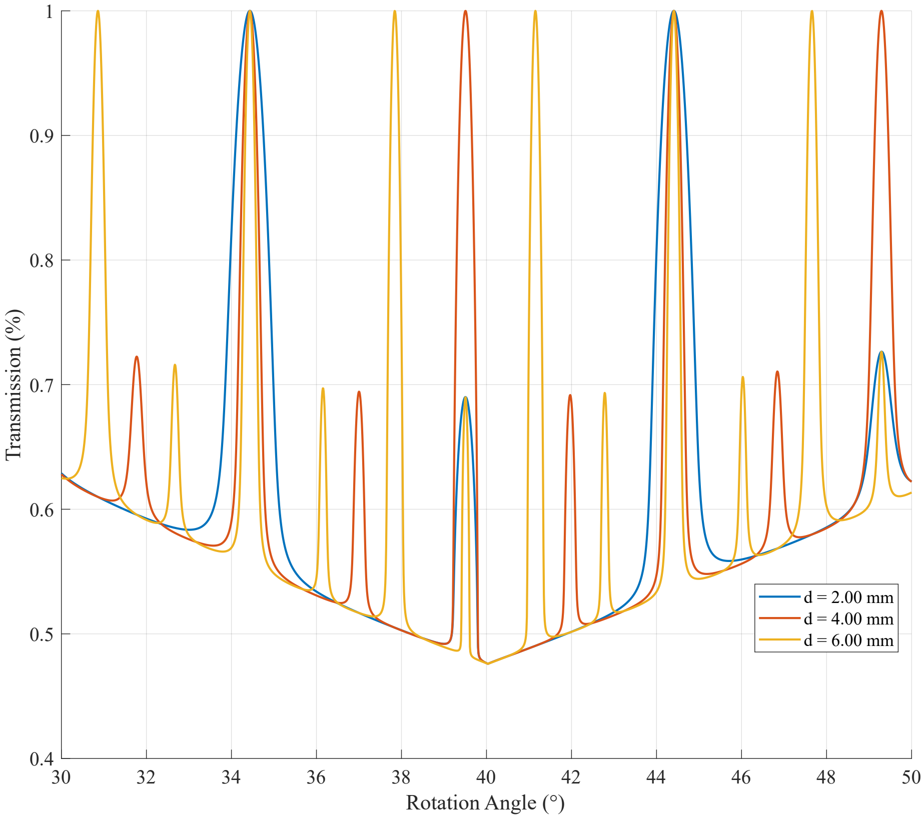

Figure 4.3: Graph of the transmission at 1083 nm as a function of the rotation angle ϕ of a 2,4 and 6 mm BRF.

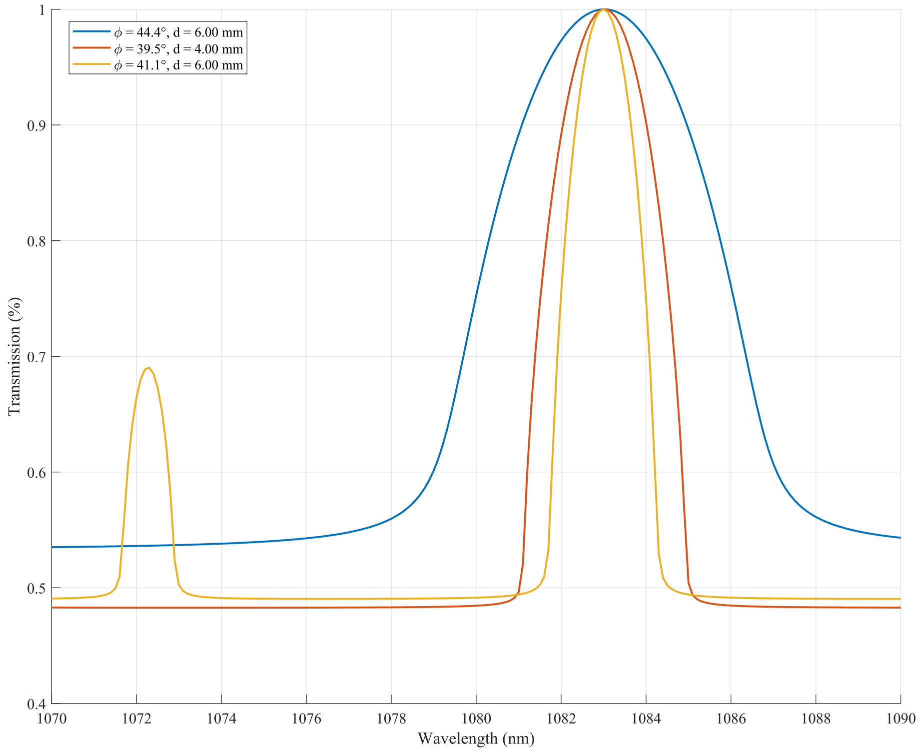

Figure 4.4: Graph of the transmission at optimal rotational angles depending on the BRF thickness as a function of wavelength.

the steepest and produces the largest drop in transmission. This ensures the narrowest effective linewidth and strongest rejection of other emission wavelengths (such as 1079 nm). This yields an angle of 44.41° for the 2 mm BRF, 39.51° for the 4 mm and 41.15° for 6 mm which are used to compare the transmission curves of these optimal angles in function of the wavelength to find the thickness that yields the best suppression of the 1079 nm emission wavelength.

From Figure 4.4, it is evident that the 6 mm thickness provides the narrowest transmission linewidth, and thus the most effective suppression of nearby emission wavelengths. This was later confirmed experimentally, as the 6 mm birefringent filter (BRF) was the only thickness that enabled wavelength tuning within the Nd:YAP laser cavity, as shown in Figure 4.11. It also supported stable Q-switched operation of the cavity.

To summarise, to ensure the greatest difference in transmission between 1079 nm and 1083 nm a BRF with a thickness of 6 mm should be used. Having selected the key component for tuning the Nd:YAP cavity, the following section will elaborate on the remaining components.

4.2 Cavity design for the 1083 nm Q-switched Nd:YAP laser

The considerations and requirements for the laser cavity, other than wavelength, have not changed compared to those described in section 3.1. However, due to availability of new equipment to the laboratory the design of the cavity will be slightly different. The biggest change is the more powerful pump diode laser, the characteristics of which shall be presented in a later section, which allows the laser to be pumped by a single source. The final setup which shall be explored within this section is shown in figure 4.5.

4.2.1 Nd:YAP crystal characteristics

The advantages of using Nd:YAP as the lasing crystal having been already explored in section 3.1.1 this section will endeavour to examine the advantages Nd:YAP provides for BRF tuning and the characteristics of the crystal obtained.

From the discussion of the theory behind tuning with a BRF it is evident that the polarisation of the light interacting with a BRF has a sizeable impact on the functionality of the optic. Due to the anisotropic nature of Nd:YAP its emission is naturally linearly polarised and this natural anisotropy swamps any induced anisotropy. Therefore by carefully choosing the orientation of the BRF and that of the Nd:YAP crystal the polarisation selectivity of the gain in the Nd:YAP will enhance the wavelength selectivity of the BRF.

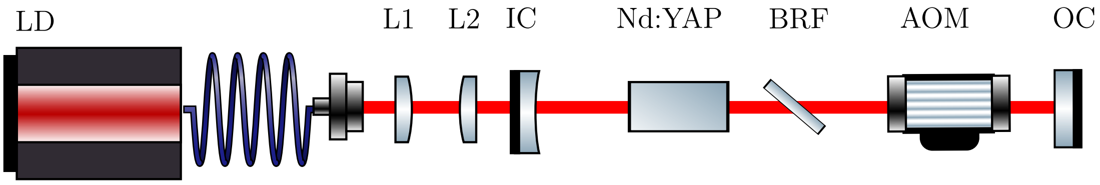

Figure 4.5: Diagram of the 1083 nm Q-switched Nd:YAP laser with LD being the pump laser diode, L1 and L2 conditioning optics and IC and OC input and output couplers. BRF is the birefringent filter and AOM the acousto-optic modulator.

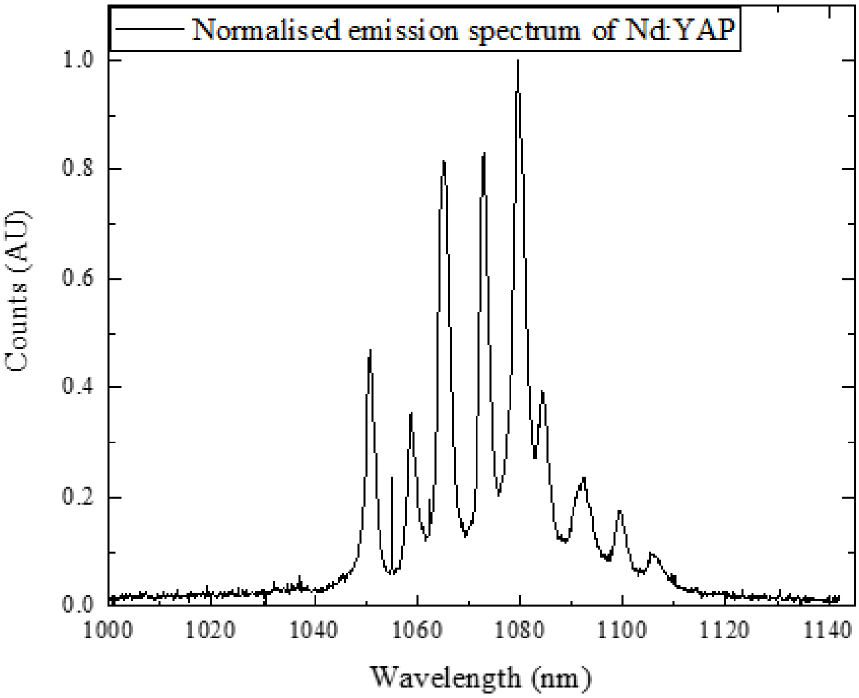

Figure 4.6: Graph of the normalised spectrum between 1000 nm and 1140 nm of the Nd:YAP crystal used for the 1083 nm Q-switched setup when oriented at the maximum 1083 nm emission.

Because of this and the arguments presented in section 4.1 a spherical rod of b-cut Nd:YAP was chosen which has a 0.9 at.% doping. The choice of a b-cut rod as specified in [81] yields a polarised output with the highest measured intensity when pumped along the a-axis at 1083 nm. The emission spectrum of the crystal was measured to ensure the correct orientation. This was achieved by pumping the crystal using the afore mentioned pump tuned to 802 nm to target the peak of a b-cut Nd:YAP absorption as specified by the provider of the crystal Crytur [87]. The emission was then passed through a 1000 nm long-pass filter and then focused into the fibre input of an Ocean Optic HR4000 spectrometer connected by USB to a computer to visualise the measured spectrum.

The spectrum of the crystal was measured for several orientations of the crystal which was rotated by hand. The spectrum shown in figure 4.6 is the one where the orientation of the crystal achieved the highest emission of 1083 nm. It is assumed that this orientation corresponds therefore to when the excitation is parallel to the a-axis. This spectrum has a strong 1079 nm peak as with all Nd:YAP orientation and a 1083 nm peak that is 40% the intensity of the 1079 nm peak. The sharp peaks seen at 1055 nm and 1064 nm are due to an equipment error and were observed across all measurements and likely arise from malfunctioning pixels within the detector.

4.2.2 Mode size

Due to the change in pump source the conditioning optics had to be rethought. The new diode laser has a 400 µm diameter core output fibre with a numerical aperture (NA) of 0.22. To achieve the required 300 µm mode radius for the pump beam in the Nd:YAP setup, spherical plano-convex lenses were selected for collimation and focusing. The collimating lens chosen has a focal length of 38 mm, while the focusing lens has a focal length of 100 mm. This yielded a measured beam radius size at focus of 333 µm with a measured Rayleigh range of 8 mm. The cavity was modelled in ReZonator and from the available mirrors a curved input mirror with a radius of curvature of 1000 mm was chosen with high reflectivity at 1080 nm and high transmission at the pump wavelength of 800 nm. The output coupler was a plane mirror with a reflectivity of 90% at 1080 nm. The output coupler will be more closely analysed later in the Chapter. Using a 13 mm in length and 3 mm diameter spherical rod of b-cut Nd:YAP with 0.9at% doping as the laser crystal the total cavity length was of approximately 200 mm with the majority of this length being due to the need to fit the BRF and the AOM. This gives a mode size radius at the focus of the pump for the 1079 nm wavelength of 330 um which matches the beam radius size at focus of the pump.

4.2.3 Cavity description

The setup for the laser can be found in figure 4.5. From left to right, which is also the beam path, the first component is the pump for the setup which is a DILAS 808 nm diode laser driven by a LIMO Laser Diode Driver 50 and cooled by a TC-48-20 thermoelectric cooler controlled through a LabVIEW software. This allowed for precise (<0.1°) temperature control of the diode laser. This diode laser is output through a 400 µm core fibre. At the output of the fibre are the collimating (f=38 mm) and the focusing (f = 100 mm) lenses which focused the beam into the cavity. The 200 mm long cavity is formed of first the input coupler (ROC = 1000 mm), then the Nd:YAP crystal, the BRF, the AOM and finally the plane output coupler. The laser crystal was chosen to be a 3×13 mm spherical rod of b-cut Nd:YAP with 0.9 at.% doping with the ends AR coated for 1079 nm and 808 nm. The crystal is wrapped with indium foil and put into a water cooled copper block with the water temperature set to 16°C through a cooling loop. The BRF is a 25 mm diameter and 6 mm thick quartz plate set in a kinematic mount allowing for a $-40°$ to 40° range rotation around its normal axis. The AOM is a Neos 33027-25-3BR used to achieve a Q-switch operation of the laser cavity. The AOM is driven by a IntraAction GE Series High Power Acousto-Optic Modulator Driver which was triggered by a Tektronix AFG3022C function generator. The function generator was timed by using the output trigger from the diode laser driver to optimally synchronise the pump diode laser and the AOM.

4.3 Nd:YAP laser setup characterisation and performance

Before launching into the results of Q-switched operation, the laser's performance in other modes of operation will first be examined. This preliminary analysis provides insight into the underlying behaviour of the laser system and informs the selection of parameters for optimal Q-switched performance. In particular, we begin by characterizing the pump laser and assessing how its properties influence the overall operation of the laser cavity.

4.3.1 Diode laser characterisation and considerations

The pump laser diode was run at 802 nm to target the peak of Nd:YAP absorption and was run mostly in a quasi-continuous wave (q-CW) mode and more rarely in continuous wave (CW) mode. In q-CW the diode laser was run with a pulse on-time of 1 ms and pulse frequency of 20 Hz equivalent to a period of 50 ms.

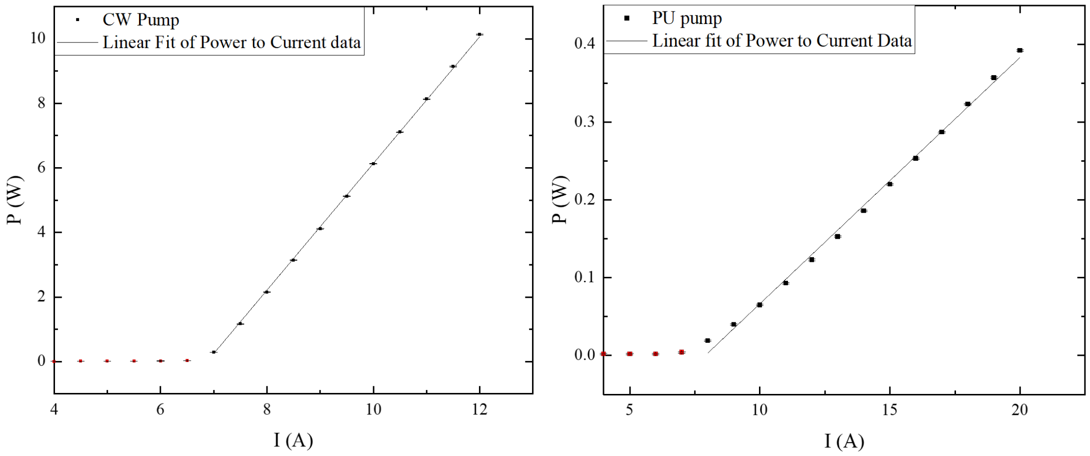

Figure 4.7: Graph of the current used on the pump diode laser to average power measured for both CW shown on the left and pulsed operation (PU) of the pump diode on the right, corresponding to q-CW operation of the Nd:YAP laser.

Figure 4.7 shows the measured average power (Watts) in function of the driver current (Amps) of the pump diode laser for both the CW and q-CW mode . The threshold of the diode laser in both modes is measured when driving the diode laser with 7 A. Fitting a linear fit to the data, masking any points before the threshold is reached, gives a way to convert current to power. For the CW mode this gives $P = -13.5 + 1.9 \times I$ and for the q-CW mode $P = -0.25 + 0.03 \times I$. Using this and measuring the power after passing through the Nd:YAP crystal, the absorption of the Nd:YAP crystal can be determined to be an average 97 % at the pump wavelength. It's linewidth using the Ocean Optic HR4000 spectrometer with a spectral resolution of approximately 0.2 nm was measured to be of 1 nm. Although threshold is often represented as a sharp cut-on, in reality spontaneous emission and competing oscillating modes lead to measurable output before fully linear behaviour is reached, resulting in the slight ramp observed.

From the absorption the thermal lens in the Nd:YAP crystal can be estimated which, as detailed in the previous chapter, can greatly affect the stability of the cavity. Using the equation for thermal lensing 1.3, shown underneath as a reminder, and keeping in mind the thermal conductivity (K) of Nd:YAP is 11 W/mK and the rate of change of refractive index with temperature ($\frac{dn}{dt}$) is $9.7 \times 10^{-6} K^{-1}$ we can calculate the induced thermal lens for different average pump powers [21]:

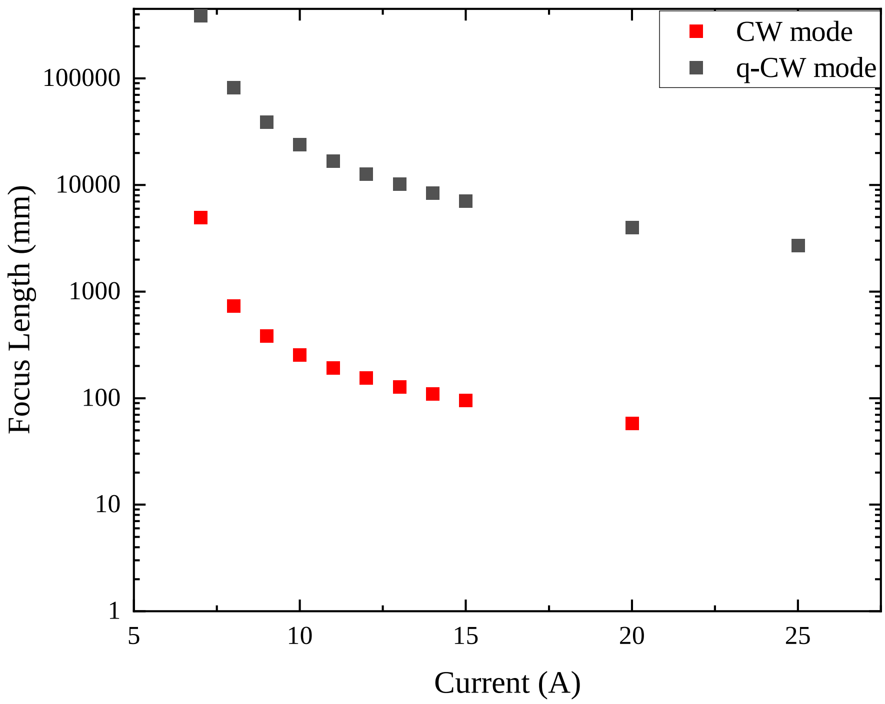

Figure 4.8: Graph of the thermal lens focal length induced within the Nd:YAP crystal by the pump laser in CW (in red) and q-CW mode (in black).

$$f = \frac{K\pi\omega_p^2}{\eta P_p \frac{dn}{dt}} \tag{4.9}$$

From the ReZonator model the cavity was found to be stable until a thermal lens of 150 mm was induced within the Nd:YAP crystal. From figure 4.8 it is evident that to ensure that the cavity stays stable and that the effect of thermal lensing is manageable the q-CW mode allows for more energetic pulses without making the cavity unstable. Therefore, all the measurements described will be performed using the q-CW mode unless specifically mentioned.

4.3.2 1079 nm Nd:YAP results

To ensure the cavity was optimal, it was first aligned using the 1079 nm emission wavelength with only the crystal and the input and output couplers inside the cavity.

The output coupler was chosen to have a partial reflectivity of 90% at 1080 nm. From this a threshold at a measured 20 mW average incident power was achieved (pump laser driven by 8.1 A). Because the pump diode laser is operating near its threshold and at relatively low power, it is more accurate to determine the threshold by direct measurement of the average power rather than using the equation relating drive current to average power. A measurement of the average incident power to output power was performed to calculate the slope efficiency of the laser.

From the results shown in figure 4.9 and the resulting linear fit of the data, the slope efficiency of the laser is calculated to be 35 ± 0.5 %. The points that were chosen to be masked on the plot for the fitting bear mentioning. The more easily explained masked points are the ones situated before the laser threshold which would warp the linear

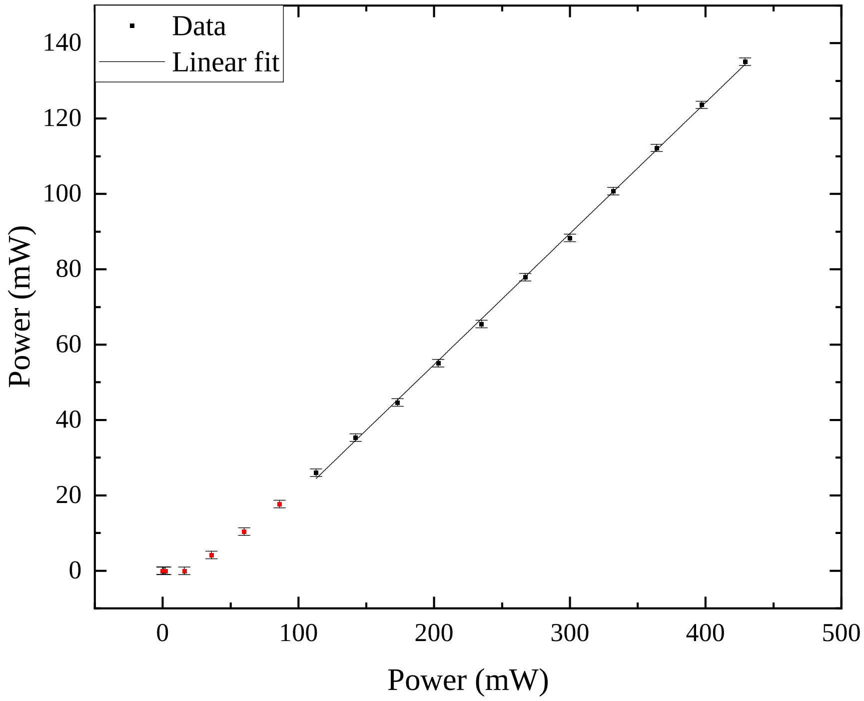

Figure 4.9: Graph of the average output power of the Nd:YAP laser operating at 1079 nm in function of the average incident pump power. This data is fitted to a linear curve to find a slope efficiency found to be 35%

fit due to no measurable output of the laser. The other ones that are more complex are those after the threshold is reached but before the laser operation reaches a linear behaviour and which form a curve near the threshold. This curve can be due to several reasons such as the laser operating at different modes before reaching a steady state but with lower slope efficiency. It could also be due to effects related to the diode laser not reaching its own steady state which can be seen in figure 4.7 or even an effect of the thermal lensing affecting the slope around the threshold. These effects together or separately will have an effect on the slope efficiency and therefore the data points before a proper linear progression in the average output power to average incident power are masked.

To determine the round-trip losses within the cavity a Findlay-Clay analysis was performed. From the paper published by Findlay and Clay [88] in which the derivation is presented in more detail, this analysis is based on the threshold condition that the gain per pass balances exactly the internal and external losses such that:

$$R_1 R_2 exp(2l(g_{th} - \delta)) = 1 \tag{4.10}$$

Where R_1 and R_2 are the reflectivities of the cavity mirrors, l is the length of the rod, g_{th} the amplification coefficient at threshold and δ the total internal loss coefficient. Equation 4.10 can further be simplified when the input coupler is considered to have high reflectivity (>99.5%) as in our case to [21]:

$$-ln(R) = 2g_{th}l - \delta \tag{4.11}$$

Where R is the reflectivity of the output coupler. As $2g_{th}l$ is proportional to the incident on-time power at threshold fitting a line to a plot of $-ln(R)$ versus P_{th} will yield the round-trip resonator loss δ as the intercept of the line. Using available output couplers with quoted reflectivities R= 97%, 93%, 90% and 70% from the laboratory the threshold energy of the 1079 nm laser were measured. The reflectivity of each mirror at 1079 nm was also measured to ensure the accuracy of the results.

From figure 4.10 it can be seen that the loss coefficient was found to be of 0.3±0.3 %.

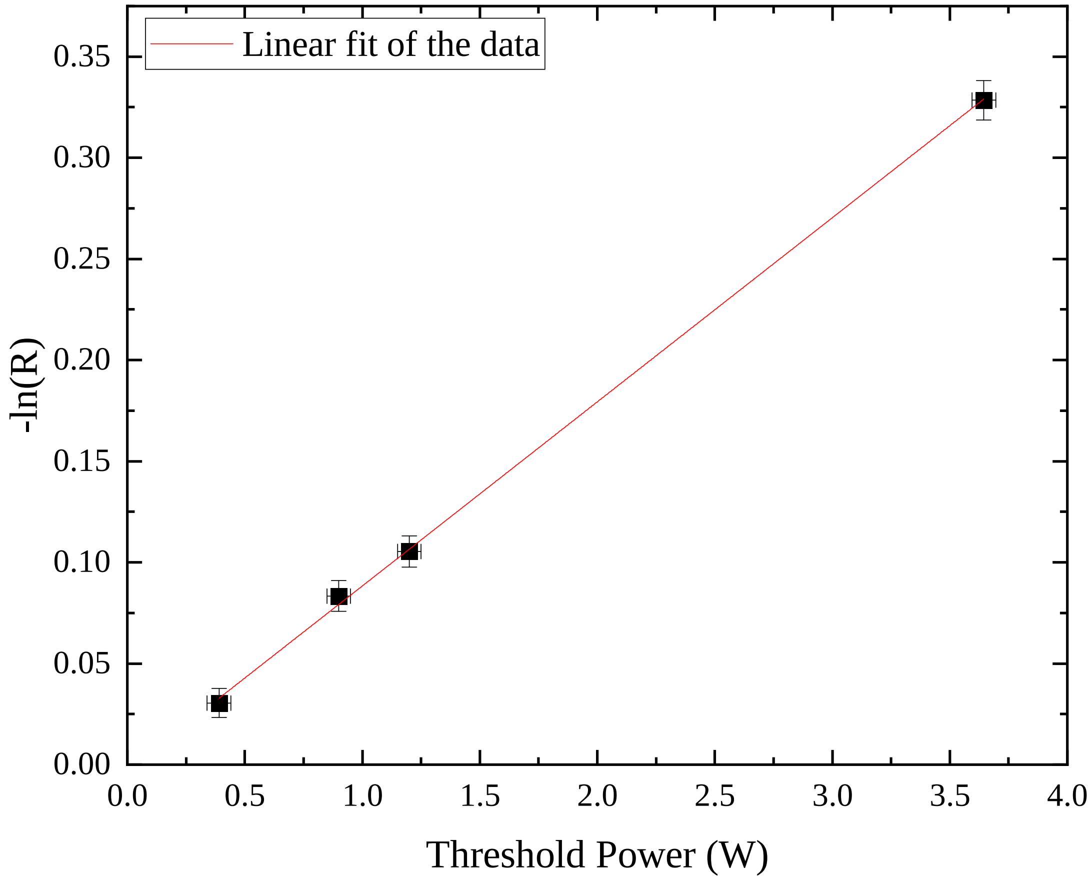

Figure 4.10: Graph of the negative natural log of the output coupler in function of the on-time threshold power. The data was fitted to a straight line and the intercept found to be 0.003 ± 0.003.

A more accurate measurement would likely include more reflectivities however due to the limited availability of output couplers the result was considered satisfactory.

4.3.3 Nd:YAP laser tuning

Before detailing the Q-switching of the cavity, the 6 mm BRF was introduced to measure the tuneability of the laser. This, as presented earlier, introduces wavelength dependent losses in the cavity by rotating the BRF around the axis normal to the surface of the plate. This allows for selectively tuning the laser to other emission wavelengths. As discussed in section 4.1, the BRF was introduced at Brewster's angle at the position shown in figure 4.5. The output spectrum of the laser was collected using the same method as employed earlier using the Ocean Optic HR4000 spectrometer.

By rotating the BRF, different laser emission wavelengths were found. Simultaneous emission of multiple wavelengths was also observed. However, since this is not the focus of the thesis, only the single emission wavelengths will be explored in detail. As shown in figure 4.11 peaks of laser emission were measured at 1064 nm, 1072 nm, 1079 nm and 1083 nm. This is in close agreement with the emission peaks measured in the fluorescence spectrum shown earlier in figure 4.6. The BRF angle at which the 1083 nm emission peak is measured was found to correspond closely to the theory with the BRF being rotated 38°. The difference can likely be attributed to the impact that every angle has on the retardation as shown in the theory and the difficulty in the laboratory to control accurately all of these parameters. Indeed, even just the Brewster angle

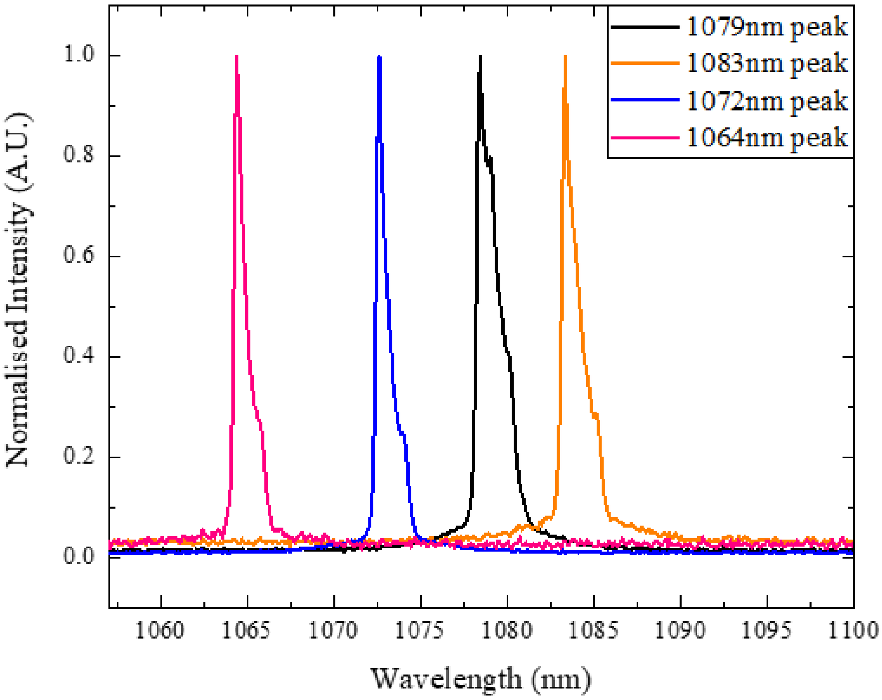

Figure 4.11: Graph of four different Nd:YAP laser emission wavelengths obtained using the 6 mm BRF normalised. In red an emission peak at 1064 nm is shown, in blue a peak at 1072 nm, in black at 1079 nm and finally in orange a peak at 1083 nm.

being slightly different has a strong impact on the loss spectrum and as such the in laboratory observations might not exactly match up with the theoretically calculated values. Additionally, the BRF was mounted in such a way that the rotation of the mount did not exactly correspond to rotation around the normal axis of the BRF, which could also be a source of the disparity.

One thing to note is the presence of shoulders on the side of each peak which is likely due to spatial hole burning or other modes of oscillation inside the cavity which, as described in chapter 3 and in more detail in [65], can be minimised by introducing an etalon in the cavity. Therefore, for the end setup a quartz 2 mm etalon which corresponds to a free spectral range or FSR of 74.7 GHz or 0.3 nm at 1080 nm was introduced in the cavity between the BRF and AOM to minimise the linewidth of the output. Further analysis on its impact will be reviewed later in this chapter.

4.4 Q-switch operation results of the Nd:YAP laser

As explained in section 3.1, to achieve the high peak powers required to reach the Raman threshold, Raman lasers pump sources are typically operated in a pulsed regime. In our setup, this was accomplished using a steady-state laser in Q-switched mode. The theory of which can be found in section 3.1.3. In our setup the Q-switching was achieved by introducing an acoustic-optic modulator (AOM). The AOM used in this setup was a Neos 33027-25-3BR which housed a water-cooled fused silica crystal at Brewster's angle with a centre frequency of 27.12 MHz and a 2 mm active aperture. This uses a transducer attached to the crystal to induce, through sound waves, a Bragg grating within the crystal. This spoils the quality of the cavity and inhibits oscillation within the cavity. This is reversed when a calculated or experimentally determined time, named trigger delay here, is reached to allow for a maximum in the population inversion within the crystal. This can be determined using the rate equation 3.1.3 for population inversion and the equation for the pump rate of: $R_p = \frac{P_{abs}}{h\nu_p V}$ [76] where R_p is the pump rate, P_{abs} is the absorbed pump on-time average power which in our case was of $25W$ approximately. $h\nu_p$ is the energy of the absorbed pump photon and V is the pumping volume which shall be assumed to be a cylinder here for simplicity. From this

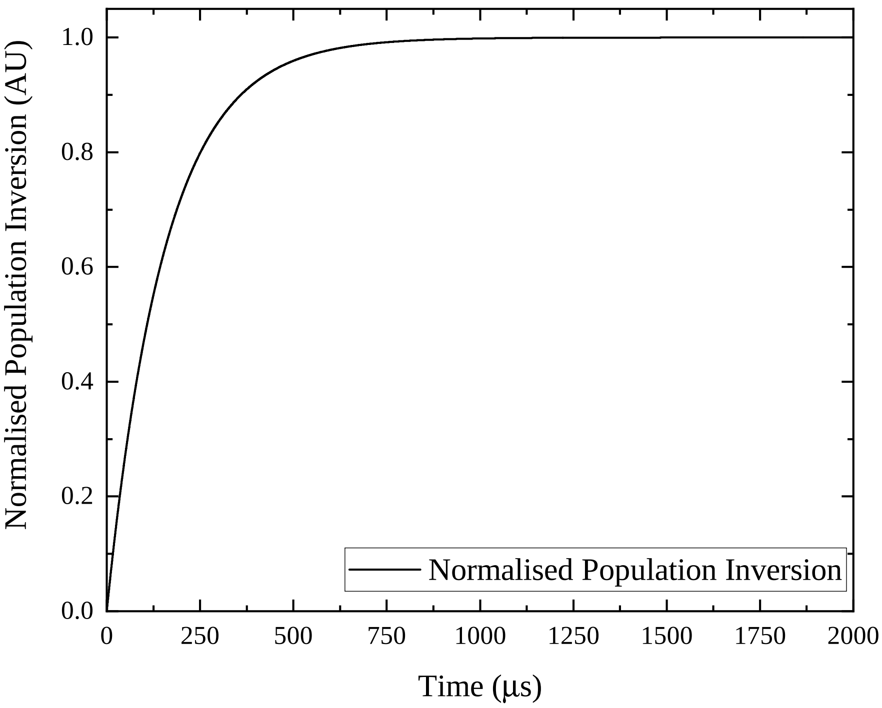

Figure 4.12: Graph of the evolution of the normalised population inversion within Nd:YAP crystal in terms of the pump on-time

and by rearranging equation 4.4 so that it describes the population inversion in terms of time: $N(t) = R_p\tau(1 - e^{-t/\tau})$ the evolution of the population inversion depending on the pump on-time can be determined. This describes the population inversion rising until it reaches a maximum as shown in figure 4.12.

From figure 4.12 we can estimate that a suitable trigger delay for the AOM would be around 600 µs. This allows the population inversion to reach its potential maximum thus maximising the potential peak power of the laser.

This result was used as a starting point to experimentally determine the optimal parameters for Q-switch operation. The parameters were then experimentally determined by measuring the output pulse with a photodetector linked to an oscilloscope. The different involved pulses in time can be visualised as shown in figure 4.13. As such, if lasing was achieved before the Q-switch window or if there were any laser emission after the window was closed it was evident that the parameters would need to be modified.

For the Q-switch setup the output coupler was reduced to 70% reflectivity initially for the reasons described in section 3.2. This was subsequently raised to 80% as, at the lower reflectivity, it was found that the tuneability of the cavity was impacted likely in relation to equation 4.8.

Experimentally it was found that a 604 µs delay and a Q-switch window of 410 ns were optimal and gave the highest output power. This is close to the theory and slightly different to the previous setup, likely due to different cable management and the difference in the setup in the laboratory.

From this, the output energy of the 1079 nm Q-switched laser was measured to be 580 µJ, with a pulse duration of 16.8 ns. These values were obtained for an average pump power of 350 mW with all the components inside the cavity. The threshold of this laser emission was found to be at 176 mW average pump power. This is enough to achieve the required pulse energy of 500 µJ detailed in the previous chapter 3. In addition, even larger pulse energies were measured at higher average pump powers showing a scalability of the cavity if required. Having confirmed the characteristics of

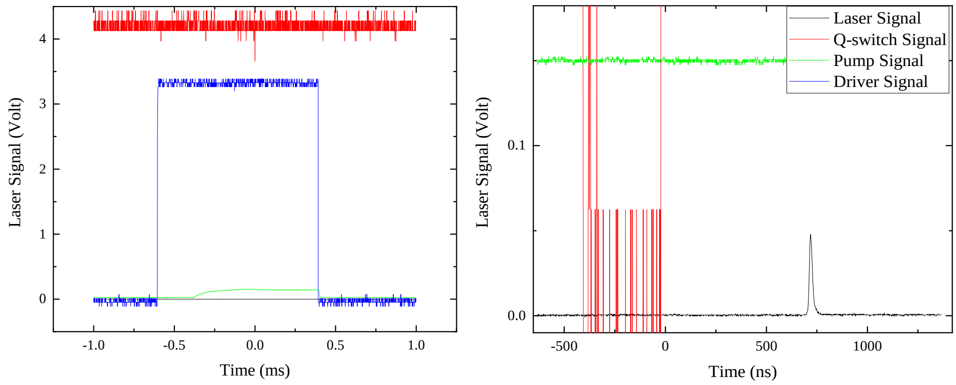

Figure 4.13: Oscilloscope traces of the pump laser trigger output signal in blue, the trigger signal send to the Q-switch driver by the function generator in red, the pump signal as measured by a photodetector in red and the Q-switch emitted laser measured by a photodetector in black. The oscilloscope voltage scale is retained as the signals are measured directly from different sources. The right-hand plot is a temporal and vertical zoom that allows the fast Q-switch trigger signal and the laser pulse to be resolved.

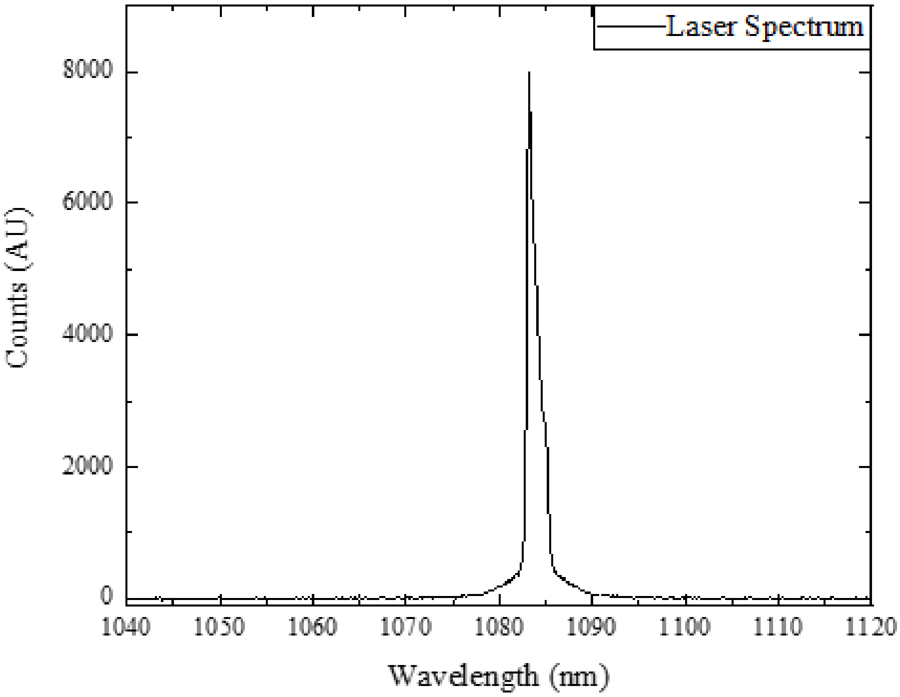

Figure 4.14: Spectrum of the Nd:YAP Q-switched laser emitting at 1083 nm

the 1079 nm Q-switched laser cavity, the tuning of the cavity using the inserted BRF was tested.

Whilst rotating the BRF to find the emission angle for 1083 nm emission, multiple other emission wavelengths were observed. Dual wavelength emission from the cavity was also found especially of 1072 nm and 1079 nm, which were frequently observed both simultaneously and individually. Although not the aim of the experiment, this is interesting to note as it matches the tuning that was observed in the [78] proving that a BRF based cavity is also a solution to achieving multi-wavelength tuneable cavities. It is also worth mentioning that in the Waritanant and Major paper [86] this potential for multi-wavelength emission cavity is discussed and the advantages of using a BRF are detailed, especially the ability to stack multiple BRF plates of various thickness to provide even more control over the wavelength dependent losses inside the cavity.

Rotating the BRF to around the same angle as before (∼38°), a Q-switched emission wavelength of 1083 nm was achieved, which to the author's knowledge is the first time such a wavelength from a Q-switched Nd:YAP laser has been reported. As shown in figure 4.14, the spectrum of the laser when pumped between 293 mW and 401 mW average pump power has a single peak of emission at 1083.2 nm with a linewidth of 1.7 nm. This is a wider linewidth than would have been ideal and was later reduced to 0.9 nm by introducing a 2 mm etalon within the cavity as mentioned earlier. This had no discernible effect on the pulse energy or pulse width. Although still larger than desired due to the Raman gain bandwidth at 1080 nm being 0.2 nm, this linewidth of the Q-switched laser emission which was comparable to that of the 1079 nm setup was considering sufficient for the proof-of-concept setup targeted.

The laser output had a pulse duration of 38 ns and a maximum pulse energy of 540 µJ. It was mainly operated at a stable 500 µJ pulse energy when pumped by 350 mW average pumper power. To ensure that the laser was of good quality, an M^2 measurement of the laser output was also performed. For this measurement, the laser output was focused down by a $f = 125\ mm$ lens and the beam profile was measured at the focus and in the far field with a Spiricon sp620U beam profiler. By doing this the divergence angle can be calculated and the M^2 of the beam as well such that: $\phi = M^2(\frac{\lambda}{\pi\omega})$ [21, 76]. Where ϕ is the beam divergence, λ the laser wavelength and ω the beam waist radius.

The 2D beam intensity profile of the laser was measured at multiple positions. A Gaussian profile was fitted to the x and y axis of the beam profile and the resultant σ_4 width of each position was determined. From this the radius in the x and y axis of the beam profile were plotted with respect to their position as shown in figure 4.15. A linear fit of the far field points was performed and the beam divergence angle for each axis was found. This enabled us, using the equation detailed earlier, to find the M^2 for both axes of the laser beam, which were found to be $M_x^2 = 1.18 \pm 0.01$ and $M_y^2 = 1.2 \pm 0.01$. This is considered good quality for the proof-of-concept setup desired.

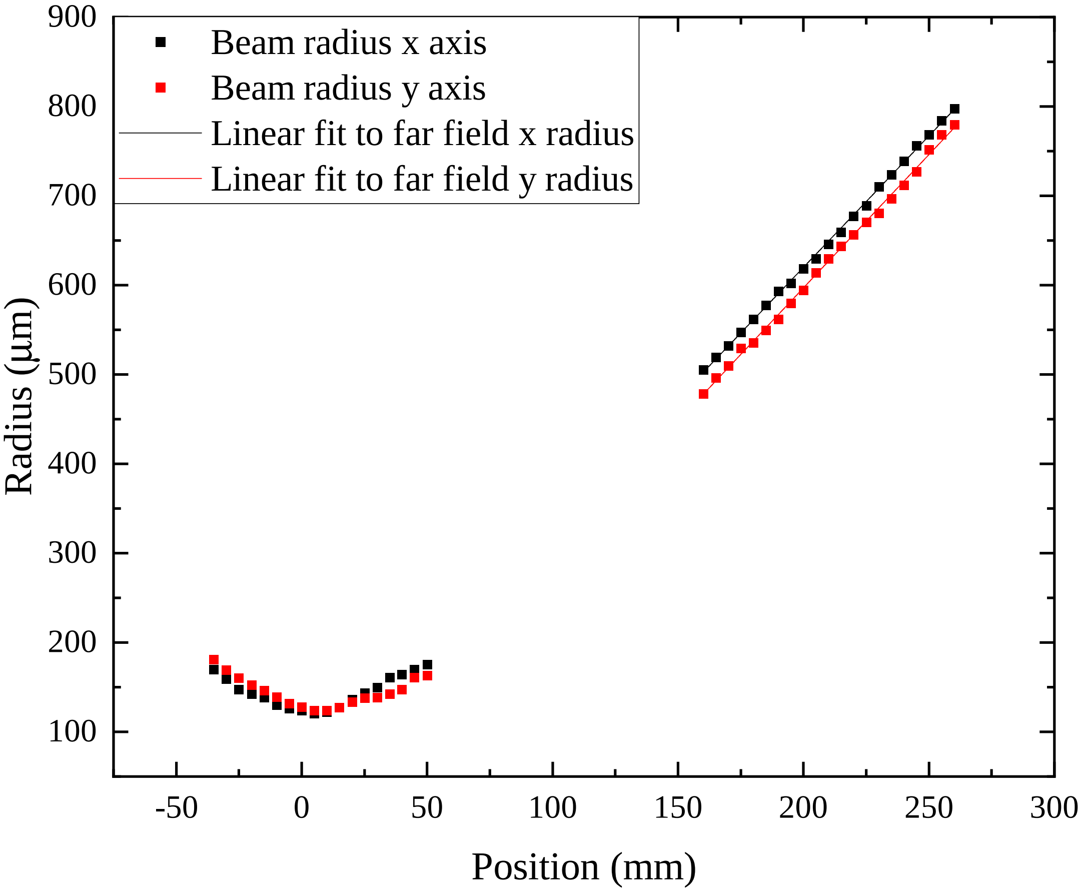

Figure 4.15: Graph of the evolution of the x and y radius of the focused 1083 nm Q-switched Nd:YAP laser at near and far field. The far field points are fitted with a linear fit to calculate the beam divergence angle and as such the M^2 of the laser.

4.5 Conclusion

In conclusion a 1083 nm Q-switch laser with 38 ns pulses with a pulse energy of 500 µJ was presented for the first time using a BRF as the tuning element in the cavity. This laser had a wavelength of 1083 nm and a linewidth of 0.9 nm. It was also of good beam quality with an M^2 average across its x and y axis of 1.19. These parameters are sufficient for this laser setup to be used as a pump for the proof-of-concept D-MOPA setup presented in Chapter 3. Further work could be performed to improve the linewidth by introducing further wavelength specific losses such as by exploring the use of multiple BRFs of different wavelengths. Using this method further studies could be performed to explore the multi-wavelength emission capability of the setup and the wide tuneability range of such a setup.

Chapter 5

Optimised D-MOPA

As discussed in Chapter 3 the initial proof-of-concept setup had several limitations. The limitations highlighted in Chapter 3 were specifically the timing jitter between the pump and the seed, the wavelength of the seed being on the edge of the gain range for an EDFA setup and the emission of parasitic 2^{nd} Stokes emission. To alleviate and attempt to remedy these limitations and optimise the setup further a combined method of modelling as explored in Chapter 2 and experimental work, presented in Chapter 4, was used. Using the insights acquired through modelling and the improvements in the pump laser, an improved setup was assembled. In this Chapter we will first be exploring the smaller improvements and their impacts such as changing the Raman crystal length, then the improved setup will be introduced and its characteristics detailed and finally the results acquired from this new setup and their significance will be presented.

5.1 Initial improvements of the proof-of-concept setup

5.1.1 Diamond crystal length optimisation

One early improvement that was made to the proof-of-concept setup shown in figure 3.5 was to switch out the 4 mm diamond for a 7 mm diamond instead. The 7 mm length was the longest available at the required specification to purchase from our supplier Element 6 at the time of writing this thesis. This new sample has the same quoted coating characteristics as the previous one having been coated by the same company.

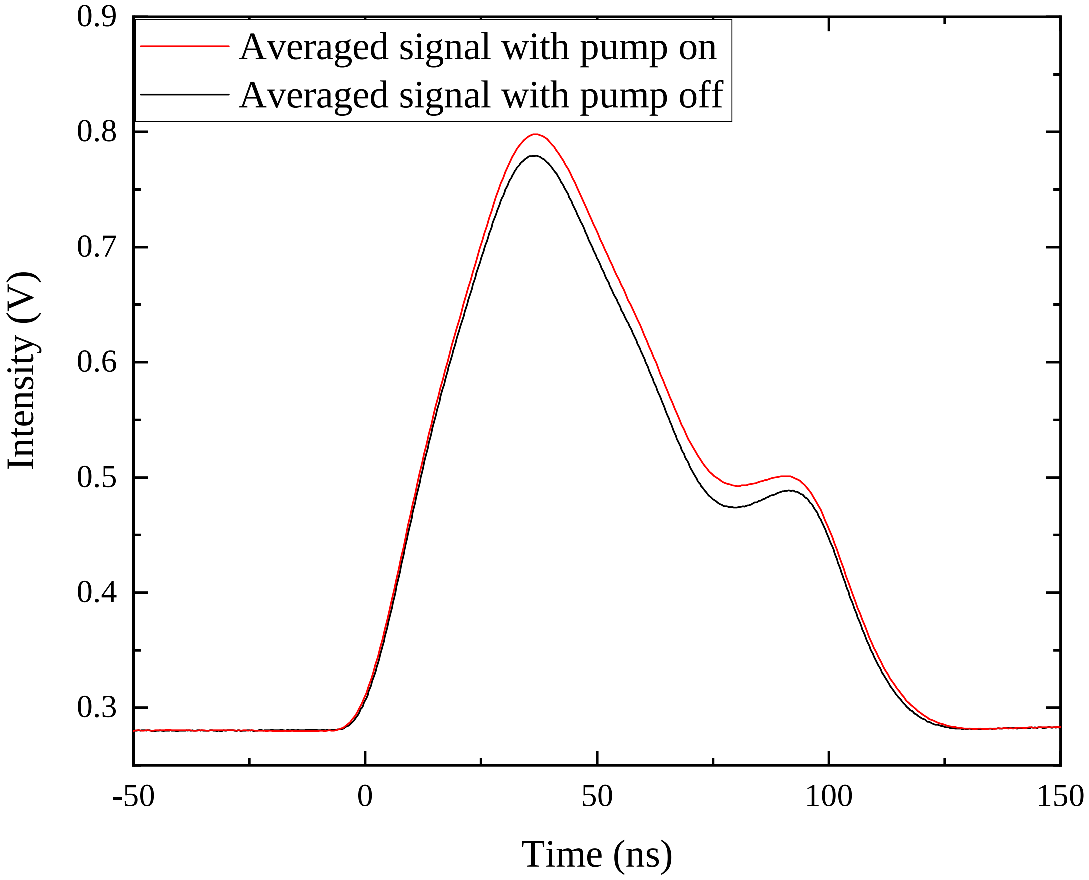

Figure 5.1: Graph of the averaged temporal response of the photodiode with pump on and off situated after the D-MOPA cavity with a diamond crystal length of 7 mm. In red is the signal with the Nd:YAP pump laser on with a measured pump pulse energy of 100 µJ and in black the signal without any pump laser. The ratio of the two signal areas is of 1.05.

From the equations presented in section 2.1 and the modelling of the amplification factor in function of the sample size from figure 2.6, this change should increase the potential amplification of the setup by a factor of $\sim \times 1.8$. Of note from the results shown in figure 2.6, longer crystals would theoretically improve this increase further however are not easily acquired. As multiple crystal lengths were taken into consideration when designing the cavity, no change is needed to accommodate the size of the new diamond in the cavity.

The average amplification factor of this new setup as shown in figure 5.1 was measured to be $\times 1.05$ with a 100 µJ pump pulse energy. Although a slightly smaller amplification factor than that discussed in section 3.8.2, this was achieved with half the amount of pump pulse energy and much closer to the threshold of the 1^{st} Stokes field. The pump pulse energy was chosen to stay under the calculated LIDT of the diamond as shown in figure 3.4.

5.1.2 Optimisation of the EDFA setup

From graph 2.5 located in the the modelling section it was clear that the timing delay of the seed laser to the pump laser was key in maximising the amplification factor. Additionally the shape of the seed laser was also shown to have an effect on the ease in optimising the delay. In the modelling, both a Gaussian and top-hat pulse shape were tested with the top-hat shape allowing for much greater margin of error of the delay compared to the Gaussian. To emulate this within the lab an electro-optic modulator (EOM) was introduced between the DFB (the seed of the EDFA) and the EDFA. EOMs based on Pockels effect [21, 89] functions in much the same way as an AOM but instead of using acoustic waves to induce a diffraction grating within a material an electrical field is used to modulate the refractive index in a non-linear crystal. Compared to modulating the drive current which was limited to a minimum pulse width of 100 ns and induced a double Gaussian peaked shape to the DFB pulse the EOM allows better control over the timing and shape of the DFB pulses. This would allow running the DFB in a continuous wave mode while carving out the desired pulses with the EOM.

The EOM that was used in this setup was a Lucent 2623NA which uses Lithium Niobate as the active crystal and has a quoted bandwidth of 10 GHz and an extinction ratio of 27 dB. It was driven by the Tektronix AFG3022C function generator which also triggers the AOM driver. This allowed for DFB pulse widths down to 10 ns and by driving directly from the function generator the timing between the Nd:YAP Q-switched laser and the EDFA pulses had much lower jitter down to the order of 10 ns. It also changed the pulse shape from the double peaks to a top-hat shape which was made it much easier to find the amplification factor.

The amplification factor was measured the same way as described in section 3.8.2 with the average of 64 traces for both the non-amplified and amplified signal measured.

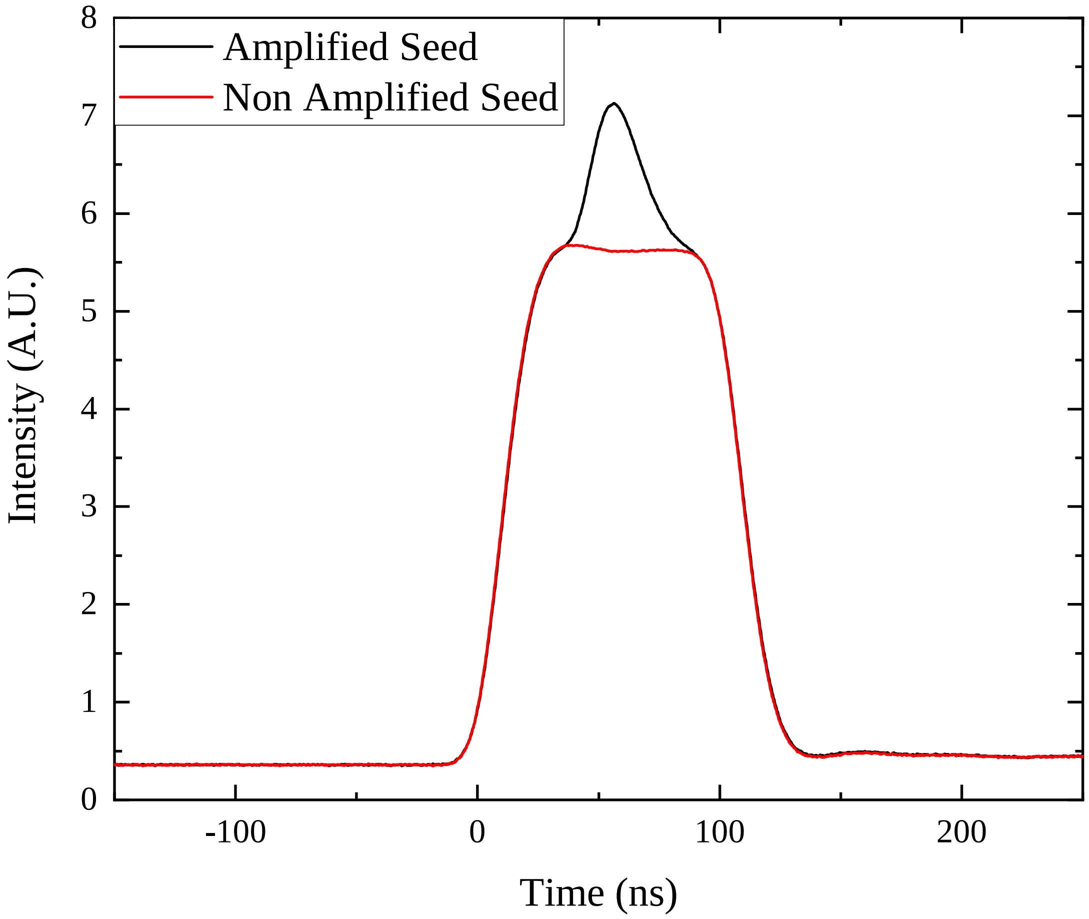

Figure 5.2: Graph of the averaged temporal response of the photodiode with pump on and off situated after the D-MOPA cavity with an EOM to generate the DFB pulses.

As shown in figure 5.2 the amplified output with the EOM is a lot more distinct compared to the amplified output without. This allowed for better alignment and more control over the system. This gave us an average amplification factor of ×1.07 with a pump pulse energy of only 100 µJ which is an improvement to the previously reported ×1.05.

To ensure that what was measured is indeed amplification of the seed and not just a 2^{nd} Stokes parasitic output on top of the seed curve, we can use the dependence of the amplification on the wavelength as was shown in section 3.8.2. With the Nd:YAP pump laser operating at 1079 nm, the corresponding 2^{nd} Stokes wavelength is here theoretically expected to be approximately 1515 nm. By changing the temperature

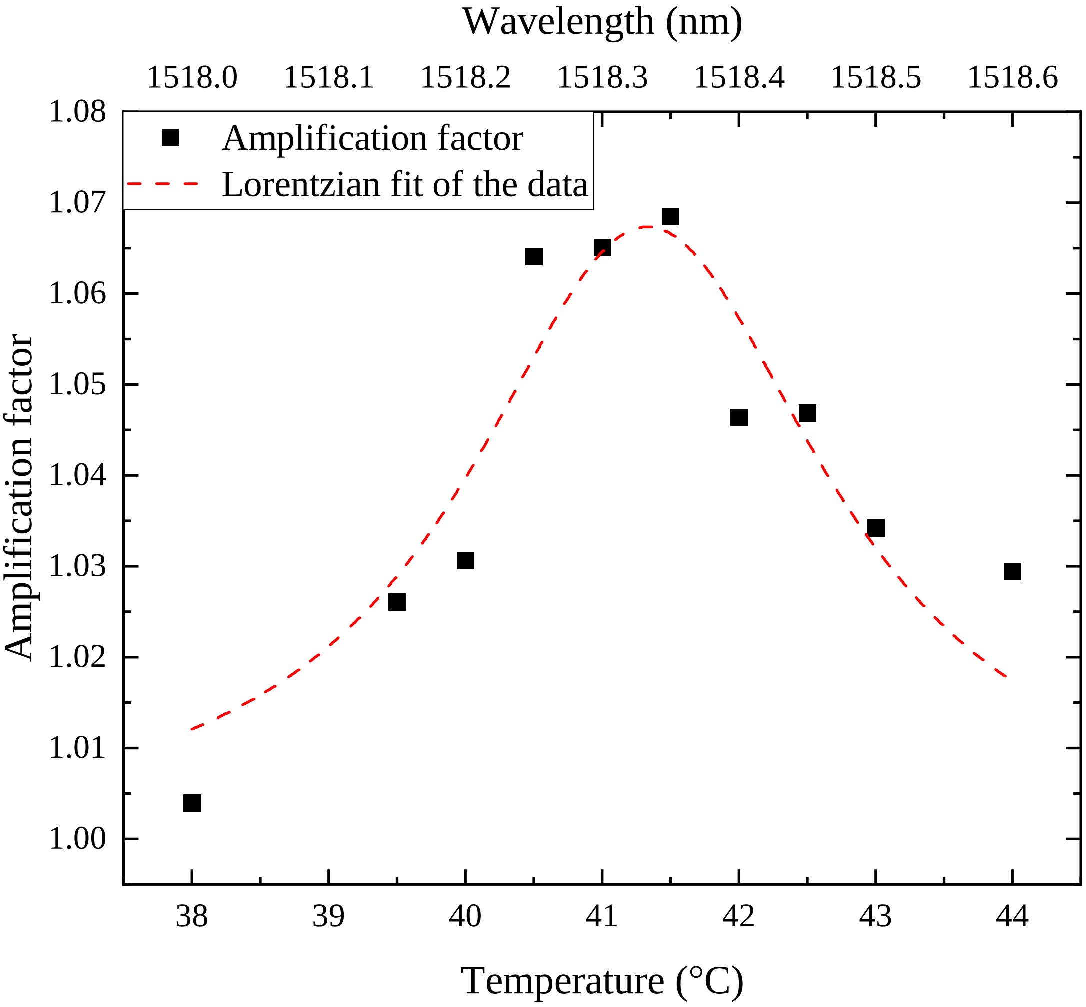

Figure 5.3: Graph of the measured amplification in function of the temperature and therefore wavelength of the DFB seed laser with a 7 mm diamond crystal and an EOM to shape the seed pulses. The data is fitted with a Lorentzian fit.

of the DFB, we can change its wavelength at a rate of 0.1 $nm/°C$. At a temperature where no amplification is expected due to the mismatch between the seed and 2^{nd} Stokes wavelength the ratio of the areas should fall to 1. The full width half maximum of this effect can be expected to be around 0.4 nm or 4°C which is the reported Raman gain bandwidth in diamond of 2 cm^{-1} at 1518 nm. If instead it is parasitic emission of 2^{nd} Stokes, we expect little difference in the amplification factor when changing the wavelength of the seed.

From figure 5.3 we can see that the amplification factor does fall to 1 outside of a wavelength range as expected. Additionally when fit with a Lorentzian curve which is the expected curve of the Raman gain bandwidth, its full width half maximum is calculated to be of 0.3±0.01 nm which is in accordance with the Raman gain bandwidth. The uncertainty is derived from the fitting error of the Lorentzian fit.

Having implemented the improvements that could be done without changing the setup too much, the second set of changes was to modify the setup further to implement the change in DFB wavelength to one closer to the EDFA gain range. The optimised setup will first be presented and the changes highlighted. Then the new DFB will be characterised and finally the results taken with the optimised setup and their significance will be discussed.

5.2 Optimised D-MOPA setup

Figure 5.4 shows the optimised setup with the pump laser being replaced by the 1083 nm Nd:YAP Q-switched laser presented in Chapter 4 and the EOM being added to the seed laser setup. This setup is designed to use the 1083 nm wavelength of the Nd:YAP Q-switched laser and therefore the DFB has been changed to a 1521 nm model of the same type as the 1515 nm one in the previous setup. Another addition is that of a N-BK7 right angled prism to separate the different wavelengths in space as the laboratory lost access to the previously mentioned monochromator. The path length after the prism was chosen to be 20 cm to ensure 1 cm between the 1265 nm and 1520

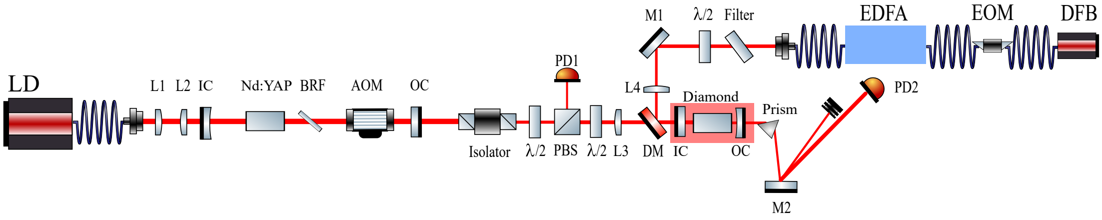

Figure 5.4: Diagram of the optimised proof-of-concept D-MOPA setup. On the left is the 1083 nm Nd:YAP pump laser cavity, in blue the EDFA seed laser and in red the diamond amplifier cavity. In the diagram L stands for lens, IC and OC stands for input and output coupler, DM is for dichroic mirror and M mirror. AOM is acoustic-optic modulator, EOM is the eletro-optic modulator, BRF is birefringent filter and PBS polarising beam splitter. Finally LD is laser diode, PD is photodiode and $\lambda/2$ signifies a half-waveplate.

nm according to modelling performed within Zemax.

5.2.1 1083 nm Nd:YAP laser focus

Changing the pump laser of the D-MOPA necessitated a reassessment of the optics used to guide and focus the beam into the diamond Raman cavity, in order to maintain a focal spot size as close as possible to the original, which had a measured radius of 72 µm. This was achieved by modelling in ReZonator the beam path taking into account the M^2 measured in section 4.4 and the output radius measured to be of 370 µm. The resulting modelled beam path is shown in figure 5.5 with 2 1000 mm focal length lenses to collimate and keep the beam under the 25 mm diameter radius for the optics and the 100 mm focal length lens to focus the beam into the diamond Raman cavity. The theoretical radius of the focus when placed about a third of the length of the diamond

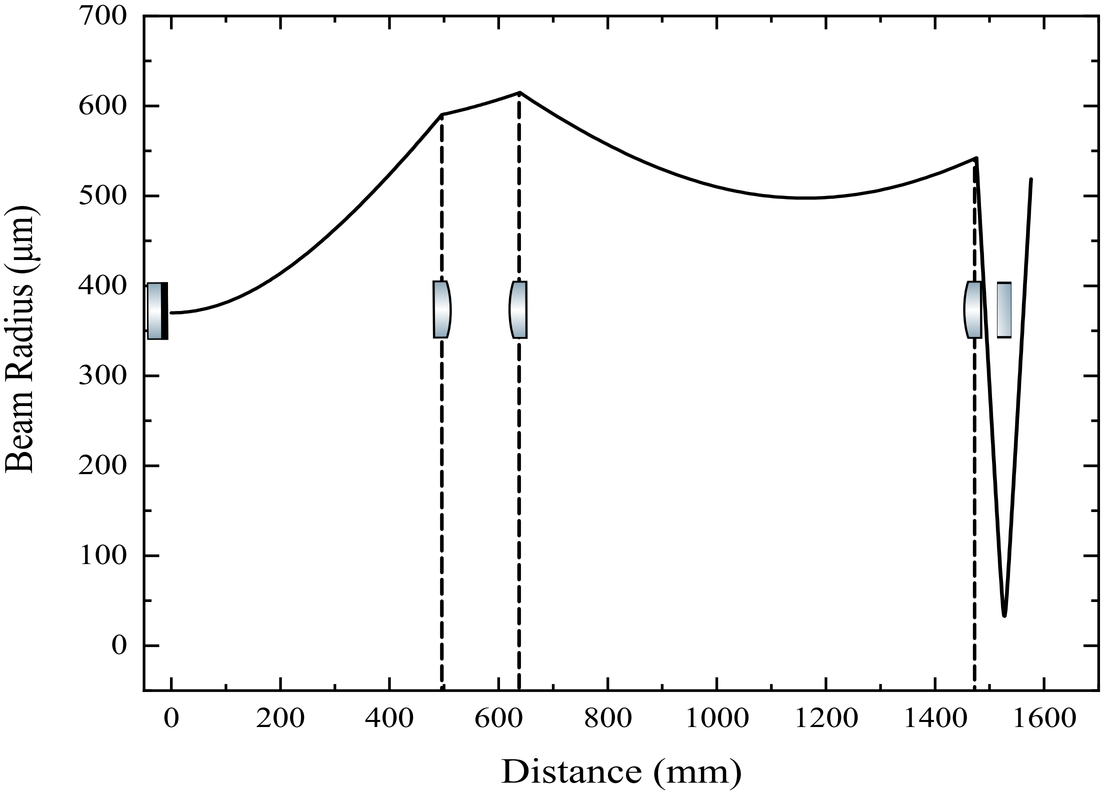

Figure 5.5: Graph of the modelled radius of the Nd:YAP from its cavity to the diamond Raman cavity. Lenses were used over the total beam path to collimate and focus the beam and achieve a focus radius similar to the one from the previous setup.

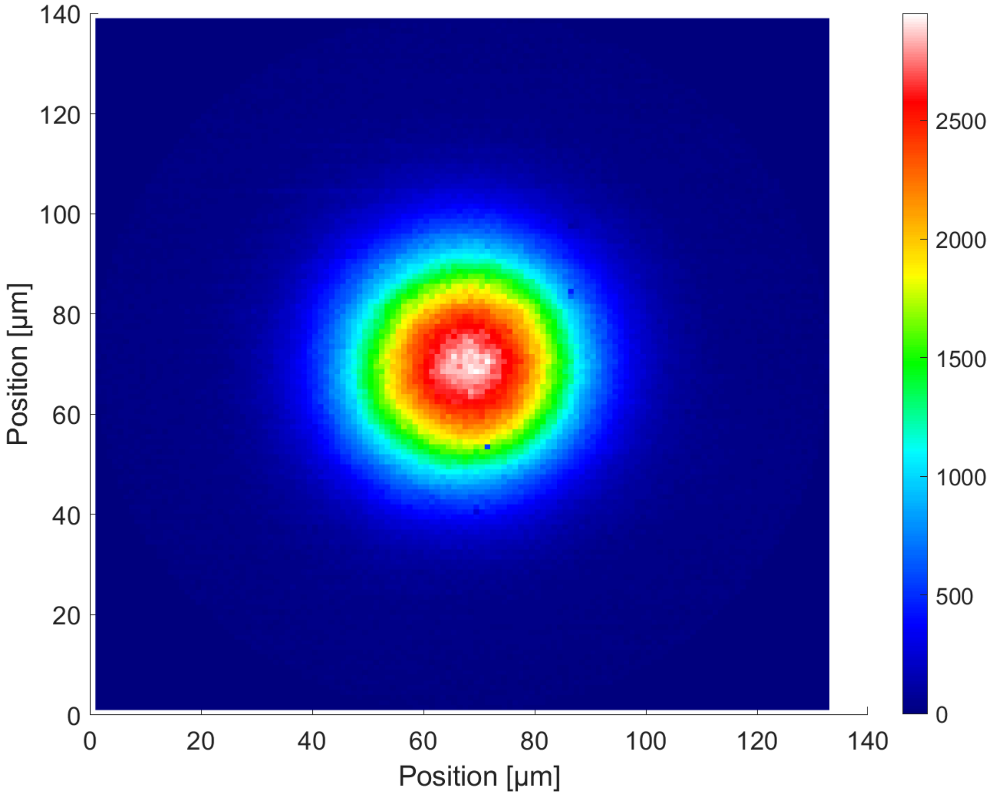

Figure 5.6: Graph of the beam intensity of the 1083 nm Nd:YAP laser in space measured at its focus.

crystal is calculated to be 67 µm. As the final lens is on an xyz stage the exact spacing is unlikely to mirror exactly the one in the laboratory as it is adjusted to yield the highest output however the modelled radius gives a good indication of what is expected. In the laboratory the D4σ beam radius at focus in free space was measured using a Spiricon sp620U beam profiler the results of which is shown in figure 5.6. This value was further analysed by fitting a Gaussian to the resulting data.

The measurement gives a beam radius of the 1083 nm laser at focus of 65 µm with a Rayleigh range of 9 mm. This was calculated by averaging the x and y plane radii from the result. This is quite close to the theoretical result with the difference likely arising from the impact the diamond will have on the beam path. From Snell's law and taking into consideration diamonds' refractive index, we expect the beam focus to likely be larger within the diamond than in free space. Additionally, simplifications made by ReZonator when calculating the caustic over the entire setup such as perfect alignment and ideal optical surfaces will also result in measurable differences.

When observing the difference in focus radius compared to the previous setup, it is important to consider the damage threshold of the AR coating of the diamond. As a reminder, this is of the order of 10 J/cm^2. From the results of the modelling in Chapter 2, which used the previous radius to find the energies of the different fields found in the Raman cavity and the calculation of the fluence at the focus found in graph 3.4, care will be taken to limit the pump pulse energy to well under 150 µJ to avoid any damage to the coatings.

5.2.2 New EDFA wavelength

The next improvement made to the setup was to change the wavelength of the DFB so that it would match the wavelength of the 1083 nm Nd:YAP Stokes shifted twice. To achieve this, the 1515 nm DFB was replaced by a 1521 nm DFB. This allows the EDFA to be well within its operating range and therefore minimise the amount of ASE during the seed pulse. Changing the wavelength of the seed to one better suited to the gain range of the EDFA, will also increase the amplification within the EDFA and as such the average power of the EDFA output.

The output spectrum of the DFB and of the EDFA output operating in CW mode were measured using a Thorlabs OSA 205 C spectrometer with a resolution of 1.5 pm at 1500 nm. For the measurement of the DFB spectrum, the DFB was driven by an 85 mA current.

Graph 5.7 shows the normalised spectra of the output of the DFB in a CW regime depending on the temperature. As was outlined in the specifications of the DFB, the peak emission has a 0.1 nm/°C dependence between wavelength and temperature, the same as the 1515 nm DFB. At 25 °C, the peak wavelength is measured to be 1520.2 nm and 1522.2 nm at 45 °C both with a linewidth of 0.15 nm. The intensity of the ASE peaks of the spectra are worth discussing as they are significantly higher than would be expected given the DFB laser's specified side-mode suppression ratio (SMSR) of 35 dB.

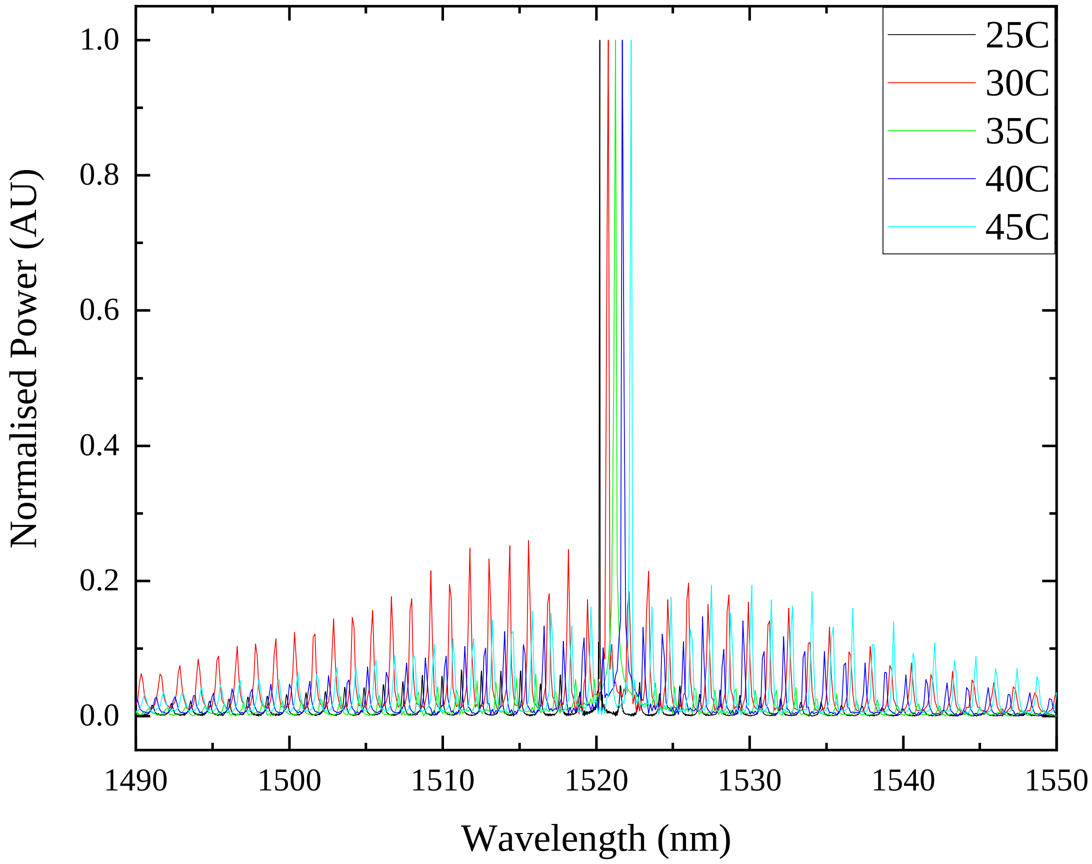

Figure 5.7: Spectra of the DFB depending on its temperature between 25 and 45 °C with 5 °C increments.

This is likely due to inefficiencies in coupling the DFB output into the spectrometer. Additionally, the relatively low CW saturation of the spectrometer of 10 mW, which is close to the specified operating CW power of the DFB when driven by 85 mA, may also contribute to the discrepancy observed.

The spectrum of the EDFA output in CW operation was measured with the 1521 nm DFB coupled into it, using a pick-off placed right after the output fibre of the EDFA. For reference the overall layout of the setup is shown in figure 5.4. For this measurement the gain of the EDFA, controlled by an etalon within the EDFA setup as discussed in section 3.8.1, was modified to maximise the output power measured for the different DFB operating temperatures. Care was taken to not exceed the 10 mW saturation with the output power of the EDFA being measured and the driving currents

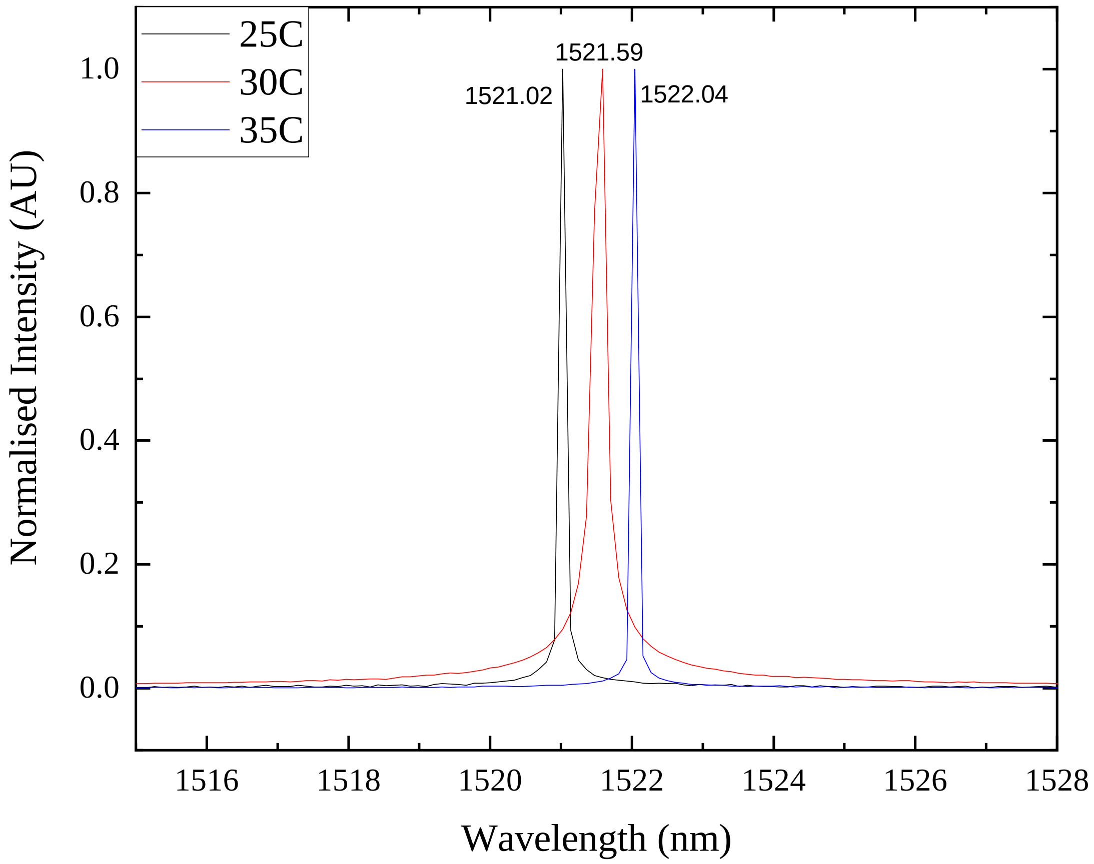

Figure 5.8: Spectra of the EDFA depending on the operating temperature of the DFB.

modified accordingly.

Shown in figure 5.8 the recorded spectra have a linewidth of 0.2 nm conserving the small linewidth of the DFB but without any ASE measurable. The peak wavelengths are slightly different from those measured at the DFB output however, this discrepancy could stem from a misalignment with the etalon in the EDFA or from variations in the EDFA's gain spectrum. This difference, however, is negligible and unlikely to affect the performance of the D-MOPA setup.

Of note the change of DFB also had a sizeable impact on the output power of the EDFA at a constant drive current of 85 mA increasing from 3 mW using the 1514 nm DFB, with the three EDFA pump lasers driven by 500 mA, 700 mA and 700 mA respectively, to 68 mW with pump currents of 250 mA, 250 mA and 250 mA. Not only is the output power higher with the new wavelength of the DFB but the pump powers had

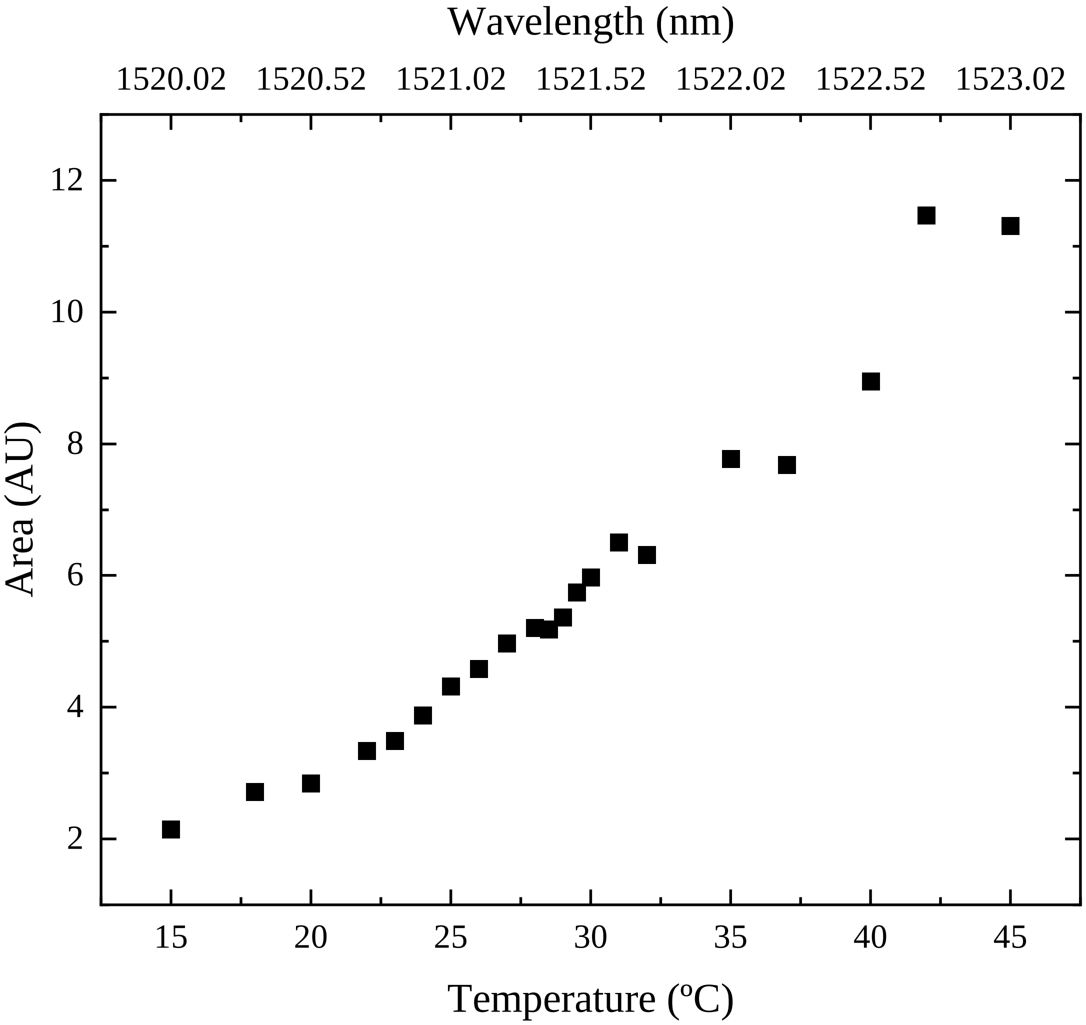

Figure 5.9: Pulse area of the EDFA seed laser in function of the operating temperature of the DFB and therefore its wavelength. The area was maximised at each temperature point using the etalon integrated in the EDFA.

to be lowered to ensure that the photodiode used to measure the amplification ratio was not saturated and had left enough range to measure any amplification. The increase in power as the wavelength is increased is demonstrated in figure 5.9 where the area of the EDFA in pulsed mode measured by the photodiode in function of the temperature of the DFB. At each temperature point the area was maximised using the EDFA etalon.

Having characterised the new 1521 nm seed laser and integrated the 1083 nm Q-switched Nd:YAP laser into the D-MOPA setup the system was ready to be tested.

5.3 Optimised D-MOPA results and considerations

The diamond Raman cavity was aligned with the 7 mm diamond sample as the Raman active crystal. The input and output coupler used were the same as for the previous setup. The input coupler was plane and highly transmissive at 1079 nm and 1515 nm (R<2%) and highly reflective at 1261 nm (>99.9%). The curved (ROC = 50 mm) output coupler was highly transmissive at 1515 nm (R<2%) and highly reflective at 1079 nm and 1261 nm (>99.9%). The methods used to measure the characteristics of this optimised setup were the same as for the previous setup as described in Chapter 3. With this setup, 1^{st} Stokes emission was found to have a threshold of 50 µJ which is lower than the previous setup threshold of 80 µJ. 2^{nd} Stokes emission was also measured and found to have a threshold at 60 µJ.

5.3.1 Amplification using the optimised D-MOPA

The amplification measurements were taken at a variety of DFB temperatures to simultaneously experimentally determine the optimal wavelength to match the 2^{nd} Stokes wavelength and, as in figure 5.3, ensure the measured result is amplification. The 1083 nm pump pulse energy was kept to 100 µJ with a pulse duration of 40 ns. The seed pulse duration was chosen to be 100 ns to make it easier to align temporally with the pump pulse. This also made the wavelength dependant amplification more identifiable due to the difference in pulse duration as shown in figure 5.11. The 1083 nm Nd:YAP pump laser pulse energy was kept at 100 µJ as, at a higher pump pulse energy, the parasitic 2^{nd} Stokes emission became too strong and made it more difficult to separate this emission and the desired amplification; however, at lower pump pulse energies the amplification becomes too small to measure.

From figure 5.10 we can see the amplification factor peaks at 15 °C which corresponds to a seed wavelength of 1520 nm. At 15 °C the average amplification factor was measured to be of ×1.15 which is an improvement on the ×1.07 presented earlier; however, this is still not as high as what was calculated to be theoretically possible; approximately ×3.9 as taken from figure 2.7. The error bars were estimated from the standard deviation

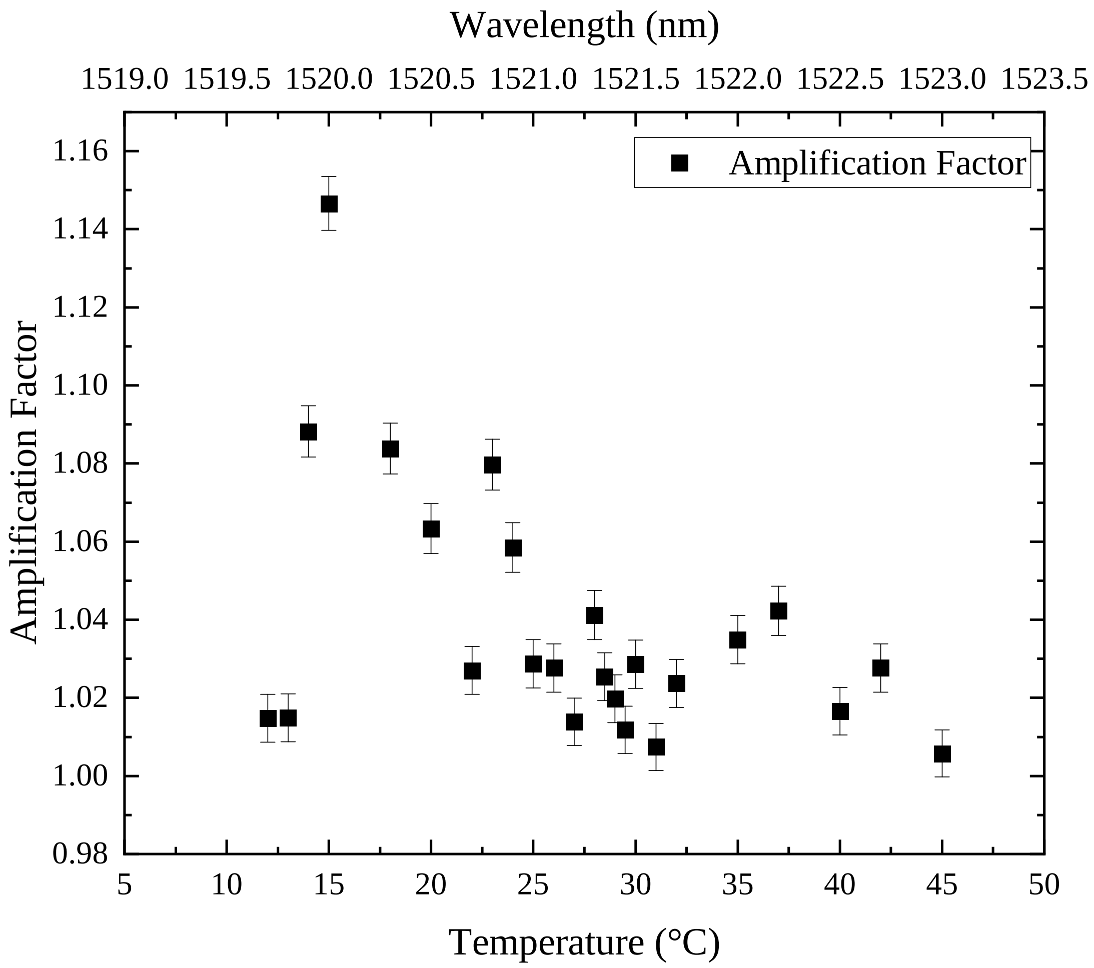

Figure 5.10: Graph of the measured amplification in function of the temperature and therefore wavelength of the DFB seed laser with the optimised D-MOPA setup.

of 64 single shot measurements. This uncertainty was propagated through the pulse integration and amplification ratio calculations resulting in an estimated relative error of 6% on the amplification factor found. Further insights can be gained by analysing the undampened outputs of the D-MOPA presented in figure 5.11. To achieve this the ND filter in front of the photodiode was removed and the output of the D-MOPA was measured for three operating conditions: with both the seed and pump pulses, with only the seed pulse, and with only the pump pulse coupled into the D-MOPA cavity. With only the pump pulse, the output measured is expected to be only the parasitic 2^{nd} Stokes output which will allow us to measure the impact it has on the

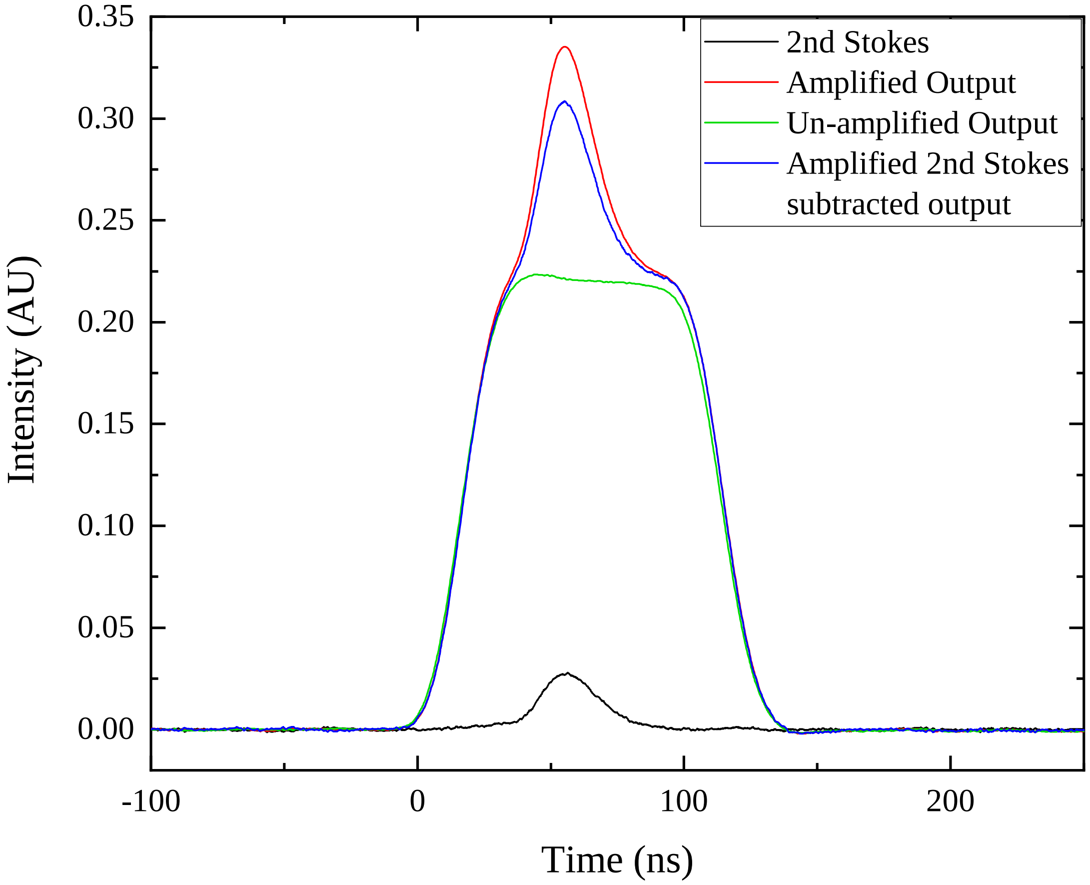

Figure 5.11: Graph of the outputs of the optimised D-MOPA under different operating conditions: with seed and pump pulses in red, with only the seed pulse in green, and with only the pump pulse coupled into the D-MOPA cavity in black. The calculated 2nd Stokes subtracted amplified output is also present in blue to compare to the amplified output.

amplification result. The curve of the parasitic 2^{nd} Stokes subtracted amplified output is also presented as a comparison.

The ratio of the area of the amplified output with the 2^{nd} Stokes curve subtracted to the un-amplified output was calculated to be of ×1.11 whereas that of the amplified to un-amplified output was found to be ×1.15. This confirms that the measured output is likely to be the amplified seed when both seed and pump lasers are coupled into the cavity however it also confirms the presence of parasitic 2^{nd} Stokes oscillation. This also reinforces the need for the ND filter so that the weaker signal of the parasitic 2^{nd} Stokes falls below the detection threshold while still conserving the ratio of the stronger amplified and un-amplified signals. This approach allowed for approximate measurements of the amplification ratio under the assumption of negligible parasitic second Stokes generation. However, it remains an imperfect solution that likely introduces some degree of error, with the true amplification factor plausibly falling within the range defined by the two measured ratios. Furthermore, as discussed in Chapter 2, this method does not fully eliminate the influence of parasitic second Stokes emission on the amplification factor. Modelling also indicates that second Stokes emission is observed experimentally at a pump pulse energy approximately 2.5 times lower than the predicted threshold. This discrepancy between the theoretical and measured thresholds is presumably due, at least in part, to the simplifying assumptions made in the model, though it warrants further investigation.

Another point of discussion that bears mentioning is how the amplification ratio is being calculated. For consistency and to allow comparison to the previously presented setup, the ratio of the areas was taken to represent this ratio. However, especially due to having minimised the timing jitter another method of calculating the ratio can also be considered. From figure 5.11, it is obvious that, when calculating the ratio of areas, a vast majority of the area will be that of the seed pulse that does not experience amplification. Therefore, we can define an instantaneous amplification ratio which represents the ratio between the intensity of both amplified and un-amplified outputs at a specific time. Using this method an instantaneous amplification ratio of ×1.5 can be calculated from the amplified and un-amplified curves in figure 5.11 and the instantaneous amplification ratio for the parasitic emission subtracted curve is ×1.4. This is already much closer to the theorised amplification ratio of ×3.9.

5.3.2 Observations during operation

During the measurements of the amplification factor for all the setups and results, a reoccurring problem was experienced. Once aligned the cavity would slowly stop emitting any of the desired outputs. Additionally, bright flashes were observed when re-aligning to positions on the diamond that the cavity had already been aligned to, or when using higher than usual pump pulse energies (but still under the estimated LIDT

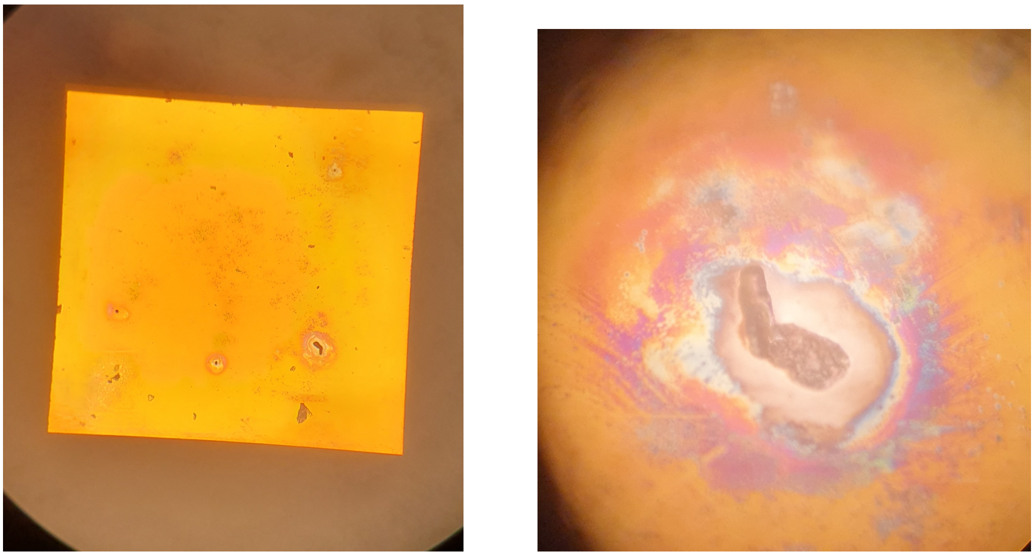

Figure 5.12: Photos of the diamond surface closest to the focus under microscope with on the left the surface at 50× magnification and on the right the damage site at 400× magnification.

of the diamond coatings) to facilitate oscillation within the cavity. This is likely due to the formation of plasma at the surface of the coating and is a recognised sign of coating damage [90]. When this was observed, a different spot on the diamond was chosen and alignment had to be restarted; however, that does not mean that the damage might not have affected future measurements. Due to the natural characteristics of diamond and especially its very low coefficient of thermal expansion certain coatings on diamond are prone to delamination [91–93]. This is potentially exacerbated in our case where a damage site could trigger local delamination of the coating, affecting an area larger than the initial damage site itself. This delamination would leave the surrounding region more susceptible to subsequent damage events. Additionally, the initial damage may generate debris such as fractured coating material or contaminants that redistributes onto adjacent surfaces, further increasing the likelihood of secondary damage.

Near the end of the measurements with the 7 mm diamond the cavity became more and more difficult to align and repeatable oscillation behaviour became unfeasible. Notably after operating for over an hour to take the measurements shown in graph 5.10, where the 2^{nd} Stokes emission from the D-MOPA was measured to have a constant amplitude during the next hour of operation, the emission gradually diminished until no oscillation could be achieved by the cavity. Additionally, after repeated attempts to re-align the cavity with the diamond sample in the same position, alignment became increasingly difficult marking a significant change in behaviour from its initial alignment. This could be explained by a slow degradation of the coating due to accumulation of damage. This was confirmed by observing and imaging the diamond surfaces under a microscope. From figure 5.12 we can see clear sites of damage as the darker spots with discolouration in a larger area around these sites. It is also clear to see that around the main damage sites characterised by large black spots there is an area of discolouration in white. This is likely due to the fields within the cavity attempting to oscillate with different spatial modes and/or the attempts to re-align the cavity with the diamond in the same position. This seems to confirm the impression that, after a certain amount of time, the original alignment would become worse and worse until it was extremely difficult to achieve lasing. This accumulation of damage to the coating would also explain the growing difficulty in aligning the laser at any spot as the more damage sites were created, the more likely the performance of the coating as a whole would worsen. To better understand and analyse the various mechanism through which coatings degrade, we must first investigate what coatings are and their characteristics.

5.3.3 Coating Aside

Optical coatings are a tool used in optics to achieve many different results. They can be used to increase the reflectivity of a material, to manipulate the polarisation or, the case on which we will be focusing, to reduce the reflectance of a surface due to Fresnel reflections [94–96]. Anti-reflection coatings are used in many different applications, such as camera objectives, optical windows, and laser crystals. For laser crystals, the simplest form of coating is a thin film coating of a different material applied to the lasing material so that the reflectance at normal incidence of a target wavelength or range of wavelengths are reduced. This helps reduce the losses in the laser cavity and therefore the lasing threshold.

This is achieved, in the simplest case, by coating the lasing material with a single quarter-wave layer of a material which has a refractive index as close as possible to the geometric mean value of the refractive indices of the laser material and the surrounding medium (usually air) such that: $n_1 = \sqrt{n_0 n_2}$. Where n_1 is the refractive index of the coating material, and n_0 and n_2 are the refractive index of the other two media. This results in two reflections from the coated material and the coating having equal magnitude but that are π-radians out of phase and so cancel each other out due to destructive interference. In our case where the light is travelling through air and then diamond, this would mean a coating material with a refractive index of 1.56. One coating often used on diamond due to its robustness and durability is silica (SiO_2) with a refractive index of 1.46 [92, 97, 98].

In the vast majority of cases, coating damage arises from one of two mechanisms: thermal induced damage and inclusions initiated damage demonstrated in figure 5.13 [94]. For thermal damage, it is due to the absorption of laser radiation within the coating material which results in an excess of thermal energy which leads to catastrophic failure by mechanical disruption or overheating. This excess heat causes delamination due to the expansion of the coating material and cracking of the thin film. In extreme cases it can even cause the coating to reach its melting point which causes it to evaporate and can change its crystalline structure. At the centre of the laser beam these effects cause a discolouration and an increase in the surface roughness. This leads to a dramatic change in the quality of the coating and makes the area in which the damage is localised impractical for laser use.

An analytical description of the instantaneous heating of the coating material in the area of the laser beam is based on the heat diffusion equation such that [94]:

$$\Delta T = \frac{2\beta_s P}{\pi^{3/2} k w} \tan^{-1}\left(\frac{16\kappa t_l}{w^2}\right)^{1/2}. \tag{5.1}$$

Where the temperature rise ΔT in the centre of the Gaussian beam profile of diameter w and power P is dependant on the thermal properties and the surface absorption of the coating material with k being its thermal conductivity, κ its thermal diffusivity and β_s its surface absorption. t_1 is the irradiation times and for large t_1 compared to the typical diffusion time w^2/κ the equation can be reduced to an asymptotic approximation:

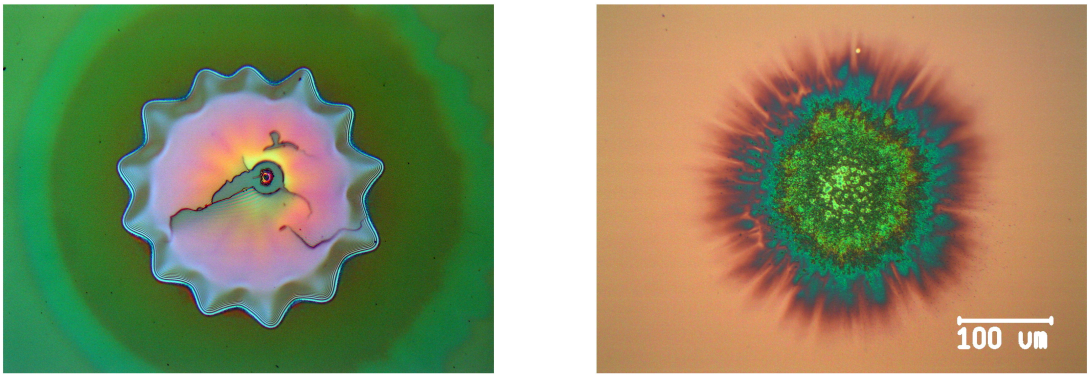

(a) (b)

Figure 5.13: Nomarski micrograph showing two different types of thermal damage induced on coatings: (a) delamination of the coating caused primarily by extreme mechanical stress, and (b) damage due to melting and re-crystallisation of the coating material due to absorption. More information on the conditions used to generate these results can be found from paper [94]. Reproduced from Ristau et al., Thin Solid Films, 2009, with permission from the publisher.

$$\Delta T \rightarrow \frac{\beta_s P}{\pi^{1/2} k w} \qquad t_1 \rightarrow \infty \tag{5.2}$$

From this we can determine that for long irradiation times, the temperature rise is dependant on the P/w ratio. Comparatively, at short irradiation times the temperature rise scales with P/w^2. This shows the critical dependence of the laser induced damage threshold (LIDT) on the size of the irradiation area and its duration.

Damage at inclusion sites is caused by a different effect. The damage is no longer initiated by absorption of the irradiation by the coating material but by defects embedded in the layer structure which posses a significantly higher absorption than the surrounding material. This is evidenced by numerous craters in the laser beam area, the underlying theory of which is beyond the scope of this report but can be found in [94]. To summarise, this effect is dependent on the interaction of a sphere, an approximation of the shape of an inclusion, inside the layer material of specific properties, specifically the melting point of the layer material. The quantitative assessment of inclusion damage is very difficult to achieve due to the challenge in precisely determining the various parameters. A typically used approximation is to purposefully imbed gold nano-particles into the coating and analyse the LIDT of the target coating with and without the particles.

An important consideration to keep in mind especially for coatings applied to diamond is that the LIDT of a coating is dependant on many different characteristics as shown by equation 5.1. Indeed, both the material of the coating and the coated material have an impact on how the temperature rise at the centre of the irradiation area behaves. Looking at the coated material, diamond is a difficult material to work with. Due to its low surface energy, it being unreactive, and its low thermal expansion coefficient, it is difficult to minimise the level of stress of the coating. Because of this the potential for delamination of the coating due to thermal or intrinsic stress is significant [99]. Another important factor which was shown in the paper by Jiao et al [100] is the surface roughness of the coated material. The rougher the surface the coating was being deposited on, the lower the LIDT of the coating was. Diamond, being a very hard material, is difficult to polish. The surface roughness of our samples was quoted by Element 6, the supplier, as less than 5 nm average roughness. This roughness is quite

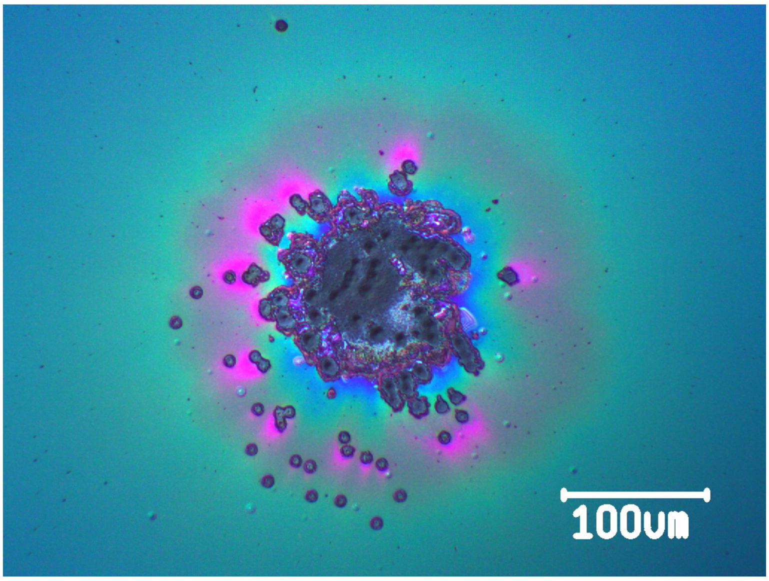

Figure 5.14: Nomarski micrograph showing damage due to inclusions within the coating. More information on the conditions used to generate these results can be found from paper [94]. Reproduced from Ristau et al., Thin Solid Films, 2009, with permission from the publisher.

significant and is likely to contribute to lower LIDT. A final point to consider is the number of layers deposited to make the coating. From Song et al. [101] we can see that the thickness of the layers and the amount of them can have an impact on the overall LIDT of the coating with thicker coatings (2.7 µm) having lower LIDT (12±3 J/cm^{-1}) than thinner (0.7 µm) coatings (21±2 J/cm^{-1}) of HfO_2/SiO_2 on a BK7 substrate.

From figures 5.13 and 5.14 reproduced from [94] and the discussion about coatings presented, we can determine that the likely cause of damage to the coating on our diamond sample is due to thermal effects. The characteristic darker centre with a large area of discolouration is very similar to the results of thermal damage described earlier in figure 5.12. The overestimation of the diamond coatings' LIDT at 10 J/cm^2 likely results from relying solely on a visible inspection test. We can posit that even when under the 10 J/cm^2 fluence limit that was determined, invisible damage was still occurring and over several pulses it achieved a critical amount of absorption to result in catastrophic damage to the coating. This would explain the increasing difficulty in aligning the laser and the damage that was shown in figure 5.12. From this, we can note that, although the intracavity amplification setup does show promise, the LIDT of the coatings on the diamonds sample was too low especially in pulsed regimes to handle the desired intracavity field energies.

Due to the lack of information about the coating material, thickness etc it is not possible to quantitively determine what a theoretical LIDT of the coating is and therefore a more in depth investigation of the LIDT of the coatings, such as the method described in ISO 11254 [102], would allow for a more suitable D-MOPA design.

5.4 Conclusion

In conclusion, we increased the amplification factor from ×1.05 to ×1.15 while using only one-third of the pump pulse energy, by addressing the timing jitter with an EOM to shape and time the EDFA seed pulses, increasing the diamond sample length, and adjusting the seed and pump wavelengths to lie within the optimal range of EDFA operation. This proof of concept setup, in parallel to the theoretical model explored in Chapter 2, shows the promise of diamond Raman amplification as a last stage amplifier to compliment more mature eye-safe range technologies such as rare earth doped glass amplifiers. Certain limitations do still exist however, with the main two discussed in this chapter being first the parasitic oscillation of a 2^{nd} Stokes field within the cavity, which draws energy from the 1^{st} Stokes field and reduces the achievable amplification, and second the fluence limitation of the coating LIDT. A possible way around both would be to consider an external cavity amplifier similar to that demonstrated in McKay et al [6] which yielded an amplification ratio of $\times 5.8$ on ns pulses; however, this would not be able to benefit from the strong intracavity fields that the setup presented in this work used.

Chapter 6

Conclusion

This thesis explored the potential of using a diamond master oscillator power amplifier setup to reach the stringent requirements of LIDAR sources particularly Doppler LIDAR devices operating in external environments such as in wind farms. As presented in the introduction, the sources for these devices need both high average power, spatial and spectral quality, and an output wavelength within the "eye-safe" wavelength range.

6.1 Summary of findings

A proof-of-concept D-MOPA setup was analysed and developed to serve as a last stage amplifier to existing sources within the "eye-safe" wavelength range such as the more mature erbium doped fibre amplifiers (EDFAs). As such, the main characteristic assessed within the setup was its amplification ratio. Thermal and power management were considered secondary concerns due to the choice of diamond as the gain medium. Diamond's exceptional thermal conductivity and optical properties make it a robust material for high-power laser applications as documented within the literature. This established capability of diamond Raman lasers to operate under high-power conditions justified focusing the investigation on amplification performance.

In pursuit of this aim as shown in the second chapter, a program was developed to simulate power transfer dynamics within a Raman amplifier cavity. This simulation enabled the evaluation of initial parameters that would otherwise have been time consuming and costly to determine experimentally. Specifically, it was found that a top-hat temporal pulse shape and the precise timing of seed pulses were critical to the D-MOPA's performance. The top-hat shape allowed for a fourfold increase in timing tolerance when the delay was modulated, compared to a Gaussian pulse shape. It also highlighted the effect of longer diamond samples on the amplification factor and helped guide the choice of anti-reflection coatings for the diamond surfaces. The program additionally revealed limitations associated with higher pump pulse energies, particularly the possible onset of parasitic second Stokes emission, which adversely affects the amplification factor.

The theory and design requirements for a proof-of-concept D-MOPA were subsequently explored in the third chapter. This highlighted the necessity of a high pump pulse energy to reach the Raman threshold, a requirement fulfilled by a Q-switched Nd:YAP laser the design of which was also examined in detail. The full proof-of-concept setup, originally build and presented by Lukasz Dziechciarzyk's in his thesis [65], was introduced here along with the results of its re-characterisation carried out during this work. The initial results obtained from this original setup, along with the limitations identified were presented and discussed. These results showed an average amplification factor of ×1.08 which was constrained by several factors: parasitic second Stokes emission, an approximate 100 ns timing jitter between the seed and pump laser pulses, and suboptimal seed laser performance resulting from a mismatch between the 1079 nm output of the Nd:YAP pump laser and the optimal operating range of the EDFA seed laser. Additional measurements taken by the author of this thesis confirmed these limitations and provided further insight into their underlying causes.

In the fourth chapter of the thesis, the tuneability of the Nd:YAP setup was explored in order to better align the wavelength of the resulting 2^{nd} Stokes shift within diamond to that of the EDFA optimal operating range. It was found through literature examination and modelling, that using a BRF as a tuning element within the cavity the 1083 nm emission peak of Nd:YAP could be targeted. This would yield a 2^{nd} Stokes wavelength of 1521 nm which is within the operating range of the EDFA setup. A Q-switched 1083 nm Nd:YAP laser setup was designed and its components presented. This is to the knowledge of the author the first time a 1083 nm Q-switched Nd:YAP laser has been achieved. The reported setup produced a pulse energy of 500 µJ with a pulse duration of 38 ns. It has an average M^2 of 1.19 and a spectral linewidth of 0.9 nm. These characteristics were deemed sufficient for the setup to be used as a pump laser for the D-MOPA system.

In chapter 5 this improved pump laser as well as other improvements were incorporated into the D-MOPA setup and their effects were systematically evaluated. Notably the timing jitter was reduced to several ns by using an EOM to control the timing of the EDFA as well as modifying its temporal shape to a top-hat shape. An approach shown by the model to offer increased timing tolerance. Other improvements included using a 7 mm diamond sample rather than the initial 4 mm diamond and using the novel 1083 nm Nd:YAP laser. These combined improvements led to an increased amplification factor of $\times 1.15$ while requiring only half the pump pulse energy. This result reinforces the potential of diamond Raman amplification as a last stage amplifier for "eye-safe" wavelength sources. However, certain constraints continue to limit the amplification ratio. Specifically, parasitic second Stokes emission persisted even at lower pump pulse energies, and the anti-reflection (AR) coatings on the diamond demonstrated friability which poses a challenge for operating the D-MOPA at the high pulse energies required.

Further work, which could not be undertaken within the time frame of this thesis, will be presented and analysed as part of this conclusion.

6.2 Further work

Based on the results presented in this thesis, the potential for a D-MOPA last stage amplifier was explored with two principal limitations identified: parasitic 2^{nd} Stokes emission from the cavity and the susceptibility of the coatings to damage under high intracavity fluence. This further work section will first outline the potential mitigation strategies that could not be experimentally investigated within the scope of this project. Additionally, a framework is proposed to guide future work towards achieving the aims identified within the introduction. Finally, alternative methods to reach these aims that do not rely on the single cavity D-MOPA geometry, will be explored.

6.2.1 Parasitic second Stokes emission mitigation

Two methods to minimise the parasitic 2^{nd} Stokes emission are proposed. First is the introduction of a dispersive prism within the cavity to spatially separate the Stokes orders within the cavity. By aligning such a cavity to the 1^{st} Stokes wavelength, the 2^{nd} Stokes suffers increased losses due to the cavity mismatch. This method has the advantage of being relatively simple introducing only a single additional optical component within the cavity. Moreover the alignment of such a component is relatively simple depending on the prism's design. It is important to note that since the seed laser does not require to be resonant within the cavity, it is not unduly affected by the cavity mismatch.

However this method presents notable drawbacks. The addition of the prism introduces extra optical surfaces, potentially increasing the risk of parasitic reflections, sensitivity to misalignment, and overall intracavity losses. Considering the already high threshold required for the Raman effect these effects may increase the difficulty in aligning and operating the Raman cavity. Additionally, the prism must provide sufficient angular dispersion over the relatively short propagation length to ensure minimal spatial overlap between the two Stokes orders and compromise sufficiently the stability within the cavity of the 2^{nd} Stokes.

The second method leverages the wavelength dependence of the Gaussian mode size in the cavity. Since the 2^{nd} Stokes has a longer wavelength than the 1^{st} Stokes, its mode size radius is larger for the same cavity geometry as was shown in Section 3.5. By introducing a physical aperture or pinhole at or near the mode waist, the 2^{nd} Stokes can be selectively attenuated while leaving the 1^{st} Stokes unaffected. This solution is also quite simple and requires only a single additional component. Additionally the pinhole introduces no additional surfaces and therefore will not contribute to reflection or absorption losses if designed carefully.

This approach does also present drawbacks. Notably a pinhole will not entirely suppress the 2^{nd} Stokes oscillation as it primarily clips the mode edges rather than impose a hard stop. Oscillation may still occur albeit with reduced efficiency rather than complete suppression. Furthermore precise alignment of the pinhole is critical and achieving a stable alignment may require a longer cavity length to establish a well-defined mode waist and ensure selective attenuation. Such constraints would likely complicate experimental implementation.

6.2.2 Coating damage mitigation

The second key limitation identified in this thesis is the diamond AR coating's induced damage under high fluence operation within the cavity. Two potential solutions are presented, based on different approaches: one aims to better characterise the coatings to enable more informed design decisions, while the other avoids coating-related issues entirely by modifying the diamond sample geometry.

First is the performance of a proper LIDT analysis of the coatings used on the diamond as detailed in paper [94] and which is detailed as ISO-Standard in ISO 11254 [102]. This would provide a more accurate LIDT value which would allow for operation within safer margins and potentially for optimising the cavity design. With this information, more informed decisions on the cavity length, pump power and mode sizes within the cavity could be made to avoid exceeding the LIDT.

The second method proposes changing the diamond sample currently used to a Brewster-cut sample as the Raman medium. With careful orientation, the reflective losses at the diamond surface are minimised which removes the need for anti-reflection coatings entirely. This would eliminate the vulnerable anti-reflection coatings currently used and therefore increase the robustness of the system. However, there are significant practical challenges associated with this approach. First is that high quality diamond samples suitable for use within a Raman laser/amplifier are already difficult to source in large sizes and Brewster cut samples are fabricated from existing high purity samples making them on average shorter. Additionally, the precision required in the cutting and polishing of the Brewster angled faces for use in laser systems increases the difficulty of fabrication and therefore increases their cost. The second difficulty arises from the impact of a Brewster-cut sample on the cavity mode shape, which also influences the system threshold. Although methods to compensate for this anisotropy are well documented, they add complexity to the cavity design.

6.2.3 Path Toward High-Power Operation

Together, the methods proposed for suppressing parasitic Stokes emission and improving coating resilience present a comprehensive strategy to overcome the key limitations identified in the setup shown in this thesis. The natural next step toward achieving the objectives outlined in the introduction would be to replace the current pump laser. The Q-switched laser employed in this work was selected primarily to demonstrate proof-of-concept operation using an accessible and readily available source.

However, due to their inherent thermal and optical constraints, Q-switched systems are limited in repetition rate, which restricts achievable average powers. To progress toward higher power operation, a more suitable candidate would be a Yb-doped fibre laser operating near 1083 nm, a wavelength well within the optimal performance range of such systems. As discussed in the introduction, fibre lasers at this wavelength are well developed and capable of delivering high average powers. This would allow progress towards reaching the targets; repetition rates in the MHz regime and average powers of 100 W.

6.2.4 Closing Remarks

While the results presented in this work demonstrate the feasibility and promise of a diamond based MOPA system, they also provide evidence on the current constraints that limit its full potential. By addressing these limitations and implementing the proposed improvements, the system can be further developed and scaled toward the performance targets outlined in this thesis. With continued refinement, the D-MOPA setup offers strong potential as a high power amplifier for future eye-safe laser applications.

Appendix A

MATLAB Code: Simulation of power transfers within a DMOPA Raman cavity

```matlab
clear all
Integr=@Integration; %call function for later in code

% /!\ CavityLength/Cristal_section determines the time step and therefor the
%duration of calculation. The smaller the longer ! 100 section for 10mm crystal is more than enought/!\
n=2.45; %refractive index of material
Air = 0.005; %length of air on each side of the cavity in m
Ksp= 1e-9; % /metre spontaneous Raman scattering factor
CavityLength=0.010; % in metres length of the crystal care to choose suitable cristal section to cavity length or it can get stuck/get very very long 0.004
Cristal_Sections=100; %We divide cristal in this number of sections 100
Pump_Wavelenght=1079e-9; %in m
RamanShift=133200; % in m-1
```

```
Seed_delay= 1e-8; %1.8e-8 in seconds (care when changing the seed the delay as it has great impact on amplification)
Delay_scale = 0 ; %in s when wanting to do multiple runs with a constantly evolving delay
% Define the constants and parameters that are going to be used for the rest of the code

Dp=2*65*1e-6 ; %65*1e-6 , 72*1e-6 in m
    D3=1*160e-6; %160e-6 , 160e-6
    D1=169e-6; %169e-6 , 189e-6
    D2=186.5e-6; %186.5e-6 , 203.5e-6
    Ds=70e-6;
%Set the diameters of the different modes according to reZonator
% Input_Coupler = [0;0.999;0.001;0];
% Output_Coupler=[0.999;0.999;0.001;0];
Input_Coupler = [0.02;0.999;0.02;0];
Output_Coupler=[0.999;0.999;0.02;0];
a1 = [0.3;0.3;0.3;0.3];
Rp1=2*0.0318; R11=2*0.0048; R21=2*0.0032; R31=2*0.01;
Rp2=2*0.0215; R12=2*0.0046; R22=2*0.0021; R32=2*0.01;
% Rp1=2*0.005; R11=2*0.01; R21=2*0.005; R31=2*0.00;
% Rp2=2*0.005; R12=2*0.01; R22=2*0.005; R32=2*0.00;
%Determine the way the pulses will interact with each element (two mirrors
%and diamond and coating on diamond)

lbdp=Pump_Wavelenght;
lbd1=(1/((1/lbdp)-1*RamanShift));
lbd2=(1/((1/lbdp)-2*RamanShift));
lbd3=(1/((1/lbdp)-3*RamanShift));
%setup the wavelength of the different Stokes shift

k=0.9;
g0=k*16.7e-11; %m/W
```

```
G1=k*7.7e-11;
G2=0;
%Effective gain of the different Stokes wavelengths (from Vasili paper)

Ap1=(pi/2)*(0.25*Dp*Dp+0.25*D1*D1);
A12=(pi/2)*(0.25*D2*D2+0.25*D1*D1);
A23=(pi/2)*(0.25*D2*D2+0.25*D3*D3);
A1s=(pi/2)*(0.25*Ds*Ds+0.25*D1*D1);
%setup of the effective core area needed for main calculations

a2=[(Rp1+Rp2)/CavityLength;(R11+R12)/CavityLength;(R21+R22)/CavityLength;(R31+R32)/CavityLength];
a=a1.*CavityLength+a2;
%setup of the losses a pulse will incure in the cavity

Gp=g0*(1)/(1*Ap1); G11=g0*(lbd1/lbdp)*1/(1*Ap1);
G12=G1*1/(1*A12); G21=G1*(lbd2/lbd1)*1/(1*A12);
G22=G2*1/(1*A23); G31=G2*(lbd3/lbd2)*1/(1*A23);
G1s=G1/(A1s); Gs1=G1*(lbd2/lbd1)/A1s;
%setup of coefficients used in the later calculations of the change in power

Pulse_Duration=36e-9; %s
Pulse_Duration_s=100e-9; %s
% Pulse_Duration_s=70e-9; %50ns at 0.0001J

Pulse_Duration_scale=0;
%Determins the duration of the respective pulses and the scale it needs if
%running multiple runs with changing pulse duration

Starting_Energy=0.0001; %in J (0.0001)
Start_Power_s=0.9; % (0.9)in W
```

```
Starting_Energy_s=Start_Power_s*Pulse_Duration_s; %in J
Repetition_Rate= 20;%in Hz

Scaling = 0.00000;
Scaling_s = 0;
Number_of_Runs = 1;
%determine initial parameters and the number of runs

NbrSection = Cristal_Sections+2;
SectionSize = CavityLength/Cristal_Sections;
TimeStep=SectionSize*n/(2.99792458e8);
%setup of parameters and setup of the cavity ie how it is divided and the
%corresponding timestep

Conv_Eff=zeros(1,Number_of_Runs);
Input_Energies=zeros(1,Number_of_Runs);
Output1s=zeros(1,Number_of_Runs);
Output2s=zeros(1,Number_of_Runs);
Output3s=zeros(1,Number_of_Runs);

% [den,num]=custom_butter(1,0.0001);
den = [1.570549638351682e-04,1.570549638351682e-04];
num = [1,-0.999685890072330];
%Setup of the output vectors to be later filled + butter from averaging
%and smoothing

for Energie_Scale=1:Number_of_Runs

%real time information for user while code is running
run=Energie_Scale
Runs_to_do_next=Number_of_Runs-Energie_Scale

```

```
tic

%PULSE
Pulse_Energy=Starting_Energy+(Energie_Scale-1)*Scaling; %J
Pulse_Energy_s=Starting_Energy_s+(Energie_Scale-1)*Scaling_s; %J
Seed_delays= Seed_delay+(Energie_Scale-1)*Delay_scale;
Power_s=Start_Power_s+(Energie_Scale-1)*Scaling_s;

FWHM=Pulse_Duration;
Sigma=FWHM/ (2*sqrt(2*log(2)));
Pulsetime=6*Sigma;
Pulse_middle=(Pulsetime+Seed_delays)/TimeStep ; %find position in array of seed pulse middle%
%Setup of the various parameters needed to model both pump and seed pulse

SimulationSteps=3*(Pulsetime/TimeStep);
Pulse=zeros(1,floor(SimulationSteps));
Pulse_s=zeros(1,floor(SimulationSteps));
%Determines size of the arrays/precision of the pulses and setups the
%pulses arrays

for t=1:1:length(Pulse)
    Next_Pulse= Pulse_Energy*(1/(sqrt(2*pi)*Sigma))*exp(-(t*
       TimeStep-Pulsetime)^2/(2*(Sigma^2)));
    Pulse(t)=Next_Pulse;
    if Next_Pulse<1e-10
        for t2 = t:1:floor(SimulationSteps)
            Pulse(t) = 0;
        end
        break
    end
end
```

```matlab
%creates the pump pulse

for i = floor(Pulse_middle-1/2*Pulse_Duration_s/TimeStep) : floor(Pulse_middle+1/2*Pulse_Duration_s/TimeStep)
  Pulse_s(i) = Power_s;
end

%creates the seed pulse

Air_Space = floor(Air/(2.99792458e8)/TimeStep/2);
Cavity = ones(4,2,NbrSection+2*Air_Space)*Ksp*SectionSize;
OutputP=zeros(4,floor(SimulationSteps));
Saved_Section=zeros(4,2,NbrSection+2*Air_Space);
%sets up the various matrices needed for the next part

for Step=1:SimulationSteps
    Entering_pulse=Pulse(floor(Step))*(1-Input_Coupler(1)); % apply 1st mirror Transmitence
    Seed_Pulse = Pulse_s(floor(Step))*(1-Input_Coupler(3)); % apply 1st mirror Transmitence

    Saved_Section=Cavity;
    for Section=1:NbrSection+2*Air_Space
        %Entrance

        if Section==1
            %Saved_Section(:,:,Section)=Cavity(:,:,Section);
            Cavity(:,1,Section)=[Entering_pulse;0;0;0]+(Saved_Section(:,2,1)).*Input_Coupler;
            Cavity(:,2,Section)=Saved_Section(:,2,2);
            Cavity(4,1,Section)=[Seed_Pulse]+(Saved_Section(4,2,1))*Input_Coupler(3);
            Cavity(4,2,Section)=Saved_Section(4,2,2);

```

```
        elseif Section <= Air_Space+1 && Section > 1
            Cavity(:,1,Section)=Saved_Section(:,1,Section-1);
            Cavity(:,2,Section)=Saved_Section(:,2,Section+1);

        elseif Section <= Air_Space+NbrSection-1 && Section > 1+Air_Space
            Saved_Section(1,1,Section)=Saved_Section(1,1,Section)*(Saved_Section(1,1,Section)>0); Saved_Section(1,2,Section)=Saved_Section(1,2,Section)*(Saved_Section(1,2,Section)>0);
            Saved_Section(2,1,Section)=Saved_Section(2,1,Section)*(Saved_Section(2,1,Section)>0); Saved_Section(2,2,Section)=Saved_Section(2,2,Section)*(Saved_Section(2,2,Section)>0);
            Saved_Section(3,1,Section)=Saved_Section(3,1,Section)*(Saved_Section(3,1,Section)>0); Saved_Section(3,2,Section)=Saved_Section(3,2,Section)*(Saved_Section(3,2,Section)>0);
            Saved_Section(4,1,Section)=Saved_Section(4,1,Section)*(Saved_Section(4,1,Section)>0); Saved_Section(4,2,Section)=Saved_Section(4,2,Section)*(Saved_Section(4,2,Section)>0);
            %Saved_Section(:,:,Section)=Cavity(:,:,Section);
            Pf=Saved_Section(:,1,Section-1); %Forward
            Pb=Saved_Section(:,2,Section+1); %Backward
            Pf1=Pf(1); Pb1=Pb(1);
            Pf2=Pf(2); Pb2=Pb(2);
            Pf3=Pf(3); Pb3=Pb(3);
            Pf4=Pf(4); Pb4=Pb(4);

       dP=[[-G11*(Pb2+Pf2)*Pf1-a(1)*Pf1 -G11*(Pf2+Pb2)*Pb1-a(1)*Pb1 ];
        [Gp*(Pb1+Pf1)*Pf2+Ksp*Pf1-G21*(Pf3+Pb3)*Pf2-Gs1*Pf4*Pf2-a(2)*Pf2 Gp*(Pf1+Pb1)*Pb2+Ksp*Pb1-G21*(Pf3+Pb3)*Pb2-a
```

```
(2)*Pb2];
        [G12*(Pb2+Pf2)*Pf3+Ksp*Pf2-G31*(Pf4+Pb4)*Pf3-a(3)*Pf3 G12*(Pf2+Pb2)*Pb3+Ksp*Pb2-G31*(Pf4+Pb4)*Pb3-a(3)*Pb3];
        [G1s*Pf2*Pf4+Pf4*Ksp-a(3)*Pf4  0]];

            dP=dP*SectionSize;
            Cavity(:,:,Section)=[Saved_Section(:,1,Section-1)+dP(:,1)+[0;0;0;0] Saved_Section(:,2,Section+1)+dP(:,2)+[0;0;0;0]];

        elseif Section > NbrSection+Air_Space-1 && Section < NbrSection+2*Air_Space
            Cavity(:,1,Section)=Saved_Section(:,1,Section-1);
            Cavity(:,2,Section)=Saved_Section(:,2,Section+1);

        elseif Section ==  NbrSection+2*Air_Space

            %Saved_Section(:,:,Section)=Cavity(:,:,Section);
            Cavity(:,1,Section) = Saved_Section(:,1,Section-1);
            Cavity(:,2,Section) = (Saved_Section(:,1,Section)).*(Output_Coupler);
            OutputP(:,Step)=Saved_Section(:,1,Section).*(1-Output_Coupler);

        end

    end
end
Filtered_DepPump=filter(den,num,OutputP(1,:));
Filtered_1s=filter(den,num,OutputP(2,:));
Filtered_2s=filter(den,num,OutputP(3,:)); %filter
Filtered_3s=filter(den,num,OutputP(4,:));

Pulse_E=Pulse_Energy; %
```

```
Entering_Pulse=Pulse*(1-Input_Coupler(1));
Entering_Pulse_E=Pulse_E*(1-Input_Coupler(1));

Stokes1_E=Integr(Filtered_1s,TimeStep);
Stokes2_E=Integr(Filtered_2s,TimeStep);
Stokes3_E=Integr(Filtered_3s,TimeStep);

%storage step
Conv_Eff(Energie_Scale)=Stokes2_E/Entering_Pulse_E;
Input_Energies(Energie_Scale)=Pulse_Energy;
Output1s(Energie_Scale)=Stoke1_E;
Output2s(Energie_Scale)=Stokes2_E;
Output3s(Energie_Scale)=Stokes3_E;
toc
end

beep on;
beep

Time=zeros(1,floor(SimulationSteps));
for t=1:SimulationSteps
    Time(t)=(t-1)*TimeStep;
end

Conv_Eff(Energie_Scale)=Stokes2_E/Entering_Pulse_E;
Input_Energies(Energie_Scale)=Pulse_Energy;
Output1s(Energie_Scale)=Stokes1_E;
Output2s(Energie_Scale)=Stokes2_E;
Output3s(Energie_Scale)=Stokes3_E;

amplificationfactor= Output3s./Starting_Energy_s;

Conv_Eff=Output2s./Input_Energies;
Avg_pow1s=Output1s*Repetition_Rate;
```

```
Avg_pow2s=Output2s*Repetition_Rate;
Avg_pow3s=Output3s*Repetition_Rate;
Avg_pow_total=Avg_pow1s+Avg_pow2s+Avg_pow3s;
Avg_powPump=Input_Energies*(1-Input_Coupler(1))*Repetition_Rate;
Quantium_Conversion_efficiency=(lbd2/lbdp)*(Avg_pow2s./
    Avg_powPump);
Conversion_efficiency=(Avg_pow2s./Avg_powPump);
Total_Conversion_efficiency=(Avg_pow_total./Avg_powPump);

function Integral=Integration(f,dx)
    Integral=0;
    for i=1:length(f)
        Integral=Integral+f(i)*dx;
    end
end
```

Listing A.1: MATLAB code for simulating the power transfers within a DMOPA Raman cavity

Appendix B

MATLAB Code: Birefringent Filter Calculation

```
% Prompt user for input parameters
prompt = "Wavelength in nm \n";
lambda = input(prompt); % Wavelength(s) in nanometers

prompt = "Rotation angle in degrees \n";
phi = input(prompt); % Rotation angle(s) in degrees

prompt = "Angle of the optic axis to the surface \n";
e = input(prompt); % Angle of optic axis to surface in degrees

prompt = "Thickness of BRF in m \n";
d = input(prompt); % BRF thickness in meters

% Refractive indices for ordinary and extraordinary rays of quartz
no = 1.5443;
ne = 1.5534;
n = (no + ne) / 2; % Average refractive index

nc = 1.925; % NdYAG refractive index
```

```
q = (2 * n) / (1 + n^2); %Losses at the BRF
q2 = (2 * nc) / (1 + nc^2); %Losses at the NdYAG rod

% Calculate theta (angle related to n)
theta = atand(n);

% Calculate eta, alpha angles based on input and material parameters
eta = acosd(cosd(phi) .* cosd(theta) .* cosd(e) + sind(theta) .* sind(e));
alphat = (1 ./ (sind(eta) .* sind(theta))) .* (cosd(phi) .* cosd(e) - cosd(eta) .* cosd(theta));
alpha = acosd(alphat);
dalpha = alpha - 45;

tic % Start timer for performance measurement

% Calculate delta phase and Mb matrices for each wavelength and rotation angle
for i = 1:length(lambda)
    for j = 1:length(phi)
        delta(i,j) = (2 * pi * (ne - no) * d * (sind(eta(j)))^2) / ((lambda(i) * 10^(-9)) * sind(theta));
        Mbtemp = [ (cosd(alpha(j)))^2 + (sind(alpha(j)))^2 * exp(1i * delta(i,j)), ...
                   q * sind(alpha(j)) * cosd(alpha(j)) * (1 - exp(1i * delta(i,j)));
                   q * sind(alpha(j)) * cosd(alpha(j)) * (1 - exp(1i * delta(i,j))), ...
                   q^2 * ((sind(alpha(j)))^2 + (cosd(alpha(j)))^2 * exp(1i * delta(i,j))) ];
        Mb{i,j} = Mbtemp;
    end
end
```

```

sz1 = size(Mb);

% Calculate M matrices (product of transfer matrices)
for k = 1:sz1(1)
    for l = 1:sz1(2)
        Mtemp = ([1 0; 0 q^2] * [1 0; 0 q^2] * Mb{k,l} * Mb{k,l})
            ;
        M{k,l} = Mtemp;
    end
end

% Calculate eigenvalues of M matrices
for x = 1:sz1(1)
    for y = 1:sz1(2)
        ttemp = eig(M{x,y});
        t{x,y} = ttemp;
    end
end

sz2 = size(t);

% Calculate transmission coefficient (max eigenvalue magnitude
    squared)
for a = 1:sz2(1)
    for b = 1:sz2(2)
        Ttemp = abs(t{a,b});
        T(a,b) = (max(Ttemp))^2;
    end
end

toc % End timer, output elapsed time
```

Listing B.1: MATLAB code for calculating birefringent filter transmission matrix

Bibliography

[1] R. Balmer, J. Brandon, S. Clewes, H. Dhillon, J. Dodson, I. Friel, P. Inglis, T. Madgwick, M. Markham, T. Mollart *et al.*, "Chemical vapour deposition synthetic diamond: materials, technology and applications," *Journal of Physics: Condensed Matter*, vol. 21, no. 36, p. 364221, 2009.

[2] W. G. Eversole, "Synthesis of diamond," Apr. 17 1962, US Patent 3,030,188.

[3] R. Mildren and J. Rabeau, *Optical engineering of diamond.* John Wiley & Sons, 2013.

[4] V. G. Savitski, I. Friel, J. E. Hastie, M. D. Dawson, D. Burns, and A. J. Kemp, "Characterization of single-crystal synthetic diamond for multi-watt continuous-wave raman lasers," *IEEE Journal of Quantum Electronics*, vol. 48, no. 3, pp. 328–337, 2011.

[5] R. J. Williams, O. Kitzler, Z. Bai, S. Sarang, H. Jasbeer, A. McKay, S. Antipov, A. Sabella, O. Lux, D. J. Spence, and R. P. Mildren, "High Power Diamond Raman Lasers," *IEEE Journal of Selected Topics in Quantum Electronics*, vol. 24, no. 5, sep 2018.

[6] A. McKay, R. P. Mildren, D. W. Coutts, and D. J. Spence, "SRS in the strong-focusing regime for Raman amplifiers," *Optics Express*, vol. 23, no. 11, p. 15012, jun 2015.

[7] M. Chanin, A. Garnier, A. Hauchecorne, and J. Porteneuve, "A Doppler lidar for measuring winds in the middle atmosphere," *Geophysical research letters*, vol. 16, no. 11, pp. 1273–1276, 1989.

[8] D. Schlipf, D. J. Schlipf, and M. Kühn, "Nonlinear model predictive control of wind turbines using LIDAR," *Wind energy*, vol. 16, no. 7, pp. 1107–1129, 2013.

[9] J. Lovell, D. L. Jupp, D. Culvenor, and N. Coops, "Using airborne and ground-based ranging lidar to measure canopy structure in Australian forests," *Canadian Journal of Remote Sensing*, vol. 29, no. 5, pp. 607–622, 2003.

[10] J. Larson and M. Trivedi, "Lidar based off-road negative obstacle detection and analysis," in *2011 14th International IEEE Conference on Intelligent Transportation Systems (ITSC)*. IEEE, 2011, pp. 192–197.

[11] H. M. Tulldahl and H. Larsson, "Lidar on small UAV for 3D mapping," in *Electro-Optical Remote Sensing, Photonic Technologies, and Applications VIII; and Military Applications in Hyperspectral Imaging and High Spatial Resolution Sensing II*, vol. 9250. International Society for Optics and Photonics, 2014, p. 925009.

[12] I. Bilik, "Comparative Analysis of Radar and Lidar Technologies for Automotive Applications," *IEEE Intelligent Transportation Systems Magazine*, vol. 15, no. 1, pp. 244–269, 2023.

[13] M. Mielle, M. Magnusson, and A. J. Lilienthal, "A comparative analysis of radar and lidar sensing for localization and mapping," in *2019 European Conference on Mobile Robots (ECMR)*, 2019, pp. 1–6.

[14] S. J. Franke, X. Chu, A. Z. Liu, and W. K. Hocking, "Comparison of meteor radar and Na Doppler lidar measurements of winds in the mesopause region above Maui, Hawaii," *Journal of Geophysical Research: Atmospheres*, vol. 110, no. D9, 2005. [Online]. Available: https://agupubs.onlinelibrary.wiley.com/doi/abs/10.1029/2003JD004486

[15] P. Chazette, J. Totems, L. Hespel, and J.-S. Bailly, "Principle and physics of the LiDAR measurement," in *Optical Remote Sensing of Land Surface*. Elsevier, 2016, pp. 201–247.

[16] S. Karp and L. B. Stotts, *Fundamentals of electro-optic systems design: communications, lidar, and imaging.* Cambridge University Press, 2013.

[17] A. N. S. Institute, *American national standard for safe use of lasers.* Laser Institute of America, 2007.

[18] T. J. T. P. van den Berg and H. Spekreijse, "Near infrared light absorption in the human eye media," *Vision Research*, vol. 37, no. 2, pp. 249–253, 1997. [Online]. Available: https://www.sciencedirect.com/science/article/pii/S0042698996001204

[19] J. A. Zuclich, D. J. Lund, and B. E. Stuck, "Wavelength dependence of ocular damage thresholds in the near-ir to far-ir transition region: Proposed revisions to mpes," *Health Phys.*, vol. 92, no. 1, pp. 15–23, 2007.

[20] S. C. Tidwell, J. F. Seamans, and M. S. Bowers, "Highly Efficient 60-W TEM_{00} CW Diode-End-Pumped Nd:YAG Laser," *Optics Letters*, vol. 18, no. 2, pp. 116–118, Jan. 1993. [Online]. Available: https://opg.optica.org/ol/abstract.cfm?URI=ol-18-2-116

[21] W. Koechner, *Solid State Engineering*, 6th ed., A. W. T. Rhodes, Ed. Springer, 2006. [Online]. Available: www.springer.

[22] H. J. Eichler, A. Haase, R. Menzel, and A. Siemoneit, "Thermal lensing and depolarization in a highly pumped Nd:YAG laser amplifier," *Journal of Physics D: Applied Physics*, vol. 26, no. 11, p. 1884, nov 1993. [Online]. Available: https://dx.doi.org/10.1088/0022-3727/26/11/008

[23] W. Koechner, "Thermal Lensing in a Nd:YAG Laser Rod," *Appl. Opt.*, vol. 9, no. 11, pp. 2548–2553, Nov 1970. [Online]. Available: https://opg.optica.org/ao/abstract.cfm?URI=ao-9-11-2548

[24] M. E. Innocenzi, H. T. Yura, C. L. Fincher, and R. A. Fields, "Thermal modeling of continuous-wave end-pumped solid-state lasers," *Applied Physics*

Letters, vol. 56, no. 19, pp. 1831–1833, 05 1990. [Online]. Available: https://doi.org/10.1063/1.103083

[25] W. A. Clarkson, "Thermal effects and their mitigation in end-pumped solid-state lasers," *Journal of Physics D: Applied Physics*, vol. 34, no. 16, p. 2381, aug 2001. [Online]. Available: https://dx.doi.org/10.1088/0022-3727/34/16/302

[26] S. Coe and R. Sussmann, "Optical, thermal and mechanical properties of CVD diamond," *Diamond and Related Materials*, vol. 9, no. 9, pp. 1726–1729, 2000. [Online]. Available: https://www.sciencedirect.com/science/article/pii/S0925963500002983

[27] S. Chénais, F. Druon, S. Forget, F. Balembois, and P. Georges, "On thermal effects in solid-state lasers: The case of ytterbium-doped materials," *Progress in Quantum Electronics*, vol. 30, no. 4, pp. 89–153, 2006. [Online]. Available: https://www.sciencedirect.com/science/article/pii/S0079672706000279

[28] P. Jacobson and S. Stoupin, "Thermal expansion coefficient of diamond in a wide temperature range," *Diamond and Related Materials*, vol. 97, p. 107469, 2019. [Online]. Available: https://www.sciencedirect.com/science/article/pii/S0925963519303851

[29] J. W. Dawson, M. J. Messerly, R. J. Beach, M. Y. Shverdin, E. A. Stappaerts, A. K. Sridharan, P. H. Pax, J. E. Heebner, C. W. Siders, and C. Barty, "Analysis of the scalability of diffraction-limited fiber lasers and amplifiers to high average power," *Opt. Express*, vol. 16, no. 17, pp. 13 240–13 266, Aug 2008. [Online]. Available: https://opg.optica.org/oe/abstract.cfm?URI=oe-16-17-13240

[30] B. Denker and E. Shklovsky, *Handbook of Solid-State Lasers: Materials, Systems and Applications.* Oxford: Elsevier, 2013.

[31] A. M. Scott and K. D. Ridley, "A Review of Brillouin-Enhanced Four-Wave Mixing," *IEEE Journal of Quantum Electronics*, vol. 25, no. 3, pp. 438–459, 1989.

[32] X. Feng, H. yaw Tam, and P. K. A. Wai, "Stable and uniform multiwavelength erbium-doped fiber laser using nonlinear polarization rotation," *Opt. Express*, vol. 14, no. 18, pp. 8205–8210, Sep 2006. [Online]. Available: https://opg.optica.org/oe/abstract.cfm?URI=oe-14-18-8205

[33] S. Mauger, L. Bergé, and S. Skupin, "Self-focusing versus stimulated Brillouin scattering of laser pulses in fused silica," *New Journal of Physics*, vol. 12, no. 10, p. 103049, oct 2010. [Online]. Available: https://dx.doi.org/10.1088/1367-2630/12/10/103049

[34] G. Nemova, "Brief Review of Recent Developments in Fiber Lasers," *Applied Sciences*, vol. 14, no. 6, 2024. [Online]. Available: https://www.mdpi.com/2076-3417/14/6/2323

[35] Y. Wang, R. Kitahara, W. Kiyoyama, Y. Shirakura, T. Kurihara, Y. Nakanish, T. Yamamoto, M. Nakayama, S. Ikoma, and K. Shima, "8-kW single-stage all-fiber Yb-doped fiber laser with a BPP of 0.50 mm-mrad," in *Fiber Lasers XVII: Technology and Systems*, L. Dong, Ed., vol. 11260, International Society for Optics and Photonics. SPIE, 2020, p. 1126022. [Online]. Available: https://doi.org/10.1117/12.2545832

[36] B.-C. Hwang, S. Jiang, T. Luo, J. Watson, G. Sorbello, and N. Peyghambarian, "Cooperative upconversion and energy transfer of new high Er3+- and Yb3+–Er3+-doped phosphate glasses," *J. Opt. Soc. Am. B*, vol. 17, no. 5, pp. 833–839, May 2000. [Online]. Available: https://opg.optica.org/josab/abstract.cfm?URI=josab-17-5-833

[37] D. J. Richardson, J. Nilsson, and W. A. Clarkson, "High power fiber lasers: current status and future perspectives," *J. Opt. Soc. Am. B*, vol. 27, no. 11, pp. B63–B92, Nov 2010. [Online]. Available: https://opg.optica.org/josab/abstract.cfm?URI=josab-27-11-B63

[38] X. Zhao, Q. Han, D. Wang, H. Hu, K. Ren, J. Jiang, and T. Liu, "Optimal design of high-power cascade co-pumping Er/Yb-codoped fiber lasers,"

Opt. Lett., vol. 44, no. 5, pp. 1100–1103, Mar 2019. [Online]. Available: https://opg.optica.org/ol/abstract.cfm?URI=ol-44-5-1100

[39] H. Lin, Y. Feng, Y. Feng, P. Barua, J. K. Sahu, and J. Nilsson, “656W Er-doped, Yb-free large-core fiber laser,” *Opt. Lett.*, vol. 43, no. 13, pp. 3080–3083, Jul 2018. [Online]. Available: https://opg.optica.org/ol/abstract.cfm?URI=ol-43-13-3080

[40] T. Sakimura, K. Hirosawa, Y. Watanabe, T. Ando, S. Kameyama, K. Asaka, H. Tanaka, M. Furuta, M. Hagio, Y. Hirano, H. Inokuchi, and T. Yanagisawa, “1.55-µm high-peak, high-average-power laser amplifier using an Er,Yb:glass planar waveguide for wind sensing coherent Doppler lidar,” *Opt. Express*, vol. 27, no. 17, pp. 24 175–24 187, Aug 2019. [Online]. Available: https://opg.optica.org/oe/abstract.cfm?URI=oe-27-17-24175

[41] J. Nomura, K. Hirosawa, T. Yanagisawa, N. Ohata, S. Imamura, D. Sakaizawa, and N. Tomii, “Single-frequency 45-mj pulses from a MOPA system using an Er,Yb:glass planar waveguide amplifier and a large mode area Er-doped fiber amplifier,” *Opt. Lett.*, vol. 48, no. 7, pp. 1758–1761, Apr 2023. [Online]. Available: https://opg.optica.org/ol/abstract.cfm?URI=ol-48-7-1758

[42] F. F. Wu and J. W. Pierce, “An eye-safe optical parametric oscillator system with more than 5-megawatts peak power,” in *Laser Technology for Defense and Security VI*, M. Dubinskii and S. G. Post, Eds., vol. 7686, International Society for Optics and Photonics. SPIE, 2010, p. 768609. [Online]. Available: https://doi.org/10.1117/12.848611

[43] G. Roy and P. Mathieu, “Comparison of Raman and degenerated optical parametric oscillators for a high-energy and high-repetition-rate eye-safe laser,” *Optical Engineering*, vol. 35, no. 12, pp. 3579 – 3584, 1996. [Online]. Available: https://doi.org/10.1117/1.601112

[44] M. Kaskow, L. Gorajek, W. Zendzian, and J. Jabczynski, “MW peak power KTP-OPO-based “eye-safe” transmitter,” *Opto-Electronics Review*,

vol. vol. 26, no. No 2, pp. 188–193, 2018. [Online]. Available: http://czasopisma.pan.pl/Content/115313/PDF/main.pdf

[45] J. Guo, G. Y. He, Z. X. Jiao, and B. Wang, "Efficient high-peak-power and high-repetition-rate eye-safe laser using an intracavity KTP OPO," *Laser Physics*, vol. 25, no. 3, p. 035403, feb 2015. [Online]. Available: https://dx.doi.org/10.1088/1054-660X/25/3/035403

[46] H. Liu, Y. Yu, H. Liu, Y. Wang, H. Zheng, H. Liu, and G. Jin, "1.5 µm eye-safe self-optical parametric oscillator with composite resonator based on Nd3+-doped MgO:PPLN," *Infrared Physics & Technology*, vol. 118, p. 103870, 2021. [Online]. Available: https://www.sciencedirect.com/science/article/pii/S1350449521002425

[47] R. W. Boyd, *Nonlinear optics.* Academic press, 2019.

[48] C. V. Raman and K. S. Krishnan, "A new type of secondary radiation," *Nature*, vol. 121, no. 3048, pp. 501–502, 1928.

[49] L. Rayleigh, "XXXIV. On the transmission of light through an atmosphere containing small particles in suspension, and on the origin of the blue of the sky," *The London, Edinburgh, and Dublin Philosophical Magazine and Journal of Science*, vol. 47, no. 287, pp. 375–384, 1899.

[50] G. G. Stokes, *On the Change of Refrangibility of Light.* Royal Society, 1852, vol. 142, pp. 463–562. [Online]. Available: https://books.google.co.uk/books?id=CE9FAAAAcAAJ

[51] S. Antipov, A. Sabella, R. J. Williams, O. Kitzler, D. J. Spence, and R. P. Mildren, "1.2kW quasi-steady-state diamond Raman laser pumped by an M^2=15 beam," *Opt. Lett.*, vol. 44, no. 10, pp. 2506–2509, May 2019. [Online]. Available: https://opg.optica.org/ol/abstract.cfm?URI=ol-44-10-2506

[52] V. G. Savitski, I. Friel, J. E. Hastie, M. D. Dawson, D. Burns, and A. J. Kemp, "Characterization of single-crystal synthetic diamond for multi-watt continuous-

wave raman lasers," *IEEE Journal of Quantum Electronics*, vol. 48, no. 3, pp. 328–337, 2012.

[53] A. Penzkofer, A. Laubereau, and W. Kaiser, "High intensity Raman interactions," *Progress in Quantum Electronics*, vol. 6, no. 2, pp. 55–140, 1979.

[54] V. G. Savitski, S. Reilly, and A. J. Kemp, "Steady-state raman gain in diamond as a function of pump wavelength," *IEEE Journal of Quantum Electronics*, vol. 49, no. 2, pp. 218–223, 2013.

[55] C. Kranert, C. Sturm, R. Schmidt-Grund, and M. Grundmann, "Raman Tensor Formalism for Optically Anisotropic Crystals," *Phys. Rev. Lett.*, vol. 116, p. 127401, Mar 2016. [Online]. Available: https://link.aps.org/doi/10.1103/PhysRevLett.116.127401

[56] A. McKay, A. Sabella, and R. Mildren, "Polarization Conversion in Cubic Raman Crystals," *Scientific Reports*, vol. 7, p. 41702, 2017.

[57] A. Sabella, J. A. Piper, and R. P. Mildren, "1240 nm diamond Raman laser operating near the quantum limit," *Opt. Lett.*, vol. 35, no. 23, pp. 3874–3876, Dec 2010. [Online]. Available: https://opg.optica.org/ol/abstract.cfm?URI=ol-35-23-3874

[58] A. M. Zaitsev, *Optical Properties of Diamond: A Data Handbook*. Springer-Verlag Berlin Heidelberg, 2001. [Online]. Available: https://doi.org/10.1007/978-3-662-04548-0

[59] O. Kitzler, A. McKay, and R. P. Mildren, "Continuous-wave wavelength conversion for high-power applications using an external cavity diamond Raman laser," *Opt. Lett.*, vol. 37, no. 14, pp. 2790–2792, Jul 2012. [Online]. Available: https://opg.optica.org/ol/abstract.cfm?URI=ol-37-14-2790

[60] Q. Xiao, P. Yan, D. Li, J. Sun, X. Wang, Y. Huang, and M. Gong, "Bidirectional pumped high power Raman fiber laser," *Opt. Express*,

vol. 24, no. 6, pp. 6758–6768, Mar 2016. [Online]. Available: https://opg.optica.org/oe/abstract.cfm?URI=oe-24-6-6758

[61] T. Qi, D. Li, G. Fu, Y. Yang, G. Li, L. Wang, S. Du, P. Yan, M. Gong, and Q. Xiao, "Amplification of random lasing enables a 10-kW-level high-spectral-purity Yb-Raman fiber laser," *Opt. Lett.*, vol. 48, no. 7, pp. 1794–1797, Apr 2023. [Online]. Available: https://opg.optica.org/ol/abstract.cfm?URI=ol-48-7-1794

[62] M. Li, P. Li, X. Zhang, Y. Feng, J. Yao, S. Li, and W. Chen, "21.8 W CW second-stokes CVD-diamond raman laser at 1516 nm," *Applied Physics B*, vol. 124, p. 165, 2018. [Online]. Available: https://doi.org/10.1007/s00340-018-7031-9

[63] Y. T. Chang, K. W. Su, H. L. Chang, and Y. F. Chen, "Compact efficient Q-switched eye-safe laser at 1525 nm with a double-end diffusion-bonded Nd:YVO4 crystal as a self-Raman medium," *Opt. Express*, vol. 17, no. 6, pp. 4330–4335, Mar 2009. [Online]. Available: https://opg.optica.org/oe/abstract.cfm?URI=oe-17-6-4330

[64] H. Jianhong, L. Jipeng, S. Rongbing, L. Jinghui, Z. Hui, X. Canhua, S. Fei, L. Zongzhi, Z. Jian, Z. Wenrong, and L. Wenxiong, "Short pulse eye-safe laser with a stimulated Raman scattering self-conversion based on a Nd:KGW crystal," *Opt. Lett.*, vol. 32, no. 9, pp. 1096–1098, May 2007. [Online]. Available: https://opg.optica.org/ol/abstract.cfm?URI=ol-32-9-1096

[65] L. Dziechciarczyk, "Novel use of diamond in eye-safe lasers," Ph.D. dissertation, University of Strathclyde, 2020.

[66] Y.-F. Chen, Y.-H. Hsu, S.-Q. Lin, D.-J. Liu, and H.-C. Liang, "Compact actively Q-switched Nd:YVO4/YVO4 Raman laser at 1525nm with frequency up to 150 kHz," *Opt. Express*, vol. 32, no. 14, pp. 25 498–25 507, Jul 2024. [Online]. Available: https://opg.optica.org/oe/abstract.cfm?URI=oe-32-14-25498

[67] M. Rini, I. Cristiani, and V. Degiorgio, "Numerical modeling and optimization of cascaded CW Raman fiber lasers," *IEEE Journal of Quantum Electronics*, vol. 36, no. 10, pp. 1117–1122, 2000.

[68] S. Ding, X. Zhang, Q. Wang, F. Su, S. Li, S. Fan, S. Zhang, J. Chang, S. Wang, and Y. Liu, “Theoretical models for the extracavity Raman laser with crystalline Raman medium,” *Applied Physics B: Lasers and Optics*, vol. 85, no. 1, pp. 89–95, oct 2006.

[69] Y. Tsutsumi and M. Ohashi, “Simple technique for measuring Raman gain efficiency spectrum distribution in a single-mode fiber,” in *Passive Components and Fiber-based Devices VI*, P. P. Shum, Ed., vol. 7630, International Society for Optics and Photonics. SPIE, 2009, p. 763005. [Online]. Available: https://doi.org/10.1117/12.853074

[70] A. Sabella, J. A. Piper, and R. P. Mildren, “Efficient conversion of a 1.064 μm Nd:YAG laser to the eye-safe region using a diamond Raman laser,” *Opt. Express*, vol. 19, no. 23, pp. 23 554–23 560, Nov 2011. [Online]. Available: https://opg.optica.org/oe/abstract.cfm?URI=oe-19-23-23554

[71] J. Sulc, H. Jelinkova, J. K. Jabczynski, W. Zendzian, J. Kwiatkowski, K. Nejezchleb, and V. Skoda, “Comparison of diode-side-pumped triangular Nd:YAG and Nd:YAP laser,” in *Solid State Lasers XIV: Technology and Devices*, H. J. Hoffman and R. K. Shori, Eds., vol. 5707, International Society for Optics and Photonics. SPIE, 2005, pp. 325 – 334. [Online]. Available: https://doi.org/10.1117/12.588233

[72] M. Boucher, O. Musset, J. Boquillon, and E. Georgiou, “CW and Q-switched diode end-pumped Nd:YAP laser at 1.34 µm. Influence of Nd doping level,” in *Advanced Solid-State Lasers*. Optica Publishing Group, 2001, p. WB11. [Online]. Available: https://opg.optica.org/abstract.cfm?URI=ASSL-2001-WB11

[73] A. McKay, O. Kitzler, and R. P. Mildren, “Simultaneous Brightness Enhancement and Wavelength Conversion to the Eye-Safe Region in a High-Power Diamond Raman Laser,” *Laser & Photonics Reviews*, vol. 8, no. 3, pp. L37–L41, 2014.

[74] R. J. Williams, J. Nold, M. Strecker, O. Kitzler, A. Mckay, T. Schreiber, and

R. P. Mildren, “Efficient Raman frequency conversion of high-power fiber lasers in diamond,” *Laser and Photonics Reviews*, vol. 9, no. 4, pp. 405–411, jul 2015.

[75] O. Kitzler, A. M. McKay, D. J. Spence, and R. P. Mildren, “Modelling and Optimization of Continuous-Wave External Cavity Raman Lasers,” *Optics Express*, vol. 23, no. 7, pp. 8590–8602, 2015.

[76] O. Svelto, *Principles of Lasers*, 5th ed. Springer Science+Business Media, 2010. [Online]. Available: https://doi.org/10.1007/978-1-4419-1302-9

[77] Element Six Technologies, *CVD Diamond Handbook*, Element Six, 2024, technical handbook, available online. [Online]. Available: https://e6cvd.com/media/wysiwyg/pdf/Diamond_Handbook_2024.pdf

[78] Y.-S. Tzeng, Y.-J. Huang, C.-Y. Tang, K.-W. Su, W.-D. Chen, G. Zhang, and Y.-F. Chen, “High-Power Tunable Single- and Multi-Wavelength Diode-Pumped Nd:YAP Laser in the $^4\mathrm{F}_{3/2} \rightarrow {}^4\mathrm{I}_{11/2}$ Transition,” *Optics Express*, vol. 21, no. 22, pp. 26 261–26 268, 2013.

[79] L. Schearer and P. Tin, “Laser performance and tuning characteristics of a diode pumped Nd:YAlO3 laser at 1083 nm,” *Optics Communications*, vol. 71, no. 3, pp. 170–174, 1989. [Online]. Available: https://www.sciencedirect.com/science/article/pii/0030401889904215

[80] F. Hanson and P. Poirier, “Multiple-wavelength operation of a diode-pumped Nd:YAlO3 laser,” *J. Opt. Soc. Am. B*, vol. 12, no. 7, pp. 1311–1315, Jul 1995. [Online]. Available: https://opg.optica.org/josab/abstract.cfm?URI=josab-12-7-1311

[81] A. A. Kaminskii, S. E. Sarkisov, I. V. Mochalov, L. K. Aminov, and A. O. Ivanov, “Anisotropy of spectroscopic characteristics in the biaxial YAlO3-Nd3+ laser crystals,” *physica status solidi (a)*, vol. 51, no. 2, pp. 509–520, 1979. [Online]. Available: https://onlinelibrary.wiley.com/doi/abs/10.1002/pssa.2210510224

[82] T. Waritanant and A. Major, "Diode-pumped Nd:YVO4 laser with discrete multi-wavelength tunability and high efficiency," *Opt. Lett.*, vol. 42, no. 6, pp. 1149–1152, Mar 2017. [Online]. Available: https://opg.optica.org/ol/abstract.cfm?URI=ol-42-6-1149

[83] R. Paschotta, "Birefringent Tuners," *RP Photonics Encyclopedia*, 2007. [Online]. Available: https://www.rp-photonics.com/birefringent_tuners.html

[84] K. Naganuma, G. Lenz, E. P. Ippen *et al.*, "Variable Bandwidth Birefringent Filter for Tunable Femtosecond Lasers," *IEEE Journal of Quantum Electronics*, vol. 28, no. 10, pp. 2142–2150, 1992.

[85] S. Zhu, "Birefringent filter with tilted optic axis for tuning dye lasers: theory and design," *Appl. Opt.*, vol. 29, no. 3, pp. 410–415, Jan 1990. [Online]. Available: https://opg.optica.org/ao/abstract.cfm?URI=ao-29-3-410

[86] T. Waritanant and A. Major, "Dual-wavelength Operation of a Diode-pumped Nd:YVO$_4$ Laser at the 1064.1 & 1073.1 nm and 1064.1 & 1085.3 nm Wavelength Pairs," *Applied Physics B*, vol. 124, no. 5, p. 87, 2018. [Online]. Available: https://doi.org/10.1007/s00340-018-6960-7

[87] Crytur s.r.o., "Nd:yap laser crystals," 2025, accessed: 2025-07-27. [Online]. Available: https://www.crytur.com/materials/nd-yap/

[88] D. Findlay and R. Clay, "The measurement of internal losses in 4-level lasers," *Physics Letters*, vol. 20, no. 3, pp. 277–278, 1966. [Online]. Available: https://www.sciencedirect.com/science/article/pii/0031916366903635

[89] R. Paschotta, "Electro-optic Modulators," RP Photonics Encyclopedia, 2006. [Online]. Available: https://www.rp-photonics.com/electro_optic_modulators.html

[90] A. J. Glass and A. H. Guenther, "Laser Induced Damage of Optical Elements–a Status Report," *Appl. Opt.*, vol. 12, no. 4, pp. 637–649, Apr 1973. [Online]. Available: https://opg.optica.org/ao/abstract.cfm?URI=ao-12-4-637

[91] X. Pan, B. Zhou, S. Yu, D. Piliptsou, H. Sun, and Z. Liu, "Preparation and properties of anti-reflective and anti-thermal shock of Y2O3/AlN composite films on CVD diamond," *Ceramics International*, vol. 50, no. 13, Part B, pp. 23 999–24 007, 2024. [Online]. Available: https://www.sciencedirect.com/science/article/pii/S0272884224015098

[92] X. Chang, W. Gao, J. An, H. Chen, Z. Liu, Z. Qi, C. Li, J. Ding, W. Li, K. Wang, Y. Wang, Z. Lu, and Z. Bai, "Optical-grade diamond: characteristics, synthesis, and recent research progress," *Functional Diamond*, vol. 5, no. 1, p. 2476690, 2025. [Online]. Available: https://doi.org/10.1080/26941112.2025.2476690

[93] T. Zhu, C. Liu, W. Zhang, Y. Wang, S. Li, Y. Zhu, W. Lian, G. Zhang, Y. Zhang, P. Sun, X. Hu, K. Nishimura, and N. Jiang, "Design, preparation and optical properties of novel Y2O3/Si/diamond/Y2O3 composite materials for IR windows," *Diamond and Related Materials*, vol. 153, p. 112028, 2025. [Online]. Available: https://www.sciencedirect.com/science/article/pii/S0925963525000858

[94] D. Ristau, M. Jupé, and K. Starke, "Laser damage thresholds of optical coatings," *Thin Solid Films*, vol. 518, no. 5, pp. 1607–1613, 2009, proceedings of the 36th International Conference on Metallurgical Coatings and Thin Films. [Online]. Available: https://www.sciencedirect.com/science/article/pii/S0040609009012851

[95] T. K. Yeung, D. L. Sage, L. M. Pham, P. L. Stanwix, and R. L. Walsworth, "Anti-reflection coating for nitrogen-vacancy optical measurements in diamond," *Applied Physics Letters*, vol. 100, no. 20, p. 201111, 2012.

[96] T. P. Mollart and K. L. Lewis, "Transition metal oxide anti-reflection coatings for airborne diamond optics," *Diamond and Related Materials*, vol. 10, pp. 536–540, 2001.

[97] D. Reinhard, D. Tran, T. Schuelke, M. Becker, T. Grotjohn, and J. Asmussen, "SiO2 antireflection layers for single-crystal diamond," *Diamond*

and Related Materials, vol. 25, pp. 84–86, 2012. [Online]. Available: https://www.sciencedirect.com/science/article/pii/S0925963512000660

[98] Z. Song, H. Yuan, P. Fan, M. Li, J. Shen, S. Wang, and G. Bian, "Enhancing fluorescence of diamond NV- centers for quantum sensing: A multi-layer optical antireflection coating," *Diamond and Related Materials*, vol. 141, p. 110584, 2024. [Online]. Available: https://www.sciencedirect.com/science/article/pii/S0925963523009093

[99] S. D. Childs, G. W. Smith, T. P. Mollart, W. Allen, R. H. Bennett, C. F. Kennedy, and J. E. Field, "Anti-reflection coating of diamond, for use at elevated temperatures," in *Optical Interference Coatings.* Optica Publishing Group, 2007, p. ThD8. [Online]. Available: https://opg.optica.org/abstract.cfm?URI=OIC-2007-ThD8

[100] H. Jiao, X. Cheng, J. Lu, G. Bao, J. Zhang, B. Ma, H. Liu, and Z. Wang, "Study for Improvement of Laser Induced Damage of 1064 nm AR Coatings in NanosecondPulse," *J. Opt. Soc. Korea*, vol. 17, no. 1, pp. 1–4, Feb 2013. [Online]. Available: https://opg.optica.org/josk/abstract.cfm?URI=josk-17-1-1

[101] Z. Song, X. Cheng, H. Ma, J. Zhang, B. Ma, H. Jiao, and Z. Wang, "Influence of coating thickness on laser-induced damage characteristics of anti-reflection coatings irradiated by 1064 nm nanosecond laser pulses," *Appl. Opt.*, vol. 56, no. 4, pp. C188–C192, Feb 2017. [Online]. Available: https://opg.optica.org/ao/abstract.cfm?URI=ao-56-4-C188

[102] International Organization for Standardization, "ISO 11254: Optics and optical instruments. Lasers and laser related equipment. Test methods for laser induced damage threshold of optical surfaces," Parts 1–3, Geneva, Switzerland, 2000–2006.